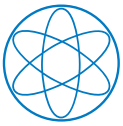

Technische Universität München

Max-Planck-Institut für Plasmaphysik

Université de Lorraine

Experimental study of turbulence at the plasma edge of ASDEX Upgrade tokamak with an ultra-fast swept reflectometer

Anna Medvedeva

Vollständiger Abdruck der von der Fakultät für Physik der Technischen Universität München zur Erlangung der akademischen Grades eines

Doktors der Naturwissenschaften

genehmigten Dissertation.

Vorsitzender: Prof. Dr. Martin Beneke

Prüfer der Dissertation:

Prof. Dr. Ulrich Stroth
Prof. Dr. Stéphane Heuraux
Prof. Dr. Laura Fabbietti
Prof. Dr. Michel Vergnat
Dr. Clarisse Bourdelle
Prof. Evgeniy Z. Gusakov

Die Dissertation wurde am 04.09.2017 bei der Technischen Universität München eingereicht und durch die Fakultät für Physik am 30.10.2017 angenommen.

DEPARTMENT OF PHYSICS

TECHNISCHE UNIVERSITÄT MÜNCHEN

Experimental study of turbulence at the plasma edge of ASDEX Upgrade tokamak with an ultra-fast swept reflectometer

Anna Medvedeva

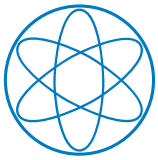

DEPARTMENT OF PHYSICS

TECHNISCHE UNIVERSITÄT MÜNCHEN

Max-Planck-Institut für Plasmaphysik

Experimental study of turbulence at the plasma edge of ASDEX Upgrade tokamak with an ultra-fast swept reflectometer

Author:	Anna Medvedeva
Supervisor:	Prof. Ulrich Stroth, Prof. Stéphane Heuraux
Advisor:	Dr. Frédéric Clairet, Dr. Garrard D. Conway
Submission Date:	04.09.2017

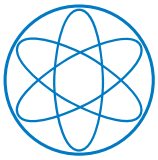

I confirm that this is my own work and I have documented all sources and material used.

Munich, 04.09.2017 Anna Medvedeva

Abstract

Plasma confinement is limited by energy and particle transport, in which turbulence plays an important role. In this work the measurements of the turbulence characteristics carried out on the ASDEX Upgrade tokamak are presented during the transition from the Low (L) to the High (H) confinement mode which goes through an Intermediate (I) phase where turbulence and shear flows strongly interact. One of the most widely accepted theories concerning the L-H transition describes how the turbulence in the plasma edge is stabilized by radial electric field gradients: the $\mathbf{E} \times \mathbf{B}$ flow shear stabilizes turbulence and decreases the radial size of turbulent structures. As a consequence, a transport barrier forms in the edge where the plasma density, the temperature, and their gradients increase. The detailed physical mechanism of the formation of the transport barrier as well as the reason for the residual transport across this barrier are not yet well understood.

The density dynamics is measured by an ultra-fast swept reflectometer (UFSR) with a time resolution as high as 1 μs. The methods used for the evaluation of density and density fluctuations and for the spectra reconstruction from this diagnostic are discussed. First, studies of the electron density profile dynamics, the density turbulence level, radial wavenumber and frequency spectra during L-H transitions in ASDEX Upgrade have been performed. The reflectometer measurements show that the density large scale fluctuations decrease after an L-H transition, which confirms the theoretical predictions of the turbulence reduction by sheared flows and supports previous experimental evidences.

I-phases for various plasma conditions are documented and the density gradient evolution is compared with the turbulence level. This investigation is carried out to discriminate between turbulence-driven zonal flows and neoclassically driven shear flows. In the I-phases in medium and high density discharges oscillations of the fluctuation amplitude and the background flow are observed. An important contribution of the density gradient to the neoclassical radial electric field has been confirmed. The I-phase

bursts might be explained by growing pressure driven edge instabilities which cause a pressure crash consistent with previous studies on AUG. Therefore the bursts in the established I-phase present more features of edge localised modes (ELM). However, the comparison between the neoclassical electric field estimate and the Doppler reflectometer measurement of the poloidal flow velocity gives indications that the first few periods of the I-phase can have a different behaviour compared to the established I-phase.

Moreover the results on high frequency coherent modes appearing at the plasma edge are presented. The edge coherent modes (ECMs) observed in the I-phase or during ELM-free and ELMy H-mode phases have common characteristics, such as their frequency of about 100 kHz, radial position and scaling of the frequency with the pressure gradient. The absence of the ballooning character, the propagation in the electron diamagnetic direction and the localisation at the pedestal top indicate that the ECMs are related to microtearing modes. The impact of ECMs on plasma confinement and transport is still an issue that needs to be investigated in the future.

Zusammenfassung

Der Plasmaeinschluss ist durch Energie- und Teilchentransport begrenzt, die zum großen Teil durch Turbulenzen verursacht werden. In dieser Arbeit stellen wir Messungen der Turbulenzcharakteristiken am Übergang vom niedrigen Einschluss-(L-mode) zum hohen Einschlussregime (H-mode) vor. Dabei geht das Plasma durch ein Zwischenregime (I-phase), in dem Turbulenz und Scherströmung stark wechselwirken. Die Messungen wurden am ASDEX-Upgrade-Tokamak durchgeführt. Eine der anerkanntesten Theorien bezüglich des L-H-Übergangs behauptet, dass die Turbulenz am Plasmarand durch den erhöhten Gradienten des radialen elektrischen Feldes stabilisiert wird: die $\mathbf{E} \times \mathbf{B}$-Scherungströmung stabilisiert die Turbulenz und verringert die radiale Größe der turbulenten Strukturen. Als Konsequenz bildet sich eine sogenannte Transportbarriere am Plasmarand, wo die Dichte, die Temperatur und deren Gradienten zunehmen. Der detaillierte physikalische Mechanismus der Bildung der Transportbarriere sowie der Grund für den Resttransport über diese Barriere sind noch nicht gut verstanden.

Die Dynamik in der Dichte wird hier mit einem ultra-schnellen gesweepten Reflektometer (UFSR) mit einer Zeitauflösung von 1 μs gemessen. Die Methoden der Dichte- und Dichtefluktuationsauswertung und die Spektrenrekonstruktion werden diskutiert. Untersuchungen der Dynamik des Elektronendichteprofils, des Turbulenzniveaus, der radialen Wellenzahlspektren und der Frequenzspektren während der L-H-Übergänge in ASDEX Upgrade wurden durchgeführt. Die Reflektometer-Messungen zeigen, dass die großskaligen Dichtefluktuationen nach einem L-H-Übergang abnehmen, was die theoretischen Vorhersagen der Turbulenzreduktion durch verscherte Strömungen bestätigt und vorherige experimentelle Ergebnisse stützt.

I-Phasen bei verschiedene Plasmabedingungen werden dokumentiert und die Dichtegradientenentwicklung wird mit dem Turbulenzniveau verglichen. Diese Untersuchung wird durchgeführt, um zwischen turbulenzgetriebenen Zonalströmungen und neoklassisch getriebenen Scherströmungen zu unterscheiden. In den beobachteten I-Phasen in Entladungen mittlerer und hoher Dichte werden Schwankungen der Fluktuationsamplitude

und der Hintergrundströmung beobachtet. Ein wichtiger Beitrag des Dichtegradienten zum neoklassischen radialen elektrischen Feld wurde bestätigt. Der sprunghafte Ausstieg im Turbulenzniveau der I-Phase könnten durch wachsende druckgetriebene Randinstabilitäten erklärt werden, die einen Druckeinbruch im Einklang mit früheren Studien am AUG verursachen. Daher präsentiert die etablierte I-Phase mehr Merkmale des Verhaltens der sogenannten "Edge-localised modes" (ELM). Der Vergleich des aus der neoklassischen Theorie abgeschätzten elektrischen Feldes mit der Messung des Doppler-Reflektometers zeigt jedoch, dass die ersten Perioden der I-Phase ein unterschiedliches Verhalten im Vergleich zur etablierte I-Phase haben.

Darüber hinaus werden Ergebnisse zu hochfrequenten kohärenten Moden präsentiert, die am Plasmarand auftreten. Die in der I-Phase, ELM-freien oder ELM-igen H-Moden beobachteten kohärenten Randmoden (ECMs) haben gemeinsame Eigenschaften, wie etwa ihre Frequenz von 100 kHz, die radiale Position und die Skalierung der Frequenz mit dem Druckgradienten. Das Fehlen der poloidalen Abhängigkeit der Amplitude, die Ausbreitung in der elektronendiamagnetischen Richtung und die Lokalisierung am Übergang vom Rand- zum Innenbereich des Plasmas könnten auf Mikrotearing-Moden hinweisen. Die Auswirkungen der ECM auf den Plasma-Einschluss und auf den Transport sind Themen, das in Zukunft untersucht werden sollten.

Résumé

La turbulence au sein d'un plasma contribue de manière significative à l'augmentation du transport de l'énergie et des particules. Ce transport diminue la qualité de confinement du plasma réduisant par là même la possibilité d'atteindre le seuil de fusion. Notre travail a consisté à étudier et à mesurer l'évolution des caractéristiques de cette turbulence ainsi que son rôle durant la transition d'un mode à faible confinement (L-mode) à un mode de confinement amélioré (H-mode) des plasmas du tokamak ASDEX Upgrade (AUG). Nous avons, en particulier, étudié la phase de transition intermédiaire (I-phase) où la turbulence et le cisaillement des structures turbulentes par les flux interagissent. L'une des théories les plus largement acceptées concernant la transition L-H prévoit que la turbulence au bord du plasma est stabilisée par des gradients de champs électriques radiaux: le cisaillement de flux $\mathbf{E} \times \mathbf{B}$ stabilise la turbulence et diminue la taille radiale des structures. En conséquence, une barrière de transport se forme dans le bord où la densité plasma, la température et leurs gradients augmentent. Le mécanisme physique détaillé de la formation de la barrière de transport ainsi que la raison du transport résiduel à travers cette barrière ne sont pas encore bien compris.

Afin d'étudier la dynamique radiale et temporelle de cette transition avec la meilleur résolution possible, nous nous sommes servis d'un réflectomètre à balayage en fréquence ultra-rapide développé par l'IRFM du CEA Cadarache et installé sur AUG. Durant nos campagnes expérimentales nous sommes parvenus à réduire ce temps de balayage à 1 μs, temps jamais atteint jusqu'à présent. Les méthodes utilisées pour l'évaluation des fluctuations de densité et de densité ainsi que pour la reconstruction des spectres à partir des données de ce diagnostic sont discutées. La dynamique du profil de densité électronique, du niveau de turbulence, des spectres en nombre d'onde et des spectres en fréquence lors des transitions L-H dans ASDEX Upgrade ont été réalisées. Les mesures montrent que le niveau des fluctuations de grande échelle diminue après une transition L-H, ce qui confirme les prédictions théoriques de la réduction de la turbulence par le cisaillement.

La I-phase a été documentée pour diverses conditions du plasma et l'évolution du gradient de densité comparée à celle du niveau de turbulence. Cette étude a permis de distinguer les flux zonaux créés par la turbulence des flux cisaillés néoclassiques. Dans les I-phases, pour les décharges à moyenne et haute densité, les oscillations de l'amplitude de fluctuation et le flux néoclassique ont été observées. Une contribution importante du gradient de densité au champ électrique radial néoclassique a été confirmée. Ces oscillations ou "bursts" pourraient s'expliquer par des instabilités qui, au bord du plasma, sont générées par la pression, et provoquent une modulation du gradient de pression, conformément aux études précédentes sur AUG. Par conséquent, la I-phase présente les caractéristiques des modes localisés au bord (ELM) et qui apparaissent durant la phase mode-H. Cependant, la comparaison entre l'estimation du champ électrique néoclassique et la mesure du réflectomètre Doppler de la vitesse du flux poloidale donne des indications que les premières périodes de la I-phase peuvent avoir un comportement différent par rapport à la I-phase établie.

Enfin, ces réflectomètres ont aussi permis l'observation de modes cohérents à haute fréquence apparaissant au bord du plasma. Ces modes cohérents (ECM), clairement localisés au bord du plasma, qui ont été observés à la fois durant la I-phase et la phase mode H, avec ou sans ELMs, ont des caractéristiques communes, telles que leur fréquence d'environ 100 kHz, leur position radiale et la dépendance de la fréquence avec le gradient de pression. L'absence du caractère ballooning, la propagation dans le sens de la vitesse diamagnétique des électrons et la localisation en haut du piédestal de pression indiquent que les ECMs sont liés aux modes microtearing. L'impact des ECMs sur le confinement et le transport du plasma est encore un problème qui doit être étudié dans le futur.

Contents

to Alexey A. Meshcheriakov and Huguette Destais

1 Introduction

I cannot explain how desperately I was longing to that
radiant little room as I stood there knocking at the door.
If only I could reach it, I thought, everything would be all right.
– Yukio Mishima, The Temple of the Golden Pavilion

In the field of energy production on Earth, fusion can potentially provide an almost unlimited source of sustainable and clean energy. The fusion of two light nuclei, like deuterium and tritium, occurs only in plasmas at very high temperatures where the particles have sufficient kinetic energy to tunnel through the Coulomb barrier. Reactor materials cannot withstand these high temperatures, thus systems with magnetic plasma confinement are used. The plasma confinement is limited by several factors, one of them being the turbulent fluctuations causing enhanced particle and energy transport to the reactor wall. Therefore the turbulence in magnetised plasma should be characterized at time and space resolution required to reveal the physical mechanisms associated to it. The dynamics of the turbulent events is also a key issue for a possible control of the plasma behaviour and to maintain a steady state during a discharge.

1.1 Fusion

A fusion reaction, for example between deuterium and tritium, can be written as:

$$ {}^{2}_{1}\mathrm{D} + {}^{3}_{1}\mathrm{T} \longrightarrow {}^{4}_{2}\mathrm{He} + \mathrm{n} + E \tag{1.1} $$

where both initial compounds have comparable masses. The reaction leads to the production of a heavier compound (He, also called α-particle) accompanied by the production of a neutron. To determine which reaction ingredients will produce an exothermic reaction ($E > 0$), it is necessary to analyse the nucleons' binding energy as a function of the number of nucleons in a nucleus A. As the nucleons' binding energy

increases with the mass in the region $A < 56$, the fusion reaction releases a positive amount of energy.

Comparing the cross sections for different light nuclei reactions [1], the most efficient controlled fusion reactions should use the isotopes of hydrogen, deuterium and tritium. The preferred fusion reaction producing 17.6 MeV is that of a D-T mixture at the optimum temperature of the order of 20 keV. Therefore every reactor should have a powerful heating source to reach this high temperature. At high temperatures atoms and molecules are partially or fully ionised, creating a plasma state. To achieve fusion, the plasma should be confined without direct contact with the reactor constructing materials. The two leading confinement approaches are magnetic fusion, where the plasma is confined by magnetic field [2], and inertial confinement, where the plasma, ignited by laser beams, is implanted inside a reactor [3].

In the ignited state the energy released in the α-particles of the fusion reactions should maintain the temperature of the plasma. The parameter Q is defined by the ratio of the fusion power P_{fusion} to the externally applied and deposited in plasma power P_{ext}:

$$Q = \frac{P_{\text{fusion}}}{P_{\text{ext}}}. \tag{1.2}$$

When Q tends to infinity, the external source can be switched off and the plasma becomes self-sustaining. The limit $Q = 1$ is called break-even, the plasma produces as much energy as it is needed to maintain it under the required conditions for the temperature defined by the Lawson criterion. The Lawson criterion for the fusion plasma density n and temperature T can be deduced from a power balance consideration:

$$n\,T\,\tau_E > 3 \times 10^{21} \ \text{keV}\,\text{s}/\text{m}^3, \tag{1.3}$$

where τ_E is the energy confinement time [4] determined by the conduction loss and the radiation loss which strongly increase with the temperature. The range of appropriate temperatures is defined by the temperature dependence of the reaction cross-section, while the product of n and τ_E is provided by a semi-empirical expression deduced from a large set of experiments [5].

1.2 The tokamak concept

At the moment the tokamak is the most advanced magnetic confinement fusion concept where the magnetic field lines are closed in a toroidal shape. The concept was invented

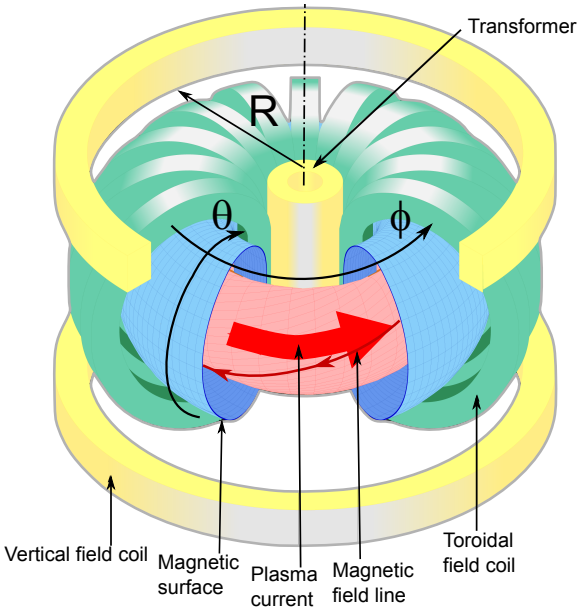

Figure 1.1: Scheme of a tokamak: the toroidal field coils produce the toroidal field B_ϕ, the poloidal field $B_\theta$is produced by the plasma current I_p (adapted from www.ipp.mpg.de)

by I. E. Tamm and the first realisation was built in the 50s in the USSR [6]. The toroidal magnetic field is created by poloidal coils (called toroidal field coils in Fig. 1.1) and is therefore inhomogeneous and decreases in strength with the distance R from the axis. The charged particles in this case not only rotate around and follow the magnetic field lines, but also execute a drift motion perpendicular to the field lines. The negative effect of the drift can be eliminated through a twist of the field lines, induced by a toroidal current inside the plasma, I_p. In addition a vertical magnetic field is required to prevent the radial expansion of the plasma and to companse part of the Grad-Shafranov shift. However the tokamak can present disruptions, which is a major problem for a fusion reactor due to the large induced forces.

The equilibrium of the plasma can be expressed through the force balance

$$\mathbf{j} \times \mathbf{B} = \nabla p, \tag{1.4}$$

where p is the plasma pressure, j is the current in the plasma and B is the magnetic field. This equality expresses the principle of magnetic confinement. The ratio between the kinetic pressure p and the magnetic pressure is characterized by the parameter:

$$\beta = \frac{2\mu_0 p}{B^2} \tag{1.5}$$

The major radius R is defined as the distance from the tokamak toroidal axis of symmetry. The cross-section of a tokamak is presented on the example of ASDEX Upgrade in Fig. 1.2. The separatrix or the last closed flux surface (LCFS) is shown in red. The set of the vertical magnetic field coils which controls the plasma shape is shown with yellow boxes. A toroidal field coil is illustrated as green shell. ASDEX Upgrade is one of the first tokamaks to use a divertor configuration: a configuration of the magnetic field lines with an X-point for the LCFS (Fig. 1.2) allowing to remove power and particles from the tokamak plasma and shield it from impurities originating from the walls. The field lines contact the vessel wall on specially equipped inner and outer divertor plates.

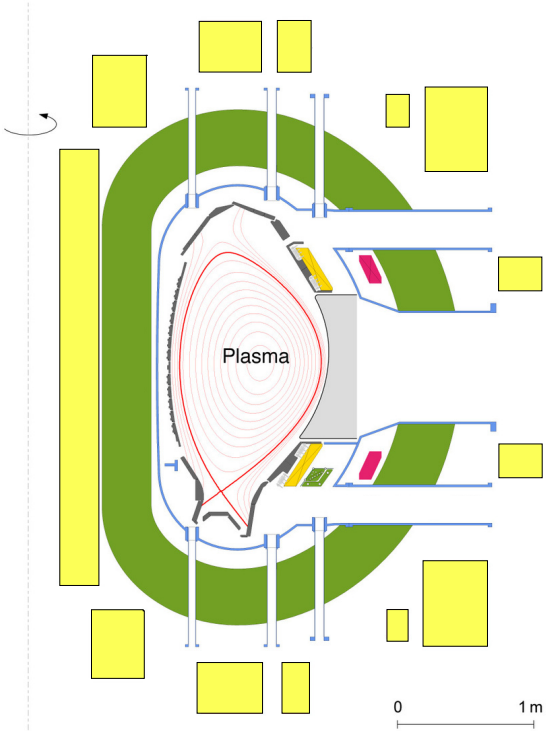

Figure 1.2: Scheme of the tokamak ASDEX Upgrade: poloidal cross-section (adapted from www.ipp.mpg.de)

The energy confinement time τ_E is limited by the transport of energy and particles across the magnetic field. As an example, the particle transport equation can be written in general form for the particle flux Γ_j for the particle species j (electrons or ions) [7]:

$$\Gamma_j = -D_n \frac{\partial n_j}{\partial r} - D_T \frac{\partial T_j}{\partial r} + V n_j + \Gamma_j^{\delta}. \tag{1.6}$$

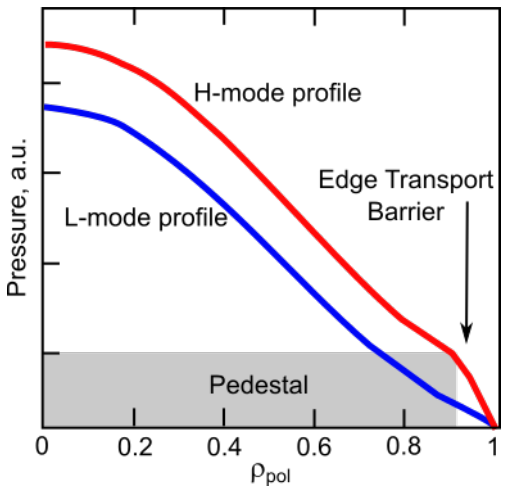

Figure 1.3: Scheme of the pedestal formation in H-mode: the profiles of the pressure in L-mode (blue) and in the H-mode (in red) against the normalised radius ρ_{pol}

The losses consist of a sum of terms arising from Coulomb collisions (classical and neoclassical transport) and from the turbulent fluctuations. The coefficients D in this equation are the particle diffusion coefficients, V is a convection velocity. Γ_j^{δ} is a particle flux due to the electrostatic and magnetic fluctuations. The energy transport equation has a similar form. The experiments revealed that the confinement is significantly lower than that predicted by only neoclassical transport, therefore the turbulent processes are dominant for the energy transport in tokamaks.

1.3 H-mode

In 1982 a regime of improved confinement, the H-mode, was discovered on the ASDEX tokamak [8]. The importance of the H-mode comes from the fact that the energy confinement time is about a factor of two higher compared to the low-confinement mode (L-mode). The nature of the transition to the H-mode is still unclear. The improved confinement is reached above a certain power threshold increasing with plasma density and magnetic field [9]. The timescale of the L-H transition is about 100 µs [10]. After the transition significant changes in the plasma edge parameters lead to reduced transport and the suppression of turbulent fluctuations. As consequence, an edge transport barrier (ETB) develops. The plasma pressure forms a pedestal, as it is shown in Fig. 1.3, and both the temperature and the density develop steep gradients in the edge. Time

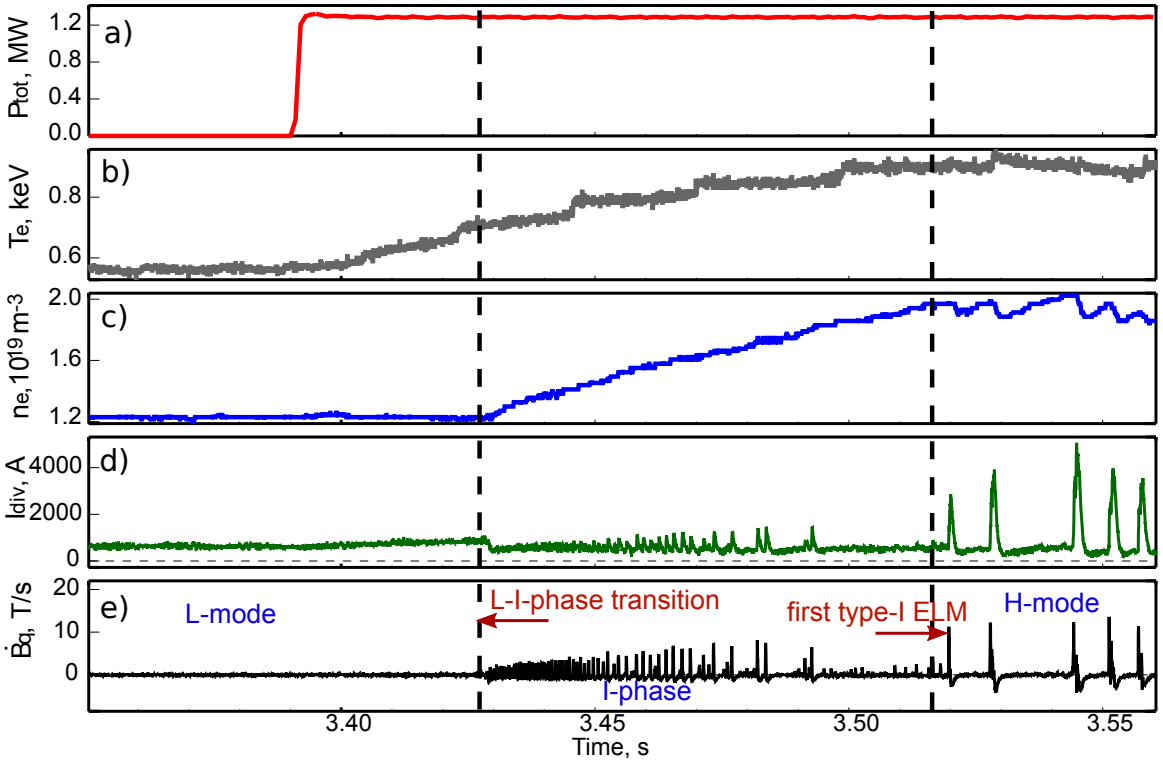

Figure 1.4: Typical L-H transition in AUG: (a) a power step of the auxiliary heating P_{tot} is followed by the edge temperature rise (b), the increase of the line averaged density (c) starts with a delay of about 50 ms and coincides with a drop in the divertor shunt current (d) and the I-phase oscillations, visible on the Mirnov coil (e)

traces of a typical L-H transition are shown in Fig. 1.4. The edge electron temperature (Fig. 1.4b) increases after switching on 1.4 MW of auxiliary heating (Fig. 1.4a) at 3.39 s. However, the edge density (Fig. 1.4c) starts to rise with a delay of about 50 ms after a drop in the inner divertor shunt current I_{div} (Fig. 1.4d), which is an indication of the reduced particle transport. The H-mode (at t >3.52 s) is characterised by the edge localised modes (ELM) causing enhanced transport and therefore appearing as spikes in the divertor current. In between the L-mode and the H-mode an intermediate phase (I-phase) occurs [11]. During this phase oscillations of various plasma parameters, such as density, temperature, edge flow velocity, turbulence level, are observed. These oscillations are accompanied by the bursts in the magnetic signal $\partial B_\theta / \partial t$ measured with Mirnov coils (Fig. 1.4e). The I-phase in this discharge is followed by a short quiescent H-mode which is an H-mode without ELM activity by definition [12].

Several theories have been developed to explain the L-H transition mechanism, the most accepted and experimentally observed one being the reduction of the edge turbulence due to sheared plasma flows driven by a radial electric field [13]. Two alternative models for the generation of the sheared flow exist. The first one suppose that the local edge pressure gradient steepening with the input power contributes to the total electric field through the diamagnetic velocity and hence increases the shearing rate [14]. The associated background $\mathbf{E} \times \mathbf{B}$ flow plays a fundamental role in the established H-mode by preventing the turbulence to develop, in spite of the strong gradients in the pedestal region which can drive turbulence [15]. However this model does not explain the L-H transition. The other model is based on the interaction of the turbulence with the poloidal flows which can be triggered by several mechanisms. One of them is a predator-prey relation between the turbulence and the turbulence induced flows, including so called zonal flows [16]. Zonal flows (ZFs) are toroidally and poloidally symmetric radial perturbations in tokamaks. The predator-prey model might explain the I-phase oscillations observed experimentally in many machines ([11, 17–20]). The comparison with the experimental observations stays contradictory. In order to distinguish between the models a progress in the measurements techniques is needed, which could allow both high temporal (order of microseconds) and spatial (order of millimeter) resolution in the plasma edge. The quantities of interest are the edge gradients of temperature and density, the turbulence and the electric field. This thesis contributes to these measurements.

1.4 Thesis goals and outline

The description of the relationship between plasma turbulence and confinement is one of the milestones in the global understanding of fusion plasma physics. The high diversity and controversy of experimental data are due to the complexity of the turbulent phenomena and to the diagnostics limitations. The ultra-fast swept reflectometer (UFSR), a new diagnostic of electron density and density turbulent fluctuations, has been finished to be developed and installed at the ASDEX Upgrade tokamak at the beginning of this PhD work for extended turbulence investigations with a time resolution of 1 μs during L and H-mode. The scope of this work is to exploit the specific strengths of the UFSR to study the fluctuation spectra, the radial propagation of turbulence and the fast density profile dynamics due to confinement transitions. This work examines the L-H transition from the beginning of the I-phase to the established H-mode and attempts to shed light on the fast edge phenomena with the microsecond time resolution.

The aim of this investigation is to provide a better understanding of the turbulence and flow velocity shear behaviour during the L-H transition. The relative temporal evolution of the background electric field, the turbulence driven flows and the density fluctuation level is addressed using the UFSR and fixed frequency Doppler reflectometers. The cause-consequence relation of the turbulence and the electric field is studied in order to discriminate between the different models of the L-H transition.

The properties of turbulence frequency spectra should be investigated to reveal the driving forces of edge instabilities and the underlying physics. The radial localisation and temporal evolution of edge modes will be analysed from the UFSR data combined with the other edge diagnostics at AUG. The possible role of the edge coherent modes in the L-H transition and ELM triggering has to be studied.

In Chapter 2 some basics of plasma physics are introduced. Chapter 3 illustrates the role of turbulence in plasma confinement. Chapter 4 gives a short description of the ASDEX Upgrade tokamak and the plasma diagnostics used in this work. In Chapter 5 a detailed history of UFSR and its characteristics are presented. The turbulence dynamics during the L-H transition is investigated experimentally in Chapter 6. Chapter 7 is dedicated to the experimental results on the edge coherent modes observed after the transition from the L-mode to the I-phase and the H-mode. Finally, the results of this work are summarised and discussed in Chapter 8.

2 Basics of plasma physics

Plasma is partially or totally ionized gas composed of neutral atoms or molecules and charged particles, ions and electrons. In tokamaks except close to the vacuum vessel the plasma can be considered as fully ionised. Its most important property is the quasi-neutrality, i.e. the bulk densities of positive and negative charged particles are almost equal. Plasma in many ways can be described like a fluid. However, the behavior of plasma in some cases, especially when it is exposed to electric and magnetic fields is a complicated and intrinsically tangled process which is determined by the motion of charged particles in the electromagnetic field, by the propagation of the electromagnetic waves in the plasma and by the particle-wave interaction. This chapter introduces the principles of the particle motion (Section 2.1) needed to understand the different mechanisms involved in the turbulence and the associated terminology. The drift motion is discussed as a key mechanism for the drift wave turbulence. The electromagnetic wave propagation inside a magnetised plasma is described in the Section 2.2 and is related to the use of microwave probing in this work. This section also includes the discussion of the microwave reflectometer spacial resolution resulting from the wave propagation.

2.1 Charged particle dynamics in a tokamak

2.1.1 Drifts in a tokamak plasma

If the effects of the micro turbulence are neglected, the theoretical description of plasma evolves in two directions. In the case of a slow plasma motion, the solution of the kinetic equation leads to the so-called two-fluid hydrodynamics, which in many cases reduces to one-fluid magnetohydrodynamics (MHD). In another extreme case, when the characteristic time is much smaller than the collisional time, the plasma is described by the Vlasov equation [21].

In the case of a strong magnetic field, the decomposition with a small parameter, the ratio of the Larmor radius to the characteristic scale, is used. This approach is simple and efficient for a tokamak plasma, where the magnetic and electric forces are dominant compared to the gravitational one. The equation of motion for a single particle can be written as:

$$m_\alpha \frac{d\mathbf{v}}{dt} = q_\alpha(\mathbf{E} + \mathbf{v} \times \mathbf{B}), \tag{2.1}$$

where m_α and q_α are the mass and the charge of a particle α (electron or ion). Supposing the magnetic field to be uniform and time independent $\mathbf{B} = B\mathbf{e_z}$, where $B = \text{const}$, and the absence of an electric field, the motion of the particle can be easily described. The resulting particle orbit is a helical trajectory following the magnetic field lines. The rotation frequency, called also gyro or cyclotron frequency, is:

$$\Omega_{c,\alpha} = \frac{|q_\alpha|B}{m_\alpha} \tag{2.2}$$

and the radius of the orbit (gyro- or Larmor radius) is:

$$r_{L,\alpha} = \frac{v_{\perp,\alpha}}{\Omega_{c,\alpha}} = \frac{m_\alpha v_{\perp,\alpha}}{|q_\alpha|B}, \tag{2.3}$$

where $v_{\perp,\alpha}$ is the velocity component perpendicular to the magnetic field. It is convenient to analyse the movement of the gyro-center called the guiding centre.

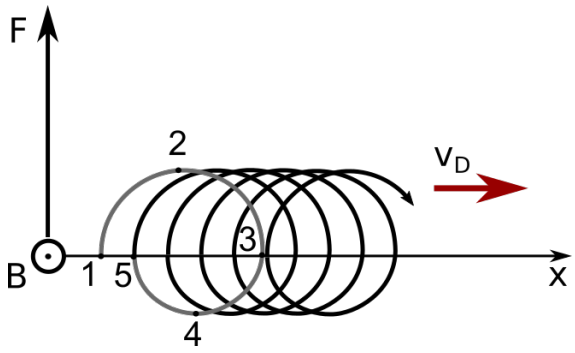

Figure 2.1: The result of a force $\mathbf{F}$ perpendicular to $\mathbf{B}$ on the particle motion: as r_L, is larger in the upper part of the orbit than in the lower part, the guiding centre drifts.

The presence of an external force in equation (2.1), for the simplicity with a constant acceleration $\mathbf{F}/m$ perpendicular to the magnetic field, produces a guiding centre drift [21]. The nature of this drift can be explained with Fig. 2.1. When a particle moves

from point 1 to point 2, the force **F** increases its perpendicular speed and its gyro-radius. On the contrary while the particle passes from point 2 to point 3 it decelerates. The average velocity $v_\perp$ is smaller on the path 3-4-5 than on 1-2-3. Therefore the difference in the averaged r_L leads to a drift perpendicular to both the magnetic field and the force **F**. The velocity of the drift is equal to:

$$\mathbf{v}_D = \frac{\mathbf{F} \times \mathbf{B}}{q_\alpha B^2}. \tag{2.4}$$

The forces present in a tokamak create various drifts: the **E**×**B** drift, the ∇B-drift and the curvature drift. For a constant electric field **E** the drift velocity, or **E**×**B** velocity has no dependence on the particle charge, i.e. the ions and the electrons drift in the same direction:

$$\mathbf{v}_{\mathrm{E}\times\mathrm{B}} = \frac{\mathbf{E} \times \mathbf{B}}{B^2}. \tag{2.5}$$

In curved magnetic fields, the centrifugal force on the plasma due to particle motion along the curved field lines with parallel velocity $v_\parallel$ acts like a gravitational force in (2.4) and produces the curvature drift:

$$\mathbf{v}_{\kappa,\alpha} = -\frac{m_\alpha v_{\parallel,\alpha}^2}{2q_\alpha B^3} \nabla B \times \mathbf{B}. \tag{2.6}$$

The gradient of the magnetic field modifies the gyro-motion as in Fig. 2.1 leading to the ∇B drift:

$$\mathbf{v}_{\nabla B} = -\frac{m_\alpha v_{\perp,\alpha}^2}{q_\alpha B^3} \nabla B \times \mathbf{B}. \tag{2.7}$$

The equation for the plasma fluid in equilibrium can be deduced from the equation of motion for electrons and ions [22]:

$$0 = \nabla p_\alpha - q_\alpha n_\alpha (\mathbf{E} + \mathbf{u}_\alpha \times \mathbf{B}) \tag{2.8}$$

By taking the cross-product with the magnetic field the following equation is obtained:

$$\mathbf{u}_{\perp,\alpha} = -\frac{\nabla p_\alpha \times \mathbf{B}}{n_\alpha q_\alpha B^2} + \frac{\mathbf{E} \times \mathbf{B}}{B^2} c = \mathbf{u}_{dia,\alpha} + \mathbf{u}_{\mathrm{E}\times\mathrm{B}} \tag{2.9}$$

The dominant plasma flow velocities are the **E**×**B** drift and diamagnetic drift velocities.

The diamagnetic drift replaces the curvature and ∇B drifts in the fluid description of the plasma if there is the density gradient ∇n_α or the temperature gradient ∇T_α. Figure 2.2 shows the generation of the magnetisation current $\mathbf{J_m}$ with a density gradient:

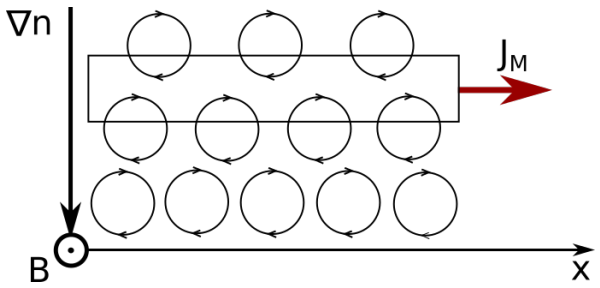

Figure 2.2: The result of a density gradient: in a volume unit the difference in the number of particles, that rotate in the direction of Ox and in the opposite direction, creates a magnetisation current $\mathbf{J_m}$

in a chosen volume there are more particles rotating in the direction of the x axes and less in the oposite direction leading to a net particle flow. The same effect can be produced by the temperature gradient that creates a higher velocity for each following layer of particles and also a current in x direction. Thus a perturbation of the plasma density or temperature as well as a local electric field leads to a particle motion which might enhance the instability as it will be described in the Chapter 3. Therefore the drifts in plasma are one of the fundamental mechanisms affecting the plasma confinement and the transport of particles and energy.

Equation (2.8) can be written for the tokamak geometry as [23]:

$$E_r = \frac{1}{n_\alpha q_\alpha}\frac{\partial p_\alpha}{\partial r} + u_{\perp,\alpha}B = \frac{1}{eZ_\alpha n_\alpha}\frac{\partial p_\alpha}{\partial r} - u_{\theta,\alpha}B_\phi + u_{\phi,\alpha}B_\theta, \tag{2.10}$$

because the pressure is assumed constant on flux surfaces. $u_{\theta,\alpha}$ and $u_{\phi,\alpha}$ are the poloidal and toroidal velocity components, respectively. This formula is often used in spectroscopy [24] for radial electric field measurements, but should be applied cautiously for the fast dynamics and turbulent plasmas as it uses the assumption of plasma equilibrium.

2.1.2 Collisional transport

The term transport in the plasma means the combination of the transport processes of particles, energy, momentum and electrical charge, which can be described by corresponding transport equations where the transport coefficients such as the diffusion coefficient D indicate the ratio of the transported quantity to the driving force. The

transport coefficients are determined microscopically by the mean free path lengths of the plasma particles. In contrast to neutral gases, Coulomb collisions are important for plasma transport. In a tokamak parallel (to magnetic field) and perpendicular (or radial) transports are distinguished. Coulomb collisions affect the gyro-radius of the particle creating so-called classical transport. Modeling the collisions as a random-walk process, the classical diffusion coefficient can be expressed as:

$$D_{\text{clas}} = \frac{r_L^2}{2\tau} = \frac{r_L^2 \nu}{2}, \tag{2.11}$$

where τ is the time between the collisions and ν is the collisionality [25]. The classical transport dominates at high collisionality.

The tokamak configuration introduces a population of particles trapped in a magnetic mirror created by the magnetic field gradient along the field lines. The orbit of a trapped particle has a banana shape on the projection to the tokamak poloidal cross-section [26]. Therefore with low collisionality the transport is enhanced by the trapped particles and the corresponding regime is called neoclassical transport. Between low-collisionality (banana regime) and high-collisionality (Pfirsch-Schlüter regime) regimes, the plateau regime is introduced.

However the experiments observe a radial transport which is larger than the neoclassical or classical predictions [27]. The difference in the transport coefficients is attributed to the turbulent transport which will be introduced in Chapter 3 after the discussion of the turbulence properties.

2.2 Wave propagation in a magnetised plasma

The propagation of an electromagnetic wave in plasma presents a special interest in the frame of tokamak plasma diagnostics with microwaves, particularly for the reflectometry application. This section summarises the basics of the microwave propagation in a magnetised plasma which will be used in the next chapters. The wave propagation equation is derived from the Maxwell's equations and the electron equation of motion. As the results on the refractive index appear in many papers and books, only a quick overview will be made in this section. The assumptions used to obtain the refractive index will be discussed and the difference between O and X mode will be explained. We will consider phenomena which are faster than the typical time of collisional relaxation.

2.2.1 Dielectric permittivity tensor

The wave creates a small perturbation with wave vector $\mathbf{k}_\perp || \mathbf{e_x}$ of the homogenous equilibrium perpendicular to a constant magnetic field $\mathbf{B} = B_0\mathbf{e_z}$. The background electric field is $E_0 = 0$. One can find the dielectric permittivity as it is shown in [28] by calculating the current density response j_i to the wave field $\tilde{E}$ from Ohm's law:

$$j_i = \sigma_{ik}\tilde{E}_k, \tag{2.12}$$

where σ is the conductivity tensor, the index k appearing twice implies summation over all components x, y, z. Then the dielectric permittivity tensor has a simple form:

$$\epsilon_{ik} = \left(1 - \sum_\alpha \frac{\omega_{p\alpha}^2}{\omega^2 - \Omega_{c\alpha}^2}\right)(\delta_{ik} - b_i b_k) + \left(1 - \sum_\alpha \frac{\omega_{p\alpha}^2}{\omega^2}\right) b_i b_k + i \sum_\alpha \frac{\omega_{p\alpha}^2 \Omega_{c\alpha}}{\omega(\omega^2 - \Omega_{c\alpha}^2)} e_{ikj} b_j, \tag{2.13}$$

where

$$\omega_{p\alpha} = \sqrt{\frac{Z_\alpha n_\alpha e^2}{\epsilon_0 m_\alpha}} \tag{2.14}$$

is the plasma frequency, $\Omega_{c\alpha}$ is the cyclotron frequency, $\mathbf{b} = \mathbf{B}/B$, α indicates electrons or ions. This expression can be obtained from the MHD approach too, and stays correct in the approximation of a cold plasma or long wave-length perturbations ($\mathbf{kv} \to 0$) without spatial dispersion.
The dispersion equation for the electric field $\tilde{\mathbf{E}}$ of the wave is:

$$L_{ij}E_\beta = (k_i k_j - k^2\delta_{ij} + \frac{\omega^2}{c^2}\epsilon_{ij})\tilde{E}_j = 0 \tag{2.15}$$

We have chosen coordinates in a way that $\mathbf{k} = (k_\perp, 0, k_\parallel)$, so from (2.13) $\epsilon_{xz} = \epsilon_{yz} = 0$, $\epsilon_{xy} = i\sum_\alpha \frac{\omega_{p\alpha}^2 \Omega_{c\alpha}}{\omega(\omega^2 - \Omega_{c\alpha}^2)} e_{xyz} b_z \neq 0$, and (2.15) transforms into:

$$\frac{\omega^2}{c^2}\begin{pmatrix} -k_\parallel^2\frac{c^2}{\omega^2} + \epsilon_{xx} & \epsilon_{xy} & k_\perp k_\parallel \frac{c^2}{\omega^2} \\ \epsilon_{yx} & -\frac{k^2c^2}{\omega^2} + \epsilon_{yy} & 0 \\ k_\perp k_\parallel \frac{c^2}{\omega^2} & 0 & (k_\parallel^2 - k^2)\frac{c^2}{\omega^2} + \epsilon_{zz} \end{pmatrix}\begin{pmatrix} E_x \\ E_y \\ E_z \end{pmatrix} = 0. \tag{2.16}$$

The ion can be considered at rest for the frequencies of the wave higher than the ion cyclotron frequency, which is the case for reflectometry. Therefore only the electrons will contribute to the dielectric permittivity ϵ.

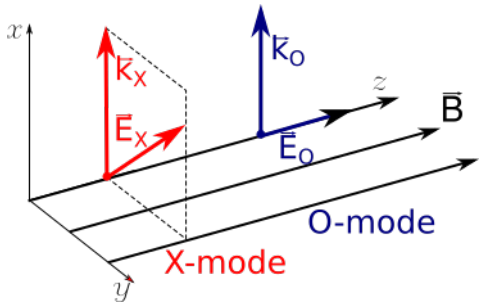

Figure 2.3: Electric field and wave vector for O- and X-mode polarised waves

2.2.2 O- and X-mode polarisation

In order to fullfill the conditions of free wave propagation $\det L_{ij}$ should be 0. The case of the propagation perpendicular to the magnetic field, $k_{\|} = 0$, represents an interest for reflectometry. The matrix L_{ij} then has two blocks:

$$L_{ij} = \frac{\omega^2}{c^2}\begin{pmatrix} \epsilon_{xx} & \epsilon_{xy} & 0 \\ \epsilon_{yx} & -\frac{k^2c^2}{\omega^2} + \epsilon_{yy} & 0 \\ 0 & 0 & -k^2\frac{c^2}{\omega^2} + \epsilon_{zz} \end{pmatrix}. \tag{2.17}$$

This leads to the separation of so called O- (Ordinary) and X-mode (eXtra-ordinary) polarisations (Fig. 2.3). The dispersion relation for O-mode ($\mathbf{k}\perp\mathbf{B}, \mathbf{E}\|\mathbf{B}$) polarisation in general form is:

$$N_O^2 = \frac{k^2c^2}{\omega^2} = 1 - \frac{\omega_{pe}^2}{\omega^2}. \tag{2.18}$$

The cutoff is reached when $N = 0$, i.e. the electromagnetic wave is reflected if its frequency $\omega = \omega_p$. The extra-ordinary wave ($\mathbf{k}\perp\mathbf{B}, \mathbf{E}\perp\mathbf{B}$) has eliptical polarisation in the plane perpendicular to the plasma magnetic field (Fig. 2.3). The refractive index far from the resonances is equal to:

$$N_X^2 = \frac{k^2c^2}{\omega^2} = 1 - \frac{\omega_{pe}^2}{\omega^2}\frac{\omega^2 - \omega_{pe}^2}{\omega^2 - \Omega_{ce}^2 - \omega_{pe}^2}. \tag{2.19}$$

For the electron cyclotron and plasma frequencies the cutoff frequency has two branches, the lower and upper one:

$$\omega_{\pm} = \frac{\Omega_{ce}}{2}\left(1 \pm \sqrt{1 + \frac{4\omega_{pe}^2}{\Omega_{ce}^2}}\right) \tag{2.20}$$

In contrast to the O-mode, the X-mode refractive index depends not only on the electron density but also on the magnetic field.

At high electron temperatures ($T_e > 2$ keV) relativistic effects will change the reflectometry cutoff location and modify the wave propagation [29]. This means that the reflectometry measurements become dependent on the knowledge of the local electron temperature. The cutoff frequencies can still be obtained from the cold plasma approximation by replacing the rest electron mass m_e with the mass m_e^* given by

$$m_e^* = m_e\sqrt{1 + 5T_e/m_e c^2}. \tag{2.21}$$

2.2.3 Radial resolution of reflectometry

Without going into the details of the reflectometry technique which will be described in the Chapter 5, the radial resolution of this method can be discussed based on the wave propagation principles. For a continuous medium it is impossible to talk about one point of reflection, however, in a tokamak plasma one still defines the cutoff layer as the positions where the refractive index for a given probing wave frequency goes to zero, because after this point the wave electrical field decreases exponentially. The cutoff layers are represented schematically for a tokamak cross-section in Fig. 2.4 for O-mode (Fig. 2.4a) and X-mode (Fig. 2.4b) waves. The surfaces of the constant poloidal flux are shown with dashed lines and labeled with the value of ρ_{pol}, while the cutoff surfaces are colour-coded for frequencies 40–110 GHz. The density profile is shown in Fig. 2.4c.

Generally speaking there are also back-scattered reflections before the cutoff layer (Fig. 2.5), which are neglected if the plasma density doesn't have strong gradients [28] and should be taken into account in the turbulent tokamak plasma. We should distinguish therefore the main reflection from the cutoff layer that serves for density profile measurements and the reflections from the density fluctuations which follow the Bragg rule:

$$\mathbf{k}_f - \mathbf{k}_{\text{wave}} = \mathbf{k}_{\text{wave}}, \tag{2.22}$$

where $\mathbf{k}_{\text{wave}}$ is the wave vector of the wave and $\mathbf{k_f}$ is the wave vector of the fluctuation. For reflectometry the question of the localisation of the signal's reflection becomes primordial.

For the direct reflection usually the width of the cutoff layer is defined as the width of the first maximum of the wave electrical field near the cutoff and can be described by

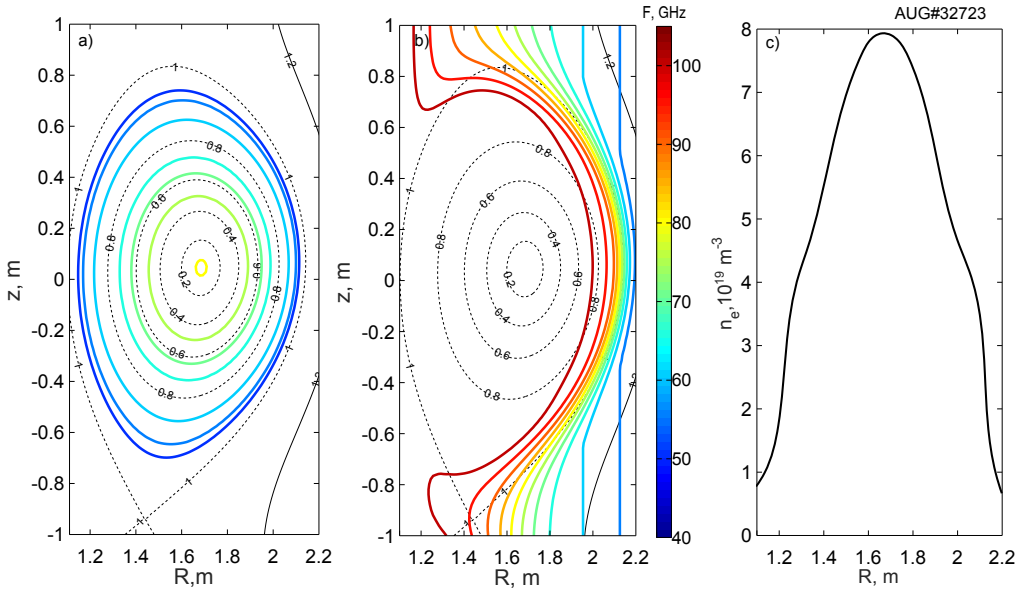

Figure 2.4: Cutoff layers for (a) O-mode and (b) X-mode polarisation in the ASDEX Upgrade geometry, poloidal cross-section and (c) the electron density profile ($t = 3$ s, #32723). The surfaces of poloidal flux are marked with dashed lines, magnetic field $B = 2.49$ T

an Airy function. In the assumption of a linear unperturbed density profile it is possible to express the electric field of the reflected wave using the first Born approximation and find the produced phase shift [30, 31].

The density fluctuation effects on the wave propagation were studied in various works [32] and are due to back-scattering processes. The localisation of the probing wave phase response was found in the cutoff vicinity [33, 34], while the theory predicts the Bragg condition is satisfied for different wavenumbers continuously on the way to the cutoff. This led to the explanation considering 2D effects, but the disagreement between the code results and the experiments stayed. So in [32] it has been shown that for a density perturbation with the wavenumber k_f smaller than the double of Airy wavenumber

$$k_A = 0.63 k^{2/3} L^{-1/3}, \tag{2.23}$$

where L is the density gradient length, the Bragg condition is not satisfied, therefore the phase response is sensitive only to the cutoff layer oscillation and is higly spatially resolved. If $k_f > 2k_A$, the resonant Bragg scattering is dominant, which means that the response is not localised and occurs far from the cutoff. Nevertheless, in

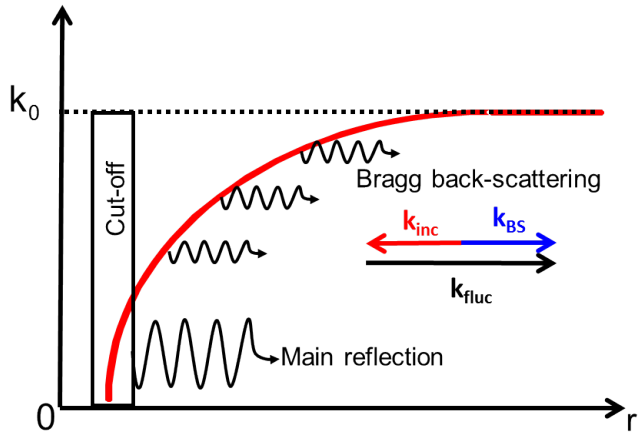

Figure 2.5: The wavenumber decreases from the vacuum value at the antenna to zero at the cutoff

tokamak plasmas the fluctuation spectra generally decrease with a power law for large wavenumbers.

In ASDEX Upgrade typical Airy wavenumber in the plasma edge is 2–5 cm^{-1} for waves of 50–100 GHz and 1–2 cm^{-1} in the core. If the corresponding characteristic width of the k_f-spectrum is smaller than k_A, the phase will contain information about the density fluctuations localised close to the cutoff layer.

3 Instabilities and turbulence in fusion plasmas

The main objective of the magnetic confinement is to isolate the plasma from the surrounding materials to maintain the fusion reactions. However, the tokamak confinement has different limits which trigger plasma macroscopic and microscopic instabilities leading to the energy and particle loss. In order to interpret experimental observations of the plasma edge dynamics during confinement transitions the impact of the macroscopic MHD phenomena and of the micro turbulence should be analysed. Therefore first a short description of macroscopic MHD instabilities and ELMs underlying their effect on the edge pressure and confinement will be given in section 3.1. Turbulence is a mixture of non-linearly interacting microscopic modes and it is introduced in this chapter as second actor on the plasma transport properties in section 3.2. The drift wave is discussed as a key ingredient of the turbulence. Then, the suppression of turbulence by sheared flows is described. Thereby a short overview of the turbulent zonal flows, their generation during limit-cycle oscillations and their impact on the plasma properties is presented. At the end of the chapter the link between turbulence suppression and plasma confinement is discussed.

3.1 MHD instabilities and ELMs

In the MHD model the plasma is considered as a quasineutral fluid of charged particles. Therefore magnetic fields induce currents, which in their turn locally polarize the plasma and modify the magnetic field itself. The equations that describe MHD are a combination of the Navier-Stokes and Maxwell's equations. The MHD instabilities, associated to growing MHD modes, arise due to the current and/or pressure gradients.

The magnetic structure of a tokamak consists of the nested tori of the magnetic surfaces. The safety factor along a field line is defined by the ratio between the number

of turns in the toroidal and in the poloidal directions before the field line closes in itself. The radial profile of the safety factor depends mainly on the current profile (the stronger is the current, the higher is q). From the Ampere's law $q(r)$ can be expressed as a function of the plasma current $I_p(r)$ inside the flux surface:

$$q(r) = \frac{2\pi r^2 B_\phi(r=0)}{\mu_0 R I_p(r)}, \tag{3.1}$$

where r is the minor radius of the magnetic surface and $B_\phi(r=0)$ is the toroidal magnetic field on the magnetic axis. The twisting of the field lines is different for each magnetic surface, this causes the magnetic shear:

$$s(r) = \frac{r}{q}\frac{\mathrm{d}q}{\mathrm{d}r}. \tag{3.2}$$

When $q(r)$ is a rational number $q(r) = m/n$, the magnetic field lines close after m poloidal and n toroidal turns and this case fcilitates the instability development.

MHD modes can be divided into two types: ideal and resistive modes [35]. In ideal MHD the plasma is considered to be perfectly conductive. In this case, the magnetic flux is conserved within each magnetic surface. This approach is only applicable when the plasma collisionallity is low and the resistivity is small. The resistivity of a tokamak plasma can become important in the vicinity of the rational surfaces. Then the ideal MHD approximation is not valid and the resistive MHD is introduced. The enhanced resistivity can result in the formation of magnetic islands or magnetic turbulence. Thus the magnetic structure can be broken by magnetic reconnection, releasing the stored magnetic energy as waves, in particle acceleration or heat.

Similar to $q(r)$ of the magnetic filed lines, an MHD mode can be characterized by its poloidal number m and its toroidal number n. A resonance is possible on the rational surfaces with the safety factor $q = m/n$. Some of the MHD modes are:

- Ideal kink modes $m = 1$, driven by the current density gradient;
- Ballooning mode (ideal or resistive), driven by the pressure gradient;
- Peeling mode, a sub-case of the kink mode with low toroidal mode numbers satisfying the condition $m - nq(a) = 0, m > 1$;
- Tearing mode (resistive), driven by the current density gradient.

The stability of the kink modes is defined by the Kruskal-Shafranov criterion [36] according to which $q(r)$ at the minor plasma radius a should satisfy

$$q(a) > 1. \tag{3.3}$$

In reality an external kink mode is destabilised already at $q = 2$, in addition there is a tendency for disruptions to occur more often for $q < 3$ [37]. These stability limits typically lead to the safety factor profile in the order of 1 at $\rho_{pol} = 0$ and higher than 3 at the separatrix. For the ballooning modes the stability is given by the Troyon's limit with respect to the normalised β [38]:

$$\beta_{N\mathrm{lim}} = \beta \frac{aB}{I_p} = 3. \tag{3.4}$$

Ballooning modes as pressure-driven instabilities impose the most strict upper limit on the plasma pressure for a given value of the magnetic field amplitude [39]. They tend to be localized on the low field side, in the region with unfavourable magnetic field line curvature.

During a tokamak discharge if enough energy is put into the plasma, the plasma reaches a state with a better confinement. This regime is called H-mode. Although the H-mode is the most favourable regime for a potential fusion reactor, it is associated with a confinement destructive phenomenon called edge localized modes or ELMs. ELMs lead to a periodic relaxation of the edge pressure profile [37]. Experimentally ELMs produce repetitive bursts in the D_α emission that indicates enhanced particle transport from the main plasma to the divertor. During an ELM the density and temperature gradients decrease abruptly (< ms) in the edge pointing out a confinement deterioration. After an ELM the plasma pressure recovers until the next ELM.

The first classification of ELMs observed at the DIII-D tokamak consists of three types [40]:

- Type I ELM is characterised by a strong burst in the D_α signal. The level of magnetic and density fluctuations increases before the ELM crash. The ELM repetition frequency in the range of 10 to 200 Hz increases with heating power. The plasma β_N is close to the ideal ballooning stability limit. The collapse of the edge pressure is about 50%.

- Type II ELMs are more frequent and the amplitude of the D_α-burst is smaller than in the type I ELMs. They appear in highly shaped plasmas. There is no information on the frequency dependence on power.

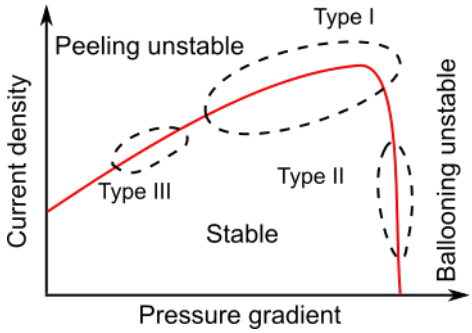

Figure 3.1: Qualitative peeling-ballooning stability diagram on the pedestal pressure-current density plane: the region under the red curve is stable, different ELM types are qualitatively marked with dashed areas

- Type III ELMs have a repetition frequency in the range of 0.5 to 20 kHz decreasing with heating power. The plasma β_N is significantly below than the ideal ballooning limit. A coherent magnetic precursor oscillation is observed on magnetic pick-up coils. The precursor frequency is about 50–70 kHz, the toroidal mode number n =5–10. The collapse of the edge pressure is about 10 %.

Over the years the precursors have been observed for Type II ELMs, too [41]. Other types of ELMs have been introduced, broadening their variety up to six types: type I–V and grassy ELMs [42].

The fast time scale and the presence of the radial magnetic field component B_r oscillations had led to the idea that ELMs can be described as a surface kink mode driven by the increased (compared to the L-mode) edge temperature and current density [37]. This theory has been extended in different ways in order to make robust quantitative predictions. Now it is generally agreed that ELMs can be described with the coupled peeling-ballooning model [43]. Within this model the ELM cycle can be qualitatively understood as shown in Fig. 3.1. The stability region is under the red curve, to the right, with a high pressure gradient, the ballooning part is unstable, above the curve the peeling instability is driven by the current. After a type I ELM crash the pressure gradient increases quickly, but the edge current density builds up slower, so first the ballooning limit boundary is reached first. Then the edge current density increases, leading to an instability with strong peeling mode character and radially broad eigenmodes. This produces the ELM crash with magnetic turbulent fluctuations and enhanced particle and energy transport. During the crash the stability boundary is

crossed again. The ELMs of type II are observed at the ballooning stability boundary, while type III ELMs occur at the peeling stability limit [44].

However the data on the pedestal evolution from many tokamaks cannot be explained purely by ideal MHD theory and a kinetic approach should be used. Analysis of data from many tokamaks lead to the hypothesis that kinetic ballooning modes (KBMs) limit the pressure gradient in the pedestal. The most prominent model widely used for the pedestal evolution predictions is called EPED and includes three main players: KBMs, the peeling-ballooning mode and the drift wave turbulence [45]. The model assumes that drift wave turbulence gets suppressed in the edge by sheared flow, then KBMs limit the pedestal pressure while the edge current density rises and triggers an ideal MHD peeling-ballooning mode resulting in an ELM crash [46]. The drift wave turbulence is introduced in the next section.

3.2 Turbulence

3.2.1 Drift waves

The plasma ions and electrons experience the drifts discussed in Chapter 2.1.1. In curved magnetic fields, by analogy with a fluid Rayleigh-Taylor instability, an instability arises when ∇B is directed away from the region of maximum pressure. In Fig. 3.2 ∇B causes, like in Chapter 2.1.1, the drift with the velocity $\mathbf{v}_D = \mathbf{v}_{\kappa,\alpha} + \mathbf{v}_{\nabla B}$ in the negative x direction for the ions. Taking a simple case of plasma with density n in the upper part of the plot and vacuum in the lower part, let us introduce a small wave-like perturbation on the plasma-vacuum boundary. The drift of ions causes a positive charge on one slope of the perturbation and the departure of ions creates a negative charge on the other. This separation of charges develops an electric field $\mathbf{E}'$ as it is shown in Fig. 3.2. The resulting $\mathbf{E}' \times \mathbf{B}$ drift is upward in the regions where the boundary had already moved upward and downward where the boundary had been deformed downward. Therefore the $\mathbf{E} \times \mathbf{B}$ drift enhances the instability, which is called a flute or **interchange** instability.

We have now considered different types of MHD instabilities that can be driven by the pressure gradient or the current density. There is another important type of instability in the fluid model, the so-called drift wave instability, that grows in a plasma with pressure gradient in a strong magnetic field. The curvature driven modes are two

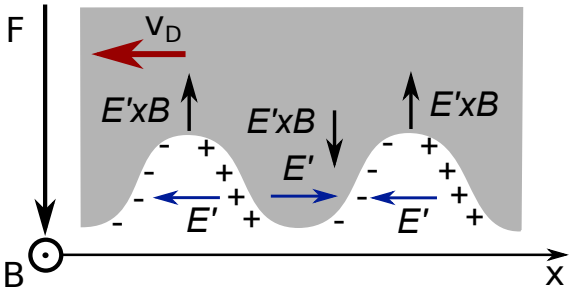

Figure 3.2: Mechanism of the flute instability

dimensional, while the drift waves are intrinsically three-dimensional. The drift waves require a finite plasma resistivity or other dissipation mechanism to be unstable [47].

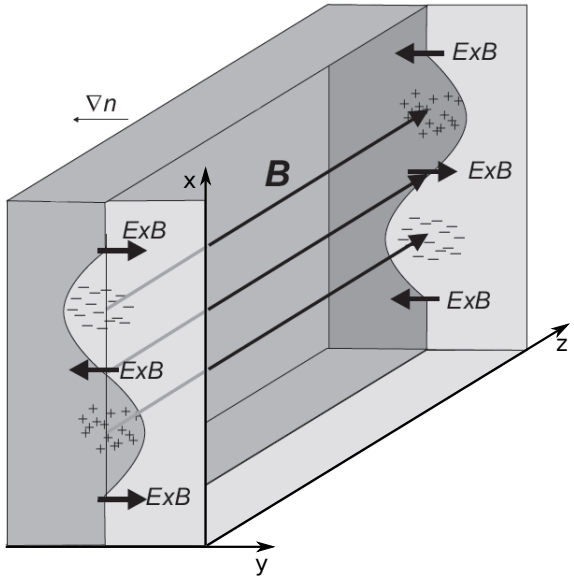

Figure 3.3: Mechanism of the drift wave instability (adapted from [48])

The mechanism of the **drift wave instability** is addressed in Fig. 3.3. Considering the density perturbation in the plane perpendicular to the magnetic field for the boundary between high density (darker part) and low density (lighter part), we assume that that the perturbation is periodic along the magnetic field lines, i.e. has a finite k_z. The displacement can be written then as: $\psi(x,t) = \psi_0(x)\exp(-i\omega t + ik_x x + ik_z z)$. Note that it is supposed that $k_z \ll k_x$. The electron dynamics parallel to B is assumed to be adiabatic [49], which means that a plasma pressure perturbation directly connects to a plasma potential perturbation. Therefore the electrons leave the high pressure

region and create a positive charge, on the contrary in the low pressure region the additional negative charge is stored. This leads to the periodic electric field E in the plane perpendicular to the magnetic field. In turn the electric field creates an $\mathbf{E} \times \mathbf{B}$ drift in the xy plane as it is shown in Fig. 3.3. The direction of this drift changes with the same period as the initial perturbation, which is thus linearly stable. For linear instability the parallel dynamics must be slowed down, leading to a finite, but small, phase shift between plasma pressure and plasma potential perturbations. The possible mechanisms for that are collisions, kinetic effects like Landau damping or magnetic induction [50].

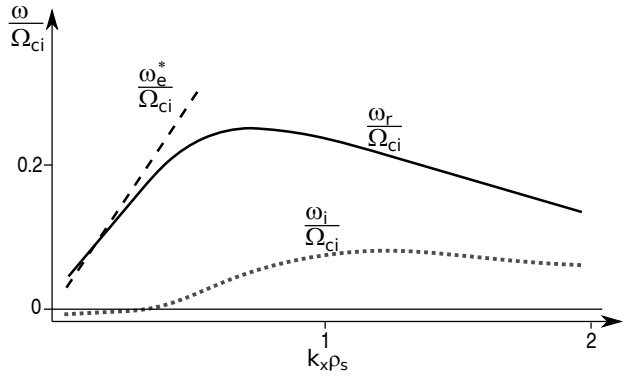

Figure 3.4: Dispersion of the kinetic drift instability as a function of perpendicular wavenumber (adapted from [51]) for the real ω_r and imaginary ω_i parts of the frequency compared to the drift wave frequency ω_e^* (dashed line)

The following dispersion relation can be obtained for drift waves in the electrostatic approximation:

$$\omega_* = \frac{T_e}{eB}\frac{\nabla n}{n}k_x \tag{3.5}$$

where ω_* is called electron drift frequency. The refinements of the dispersion relation 3.5 give rise to complex roots in frequency, i.e. lead to the drift wave instability and damping. The dispersion relation for the kinetic drift instability is shown on Fig. 3.4 against $k_x\rho_s$, where $\rho_s = \frac{\sqrt{m_i T_e}}{eB}$ is the effective ion gyroradius. The real part of the frequency ω_r shows a maximum around $k\rho_s = 1$ (solid line) and the imaginary part ω_i indicates the destabilisation for $k\rho_s > 0.4$ caused by collisions [51].

There are multiple various drift-wave and interchange instabilities in the tokamak plasma, including the trapped electron modes (TEM), the ion temperature gradient mode (ITG), the electron temperature gradient mode (ETG). Their growth rates are

typically peaked, as in Fig. 3.4, around a characteristic scale. Therefore the instabilities can be distinguished by their characteristic frequencies and scales: the ITG and TEM modes have a spatial scale of the order of a few ionic Larmor radii $r_{L,i}$, which corresponds to the perpendicular wavenumbers $k_x r_{L,i} \sim 1$, whereas the ETG modes are of a smaller spatial scale with $k_x r_{L,i} \gg 1$. Above a certain critical gradient, these modes become linearly unstable and grow exponentially. However, their growth is inhibited by a non-linear saturation via coupling between several modes. In the experiments it is difficult to identify the particular driving terms of the turbulence which is also consistent with theory where growth rates and turbulence levels are complicated functions of many different radial gradients.

The importance of the drift wave instability arises from the universality of the spatial gradients in the density and temperature. Thus the drift wave instability can easily convert particle thermal energy into wave energy, leading to turbulence with the increased heat and particle losses.

3.2.2 Turbulent spectra

An incompressible neutral fluid can be described by the Navier-Stokes equation for the fluid velocity $\mathbf{u}$:

$$\frac{\partial \mathbf{u}}{\partial t} + (\mathbf{u} \cdot \nabla)\mathbf{u} = -\nabla p + \frac{1}{R_e}\Delta \mathbf{u}, \tag{3.6}$$

where p is the pressure and R_e is the Reynolds number defined as

$$R_e = \frac{u_0 L \rho}{\nu}, \tag{3.7}$$

where u_0 stands for the mean velocity, L is the characteristic system scale, ρ is the mass density and ν the viscosity. The Reynolds number characterises the degree of non-linear behaviour in the system compared to viscous damping. Low R_e flows are called laminar, for high R_e turbulence develops, where eddies of different sizes are formed. In a magnetically confined fusion plasma similar equations exist for electrons and ions. The plasma turbulence is mainly due to the nonlinear interactions between the eigenmodes described in Sections 3.1 and 3.2.1.

One of the most important quantities to observe is the turbulence energy contained in different scales. As it evolves in time, the turbulent vortices can split or merge. These modifications form cascades, where the cascade towards smaller scales is called direct,

and the one towards larger scales inverse. The turbulent direct cascade characterises the energy transfer to small scales until the smallest scales where energy is dissipated to heat. The first exact mathematical theory of turbulent cascades was developed by Kolmogorov [52]. By a dimensional analysis for homogeneous turbulence Kolmogorov found the function of the energy spectrum $E(k)$ for 3D-turbulence:

$$E(k) = C\epsilon^{2/3}k^{-5/3}, \tag{3.8}$$

where C is a constant and ϵ is the rate of energy dissipation. This 5/3 power law is experimentally observed in turbulent fluids [53]. Figure 3.5 schematically represents the spectral energy against the turbulent wavenumbers k. The size of the structures thus is decreasing for higher k. The energy is injected into the system at some scale k_{inj}, then transferred towards smaller scales in the inertial range and dissipated in the dissipative range.

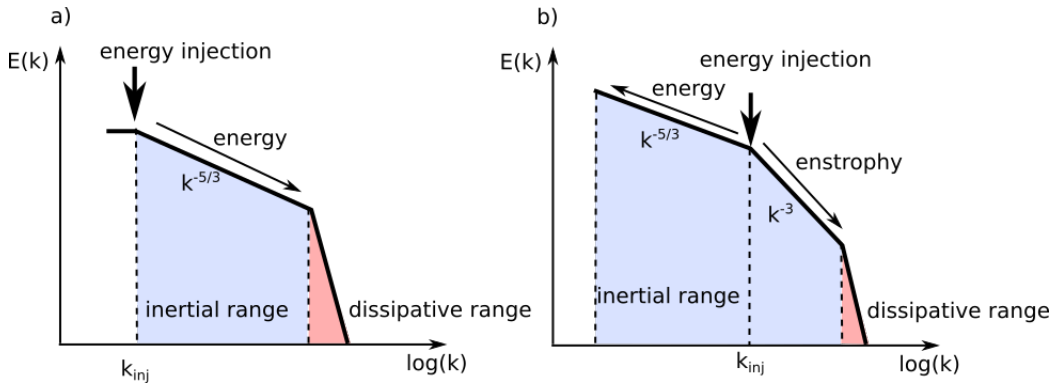

Figure 3.5: Spectral energy for 3D turbulence a) and 2D turbulence b)

Passing to 2D geometry, the effect of vorticity stretching disappears [54], that means that the enstrophy is conserved. The consequence of this conservation is that the energy is transferred towards smaller wavenumbers and the enstrophy – towards higher wavenumbers. The two cascades form a Kolmogorov-Kraichnan-type power spectrum with two prescribed spectral indices (slopes) of -5/3 and -3. The first one is called inverse energy cascade and the second one is the direct enstrophy cascade.

It has been shown in simulations and experiments [55], that in reality different spectral indices may be obtained due to anisotropy, mode coupling, Landau damping etc.. The indices are partially defined by the dominant instability (often ITG, ETG or TEM) with its characteristic size (ρ_i, ρ_e or ρ_s, the ion gyro-radius at the electron

temperature). Nevertheless the spectral description can be used to characterize the turbulence and to make predictions on the turbulence behavior.

For the characterisation of turbulence the width of the wavenumber spectrum $\langle k \rangle$ is used, it is also related to the correlation length L_{cor}. The typical size of the turbulent structures and their correlation time t_c determines the transport coefficient written in a naive way as

$$D_t \approx L_{cor}^2 / t_c, \tag{3.9}$$

which was explained [56] by the flattening of the density, temperature and potential gradients in a region of the size L_{cor}. Equation (3.9) can be refined by more accurate statistical models [57].

3.2.3 Turbulence suppression by shear flow

Flow shear can suppress turbulence as described in [13]. The mechanism acting on turbulent eddies is shown on Fig. 3.6. Without shear the structure would be convected in the flow direction retaining its shape.

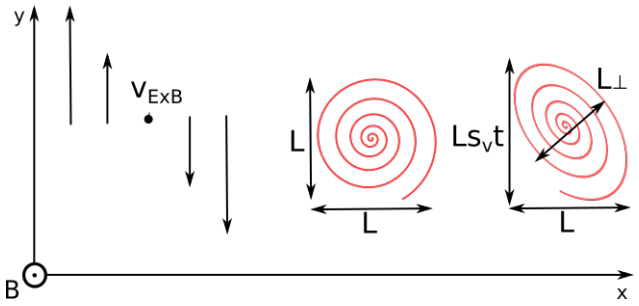

Figure 3.6: Stretching of a turbulent structure by the flow shear

The sheared flow with an $\mathbf{E} \times \mathbf{B}$ velocity in the direction y stretches and tilts an initially circular turbulent eddy of size L. The flow shear

$$s_v = r \frac{\mathrm{d}}{\mathrm{d}r} \left(\frac{E_r}{B} \right) \tag{3.10}$$

acts during a time t and causes the deformation of the eddie to an ellipse with a major axis of the length $\sqrt{L^2 + (Ls_v t)^2}$. The area should be conserved, therefore the minor axis is equal to $L_{\text{eff}} = L \cdot (1 + s_v^2 t^2)^{-1/2}$. Thus this process reduces the eddy correlation

length and the turbulent diffusion coefficient at the scale of the structure correlation time (3.9):

$$D = \frac{L^2}{\tau_c(1 + s_v^2 t^2)} \tag{3.11}$$

Although the structure deformation decreases the radial transport, the turbulence suppression suggests an additional energy transfer. The straining-out process described in [58] establishes the energy transfer from the turbulence to zonal flows. As the shear flow tilts and stretches the turbulent structures, the flow anisotropy produces a Reynolds-stress drive for the zonal flows. In addition the stretching increases the drift waves radial wavenumber and their coupling to the dissipation range becomes stronger.

A zonal flow is a toroidally symmetric band-like shear flow ($n = 0$) including electrostatic potential fluctuations with finite radial wavenumber k_r. Zonal flows are driven by nonlinear interactions, which transfer energy from the drift waves. Consequently the zonal flows reduce the level of turbulent transport. In comparison to the drift waves, the zonal flows have low frequency and wavenumber ($k_r \rho_i \ll 1, \omega_{ZF} = 0$).

3.2.4 Limit-cycle oscillations

The generation of zonal flows happens via the divergence of the Reynolds stress $m_i n \partial_r \langle \tilde{u}_r \tilde{u}_\theta \rangle$, where $\tilde{u}_r = \tilde{E}_\theta / B$ and $\tilde{u}_\theta = \tilde{E}_r / B$ are the fluctuating flows [59]. The energy exchange in this process can be described by the following equation

$$\frac{\partial E_{ZF}}{\partial t} = \langle \tilde{u}_r \tilde{u}_\theta \rangle \frac{\partial u_{ZF}}{\partial r} - \mu E_{ZF}, \tag{3.12}$$

where u_{ZF} stands for the zonal flow velocity, $E_{ZF} = \langle u_{ZF} \rangle^2$ is the zonal flow energy, μ is the total zonal flow damping rate due to ion-ion collisions or parallel viscosity. The stabilization of the drift waves with a broad wavenumber spectrum occurs through a shearing process. The drift wave turbulence energy evolves according to

$$\frac{\partial E_{DW}}{\partial t} = -\langle \tilde{u}_r \tilde{u}_\theta \rangle \frac{\partial u_{ZF}}{\partial r} + \gamma_{eff} E_{DW}, \tag{3.13}$$

with an effective growth rate γ_{eff} which includes the gradient drive, background shear and nonlinear interaction of the modes [60]. The interaction of the zonal flow and the drift wave also can be described by the non-linear wave interaction. In this case the initial drift wave $(\mathbf{k_0}, \omega_0)$ couples to the zonal flow $(\mathbf{k_{ZF}})$ and produces two drift waves which have wave vectors $\mathbf{k_0} + \mathbf{k_{ZF}}$ and $-\mathbf{k_0} + \mathbf{k_{ZF}}$.

The interaction between turbulence and zonal flows in high temperature plasmas has been studied in many experiments [61, 62]. For the experimental observation of the zonal flows, different scales of turbulent structures should be analysed. For this purpose usually a bicoherence analysis is applied in the frequency space. This allows to demonstrate the coupling between turbulence and zonal flows. The geodesic acoustic mode (GAM), being a finite frequency zonal flow, is often identified in this analysis [63]. In order to quantify the zonal flow contribution to the total $\mathbf{E} \times \mathbf{B}$ shear, usually the electric field is measured using the motional Stark effect (MSE) [64], a heavy ion beam probe (HIBP) [65] or charge-exchange spectroscopy (CXRS) [24], where the background mean E_r is estimated from the radial force balance for different plasma species. However, the temporal resolution of these diagnostics is usually lower than the typical time scales of the zonal flows and turbulence dynamics. Doppler reflectometry can provide fast measurements of the flow velocity which has been used for zonal flows studies [11].

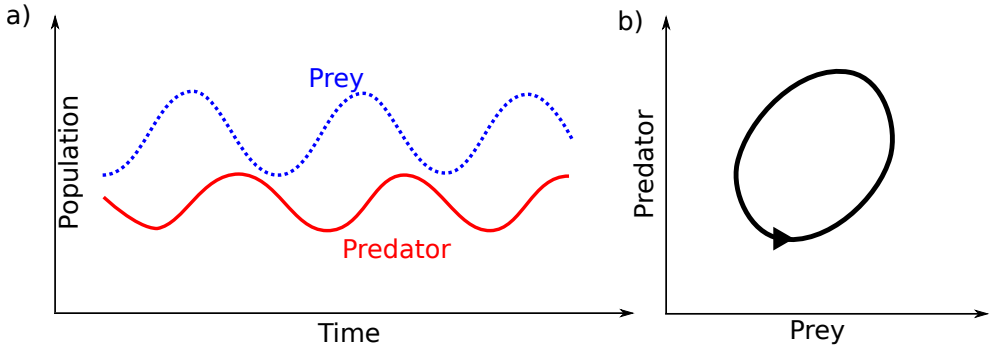

Figure 3.7: a) Time evolution of predator and prey populations, b) relation between the two populations on the phase plane forms a cycle in counter-clockwise direction

The equations (3.12) and (3.13) form a Lotka-Volterra type of system, that describes a predator-prey relation between two quantities, E_{ZF} and E_{DW}, and is often used for the population dynamics in biology. Figure 3.7 depicts the population of two species, the predator (Fig. 3.7a, red solid) and the prey (Fig. 3.7a, blue dashed). The predator population decreases when there is low amount of prey and increases at the maximum of the prey population. The phase behaviour of the two populations is shown in Fig. 3.7b and represents a cycle in counter-clockwise direction. The drift wave turbulence corresponds to the prey, while the zonal flow takes the role of the predator. Although the predator-prey model is a very simplified approach for the interaction of

zonal flows with the turbulence, it helps to better understand the limit-cycle oscillations observed in many experiments.

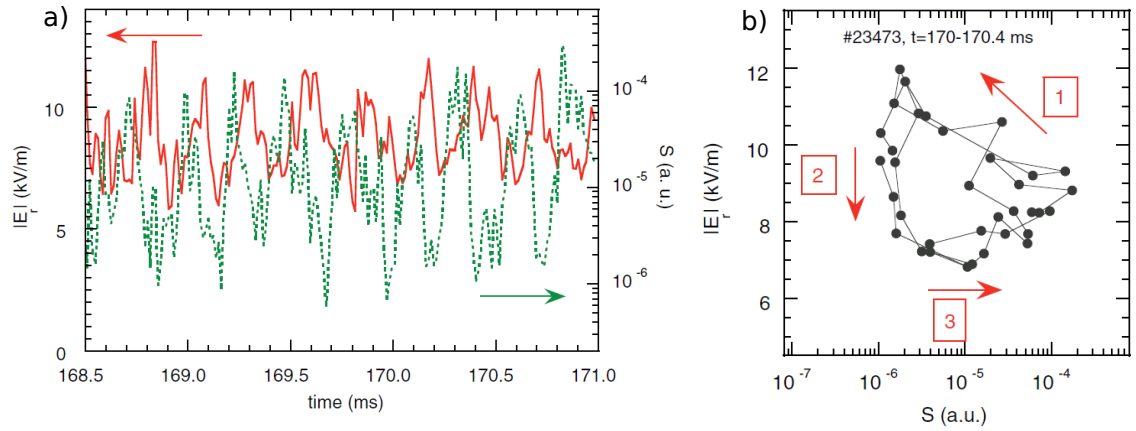

Figure 3.8: a) Time evolution of E_r and density fluctuation level S obtained from Doppler reflectometer measurements, b) relation between E_r and density fluctuation level during two cycles (adapted from [20])

The predator-prey system of equations gives two equilibrium states. The first is the "extinction" of both "species", the second one is a fix point. This system has a characteristic oscillation frequency at $\omega = \sqrt{\gamma_{\text{eff}}\mu}$. The behaviour of the quantities entering the predator-prey model is that the zonal flow energy follows that of the turbulence by $\pi/2$. This has been actively measured and discussed in the fusion plasma community during last decades, but the contradictions are still present. Usually the turbulence level is compared to the radial electric field $E_r = E_r^{neo} + E_r^{ZF}$ consisting of the neoclassical mean electric field E_r^{neo} and the electric field E_r^{ZF} created by zonal flow.

An example of a simultaneous measurement of turbulence intensity and radial electric field on the stellarator TJ-II is shown in Fig. 3.8 during an I-phase. A cyclic trajectory on the plane of radial electric field and turbulence intensity (Fig. 3.8b) indicates a $\pi/2$ phase difference between the density fluctuation level (prey) and radial electric field E_r (predator). The turbulence-induced sheared flow is generated causing a reduction in the turbulent fluctuations (Fig. 3.8b, 1), the drop in the sheared flow follows (Fig. 3.8b, 2) and the increase in the turbulence level ends the cycle (Fig. 3.8b, 3) [20]. Note that the limit cycle oscillations can arise from any energy transfer term related to

turbulence, flows, gradients and other driving terms [66]. Thus, it is extremely difficult to discriminate the main players.

3.2.5 H-mode, turbulence and confinement

The transition from the low (L-mode) to the high confinement (H-mode) regime in a tokamak occurs very rapidly if the heating power exceeds a certain threshold value that depends mainly on plasma average density $\bar{n}_e$, magnetic field strength B and plasma surface area S. Its scaling can be written as [9]:

$$P_{\mathrm{thr},08} = 0.049 \bar{n}_e^{0.72} B_t^{0.80} S^{0.94}. \tag{3.14}$$

However, the physical mechanism that triggers the transition to the H-mode is not understood. The predictions of the conditions for the transition are based on empirical scalings of needed power [67], critical gradients or values of various plasma parameters [68] with a large uncertainty.

One of the most widely accepted theories concerning the L–H transition asserts that the plasma edge is stabilized by increased radial electric field gradients [69]: the $\mathbf{E} \times \mathbf{B}$ shear flow stabilizes drift wave modes and decreases the radial size of turbulent structures. A transport barrier forms in the edge (ETB) where density and temperature gradients increase [8]. The dynamics of barrier formation and of turbulence suppression involves the evolution of both the mean $\mathbf{E} \times \mathbf{B}$ flow as well as the zonal flows. The theory suggests that first the turbulence level grows in the edge and the turbulent modes begin to transfer energy to zonal flows. The zonal flow then starts to grow and by the shearing mechanism extract kinetic energy from the drift waves and thus decreases the associated turbulent transport. The confinement improves because of the reduced radial transport. The pressure gradient is then increased together with the neoclassical electric field. The neoclassicale electric field is a result of an initially Maxwellian distribution in the presence of temperature and density gradients, which evolves into a regime with a deep radial electric field well in the region of the ETB, creating a background flow shear. In this model the zonal flows trigger the transition to a lower turbulence level, while the increased neoclassical ∇E_r reduces the remaining turbulence. Without sufficient turbulent drive, the zonal flows disappear.

If the input power is just below the L-H transition threshold, limit-cycle oscillations occur between the turbulence and flows that indicate the presence of the predator-prey

mechanism. Despite some experimental evidencies of the interaction between zonal flows and turbulence, the experimental results differ from one device to another and do not allow a definitive conclusion. Some of experimental results are discussed in Chapter 6. The fast time scale of the L-H transition and limit-cycle oscillations complicates the identification of the causality.

The first theoretical model linking the confinement transition and the electric field was proposed by K.Itoh and S.-I. Itoh [70] in 1988. Their model introduces a bifurcations in E_r, particle flux and energy loss at the plasma edge. The shearing mechanism was described in [13] in order to explain the reduced turbulent transport. In 1994 the coupling of the turbulence and shear flows through the Reynolds stress was discussed [16]. Numerous investigations of the turbulence in tokamak plasma have not fully revealed its properties and mechanisms. For these studies it is necessary to measure the main plasma parameters and their fluctuations : electron and ion temperature, density, electric field with the typical time scale of microseconds. To identify experimentally which underlying instabilities determine the confinement transition, one should measure the turbulence driving gradients and the resulting turbulence spectra with a high spatial resolution of millimetre range. In this work we investigate the turbulence behaviour using density fluctuation measurements from an ultra-fast swept reflectometer at AUG. Combining the UFSR electron density measurements with 1 μs resolution with the ECE electron temperature data averaged over 100 μs, it is possible to follow the dynamics of the neoclassical electric field, which can be compared with the evolution of the flow velocity measured with the Doppler reflectometer backscattering system. The detailed comparison is essential in understanding of the mecanisms of L-H transition.

4 ASDEX Upgrade and diagnostics for temperature, density and electric field measurements

The experiments described in the following chapters have been performed at the ASDEX (Axial Symmetric Divertor EXperiment) Upgrade (AUG) tokamak. In order to study the turbulence behaviour during the L-H transition, precise measurements of the electron and ion density and temperature are needed as shown in the previous chapter along with the edge radial electric field. AUG disposes a set of diagnostics necessary to study and to attempt a better understanding of the turbulent phenomena in fusion plasmas. This chapter summarises the main diagnostics methods commonly used at AUG, upon which this thesis is based. Electron density is measured by the DCN interferometer, vertical Thomson scattering (VTS), lithium beam emission spectroscopy system (LiBES) and reflectometry. Electron temperature is available from Thomson scattering and electron cyclotron emission (ECE) data. Ion density and temperature as well as the flow velocities can be measured with the charge exchange recombination spectroscopy (CXRS). Using the radial force balance (2.10) the radial electric field is found from these parameters. Doppler backscattering system (DR) with several fixed frequency channels provides an alternative for the $\mathbf{E} \times \mathbf{B}$ flow velocity measurements [71]. Poloidal correlation reflectometry is able to measure the poloidal velocity of fluctuations [72]. Reflectometry will be discussed in details in Chapter 5 as the main method used in this work.

4.1 ASDEX Upgrade tokamak

AUG is a middle-size tokamak device located at the Max Planck Institute for Plasma Physics in Garching. AUG has a poloidal divertor and a system of 12 poloidal and

16 toroidal magnetic field coils. The toroidal magnetic field is 1.8–3.1 T. The plasma current can vary in the range 0.4–1.6 MA. The plasma discharge lasts up to 10 s.

The major radius is 1.65 m, the plasma minor horizontal radius is about 0.5 m and

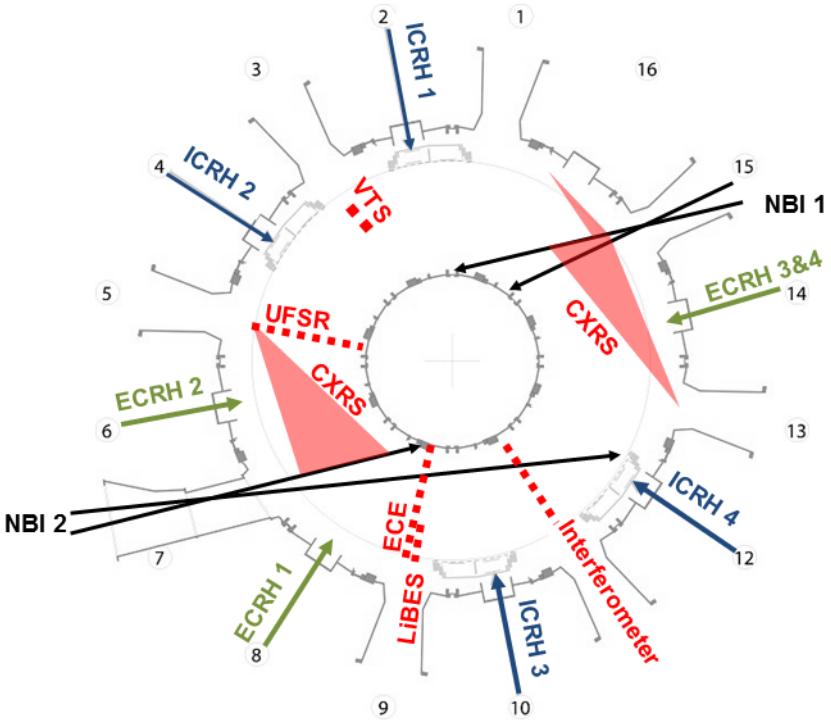

Figure 4.1: The heating systems at ASDEX Upgrade, top view: ECRH, ICRH and NBI and diagnostics lines of sight: CXRS, interferometer, LiBES, ECE, UFSR, VTS

the vertical plasma radius is 0.8 m. Plasma discharges are created with D, H or He as main species. The plasma density can reach up to 10^{20} m^{-3}. The main parameters of AUG are listed in Table 4.1.

It is convenient to describe the tokamak plasma geometry in terms of the magnetic flux surfaces. The magnetic surfaces are surfaces of constant pressure too, because $\mathbf{B} \cdot \nabla p = 0$. The normalized radius ρ_{pol} is defined by the poloidal magnetic flux Ψ:

$$\rho_{pol} = \sqrt{\frac{\Psi - \Psi_{axis}}{\Psi_{sep} - \Psi_{axis}}}. \tag{4.1}$$

Ψ_{sep} is the poloidal flux at the LCFS and Ψ_{axis} is the poloidal flux at the plasma magnetic axis. Thus ρ_{pol} can vary from $\rho_{pol} = 0$ in the plasma centre to $\rho_{pol} = 1$ at the

Experiment total height	9 m
Total radius	5 m
Major plasma radius R_0	1.65 m
Minor horizontal plasma radius a	0.5 m
Minor vertical plasma radius b	0.8 m
Number of toroidal field coils	16
Number of poloidal field coils	12
Maximum magnetic field	3.1 T
Plasma current	0.4–1.4 MA
Pulse duration	<10 s
Time between pulses	15–20 min
Elipticity b/a	1.8
Triangularity (top/bottom)	0.4/0.4
Plasma types	deuterium, hydrogen, helium
Plasma volume	13 m^3
Electron density	$< 10^{20}$ m^{-3}
Plasma temperature	< 250 million degree

Table 4.1: ASDEX Upgrade technical data and typical parameters

separatrix. The shape and position of the plasma in AUG are controlled by vertical field coils. The most common plasma configuration in AUG is the Lower Single Null (LSN) shape, which is shown in Fig. 1.2 with an X-point at the bottom, next to the divertor. A typical LSN discharge has a low upper triangularity (more round plasma shape at the top of the cross-section) and a high lower triangularity. The plasma current produces Ohmic heat due to finite resistivity, but this heat is not sufficient for reaching fusion relevant conditions. Therefore auxiliary heating systems supply additional 30 MW of heating power. The heating systems consist of Ohmical heating of 1 MW, neutral beam injection (NBI) heating up to 20 MW with the deuterium atoms of 60 and 100 keV energies, ion-cyclotron resonance heating (ICRH) of up to 6 MW (30–120 MHz) and electron-cyclotron heating (ECRH) of up to 4 MW (105 or 140 GHz). The maximum power applied in a plasma discharge is limited by the generators' capacity. Figure 4.1 depicts the schematic top view of AUG with the position of the heating systems and several plasma diagnostics described in this chapter. The tokamak sectors are numbered

from 1 to 16. The NBI heating is based on the ionisation of the high-energy neutral particles by collision with the plasma particles resulting in a population of fast ions. The fast ions then transfer most of their energy by further collisions to the thermal particles. This heating method introduces an additional toroidal momentum in a plasma. The ICRH also increases the kinetic energy of the resonant ions, whereas ECRH launches microwave beams absorbed by the plasma electrons.

4.2 Equilibrium reconstruction at ASDEX Upgrade

In order to use all diagnostic data in the same coordinate system, an equilibrium of plasma magnetic surfaces should be reconstructed for each time point. There are two standard methods for the equilibrium reconstruction at AUG used for all plasma discharges. The first one, function parametrisation, reconstructs the flux matrix and various plasma parameters from a linear regression of magnetic measurements. The coefficients of regression are determined using a database of several thousand ideal equilibria. This method is fast and therefore used for the first check of the plasma equilibrium. The second method, CLISTE, is more accurate and used for a detailed analysis [73]. The CLISTE code searches for an optimal equlibrium to a set of measurements by solving the force balance equation (1.4) together with Maxwell's equations. CLISTE uses the assumption of toroidal symmetry of the flux surfaces, neglecting the ripple created by the finite number of magnetic field coils. This assumption results in a spatial resolution of the mapping from absolute coordinates to the normalised radius ρ_{pol} of the order of few millimetres. The temporal resolution is of 100 ms for the equilibrium named EQI and of 1 ms for EQH.

4.3 Laser interferometer

For electromagnetic wave frequencies larger than the plasma frequency $\omega_{pe}/2\pi$ ((2.14)), the refractive index is very close to 1. However the phase difference is measurable using the interference between a reference laser or microwave beam in vacuum and the beam crossing the plasma along coordinate l with respect to the vacuum wavelength λ:

$$\Delta\Phi = \frac{\lambda e^2}{4\pi c^2 \epsilon_0 m_e} \int n_e(l) \mathrm{d}l. \tag{4.2}$$

It is sufficient to detect the phase shift in order to deduce the density integrated over a line of sight. The choice of the wavelength λ (between 10–2000 μm) is the result of a compromise between the effects of mechanical vibrations affecting the short wavelengths and the effects of refraction of the beam by the transverse density gradients, affecting long wavelengths. In AUG the interferometer uses a deuterium cyanide (DCN) laser with a wavelength of 195 μm and has 5 lines of sight in the sector 11 (Fig. 4.1). If the line densities (in m^{-2}) are measured very precisely, the radial profile is less precise. Its reconstruction by Abel inversion requires a hypothesis on the location of the iso-density surfaces. Note that due to this imprecision on the reconstruction of the radial profile, it is not possible to calculate electron density gradients from the interferometry measurements, especially in the plasma edge. Nevertheless, the interferometer allows real-time measurements of the density which are used for the plasma control. The density profile is calculated each 1 ms. The complete description of the interferometry diagnostics installed on ASDEX Upgrade can be found in [74]. In this work interferometer will be used for the cross-comparison of the density profiles and for the real-time density control during the discharges.

4.4 Electron cyclotron emission radiometer

The electron temperature measurement by the Electron Cyclotron Emission (ECE) is a common diagnostic in all current large tokamaks. It measures the radiation emitted by the electron gyro-movement at the electron cyclotron frequency $\Omega_{ce} = eB/m_e$ and at its higher harmonics $n\Omega_{ce}$. In AUG a 60-channel heterodyne radiometer is installed for the measurement of the second harmonic of X-mode ECE along a radial horizontal line of sight (Fig. 4.1) with a sampling rate of 1 MHz [75].

In case of an optically thick plasma its equilibrium temperature can be considered constant in the emitting element and the emission density of its surface in all directions is the same and corresponds to the equilibrium value from Planck's formula for blackbody emission $I(\omega)$:

$$I(\omega) = \frac{\omega^2 k_B T_e}{8\pi^3 c^3}, \tag{4.3}$$

where k_B is the Boltzmann constant [76]. In this case the radiation temperature approaches the electron temperature T_e.

The optically thick plasma approximation is usually justified in the AUG core plasma,

but in the optically thin plasma edge often a 'shine-through' peak is observed. This phenomenon is manifested in the increased radiation temperatures in the optically thin scrape-off layer caused by strongly down-shifted radiation of Maxwellian tail electrons located in the edge region. The shine-through effect can be corrected with the integrated data analysis which applies Bayesian probability theory for joint analysis of the electron density and temperature with data of different interdependent and complementary diagnostics [75]. By this means, the electron cyclotron radiation intensity delivers millimeter-resolved electron temperature data for the plasma edge with the temporal resolution of about 100 μs.

4.5 Thomson scattering

Electron temperature and density can also be obtained from the Thomson scattering of a laser beam on plasma electrons [77]. The scattered radiation frequency spectrum is shifted due to the Doppler effect. The Doppler width of the spectrum is proportional to the electron temperature, while the radiation intensity is proportional to the electron density. In AUG the Thomson Scattering System (VTS) collects data from two vertical lines of sight (Fig. 4.1) in the plasma edge and the core. The laser beam allows high localisation of the scattering volumes of 3 mm^3 and 25 mm^3 in the edge and in the core, respectively. The acquisition uses 26 channels providing a centimeter spatial resolution. The temporal resolution is due to the signal integration and is of 3 ms for the edge system and 8 ms for the plasma core [78]. The VTS system is not appropriate for fast dynamics measurements, but is essential for the profile cross-checking.

4.6 Lithium beam emission spectroscopy

The lithium beam emission spectroscopy (LiBES) measures the plasma edge density with high temporal and spatial resolution. The density fluctuation can be measured by LiBES, too. It has high sensitivity in the scrape off layer (SOL) which decreases towards the plasma core. The diagnostic is based on the interaction between the plasma and the neutral lithium beam injected in the sector 9 (Fig. 4.1) with an energy of 15–100 keV. The collisions between the plasma particles and the Li atoms excite Li high energy atomic states and ionise the atoms. The state Li_{2p} is the most populated

and the photon produced by its relaxation creates the spectral line measured by a spectrometer. From the line intensity the electron density profile is reconstructed using a probabilistic lithium beam data analysis based on the Bayesian probability theory [79] with a temporal resolution down to 5 μs and a radial resolution of about 6 mm.

4.7 Charge exchange recombination spectroscopy

This diagnostic of main ions or impurities temperature, density and velocity is based on the measurement of the radiation produced by the charge exchange processes between the plasma ions and neutrals from the neutral beam (NBI used to heat the plasma). The principle of the charge exchange recombination spectroscopy (CXRS) is to measure the radiation of the spectral lines produced by charge transfer from a neutral atom to an excite state of the ion. The radiation spectra have a Doppler shift because of the ion velocity. The ion temperature and the flow velocity are then obtained from the Doppler peak width and shift. The density of an impurity is calculated from the intensity of the emission line.

The CXRS diagnostic in AUG analyses the charge exchange between low-Z impurities like boron, helium or nitrogen and injected neutrals from the heating beams NBI1 and NBI2 (see Fig. 4.1). The use of NBI blips is required in order to get a sufficient level of the radiation intensity. Toroidal and poloidal lines of sight enable to measure the poloidal and toroidal projections of the ions velocity. Thus, through the radial force balance equation (2.10), the radial electric field can be estimated. The radial force balance is established when the distribution functions of the impurity and of the main ion become Maxwellian with the same temperature T_i. This time is about 50–100 μs [24]. The highest temporal resolution of E_r estimation is about 100 μs. This measurements can be compared to the Doppler reflectometry measurements described in Chapter 4.10.

4.8 Magnetic pick-up coils

Pick-up or Mirnov coils allow to observe the perturbed magnetic field by measuring the currents induced by the variation of magnetic field components. The fluctuation of the poloidal (B_θ) and radial (B_r) magnetic field components can be found, since the

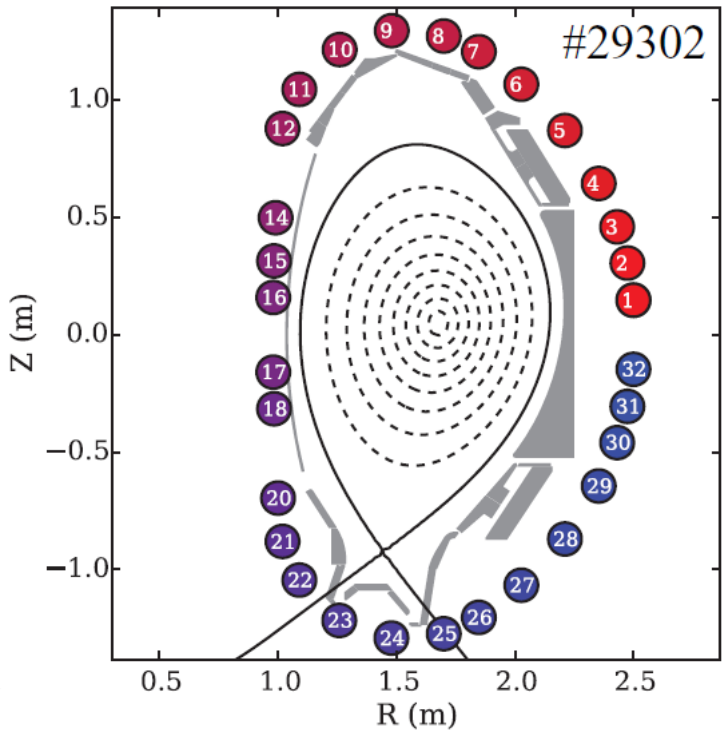

Figure 4.2: AUG poloidal cross-section with the set of magnetic pick-up coils C09-1–32 measuring $\dot{B}_\theta$ (adapted from [80])

induced current is proportional to the temporal derivative of the magnetic field. The measurement is well localized in poloidal and toroidal angles, but corresponds to any radial location of the perturbation. Moreover, the pick-up coil signal can be affected by currents in the vessel components. The Mirnov coils are heat sensitive and therefore can be used only outside the plasma. However this diagnostic has several advantages: simple calibration, high sensitivity ($10^{-4} - 10^{-5}$ T), high number of coils available at different poloidal and toroidal locations [81].

The pick-up coils are used to determine the frequency of plasma modes. Toroidal n and poloidal m mode numbers can be found from the phase difference between two coils signals $\Delta\phi_{mode}$. For example, if the toroidal angle between two Mirnov coils is $\Delta\phi$, the toroidal mode number is deduced from the relation

$$n\Delta\phi = -\Delta\phi_{mode}. \tag{4.4}$$

This relation is ambiguous (modulo the number of the distance between two coils in 2π), i.e. if the toroidal angle between the coils is for instance $\pi/2$, the highest detectable

$n_{max} = 4$. In addition if the mode propagation direction (co- or counter-current) is unknown, only a couple of positive and negative mode numbers satisfying $n_1 - n_2 = 4$ can be obtained.

The system of pick-up coils in AUG includes two poloidal sets of 32 Mirnov's coils (Fig. 4.2) and additionally 6 coils mounted at different toroidal positions in the mid plane measuring $\dot{B}_\theta$, one toroidal set of 6 coils from the low-field side and 2 saddle loops mounted at the high-field side of the vessel measuring $\dot{B}_r$. Different coils will be used in this thesis for the description of edge plasma oscillations.

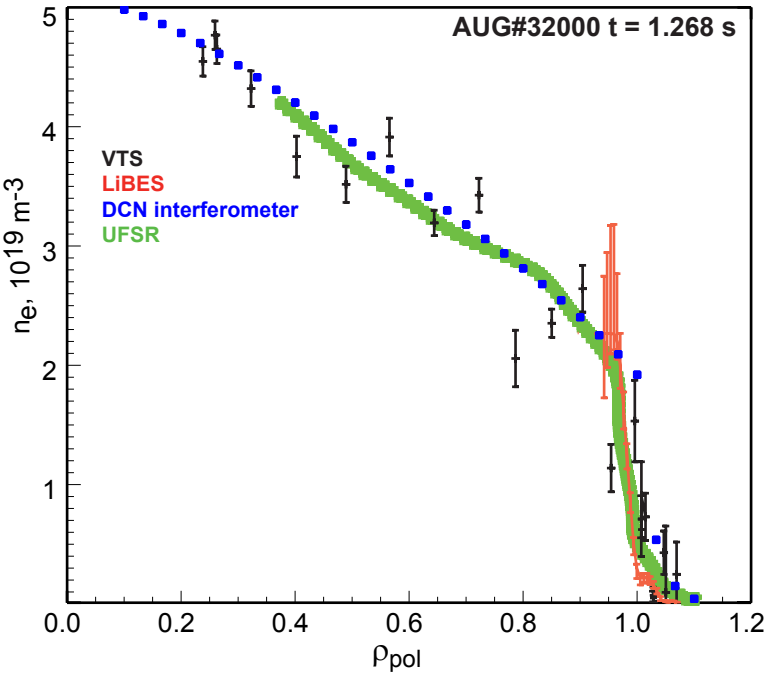

Figure 4.3: Electron density profile diagnostics cross-comparison: Vertical Thomson Scattering (black solid), LiBES (red solid), DCN interferometer real-time data (blue points) and Ultra-fast swept reflectometer (green points)

4.9 Profile reflectometers

In AUG two systems of profile reflectometry are installed. The FM-CW reflectometer in O-mode in the sector 6 provides electron density profiles by sweeping the probing frequency in 20 μs. It has antennas installed both on the low magnetic field side (LFS)

and the high field side (HFS). The same system can be programmed for a fixed probing wave frequency and therefore produce density fluctuation frequency spectra. The main characteristic of the density measurement by the reflectometry is the high sub-centimetre precision of the profile allowing a precise calculation of the local gradients.

The ultra-fast swept reflectometer is installed in the sector 5 and provides temporal resolution of 1 μs. The principle of the reflectometry measurements is detailed in Chapter 5. The density profiles from the aforementioned diagnostics are presented in Fig. 4.3. Because of the mapping uncertainties the profiles should be manualy shifted within few millimetres relatively to each other. In this example LiBES was shifted by 5 mm inwards while VTS edge measurements were shifted 1 cm outwards. LiBES has very large error bars in the region $0.95 < \rho_{pol} < 1$, VTS density values are strongly scattered and few edge channels don't give adequate values, the real-time interferometer data fit well the edge and SOL values from VTS and LiBES and give reasonable central density, the Ultra-fast swept reflectometer agrees with the set of other diagnostics and has an advantage of simultaneous precise measurement of the edge and core plasma density.

4.10 Doppler reflectometer

The Doppler reflectometry backscattering system provides measurements of density fluctuation characteristics with good spatial resolution at selected perpendicular wavenumbers. The probing wave is launched in oblique incidence with respect to the normal vector to the surfaces of constant refractive index. In this case only the signal backscattered on density fluctuations close to the turning point is detected. Due to thevelocity of the turbulent structures, perpendicular to the magnetic field lines, the received signal is Doppler shifted by $\omega = \mathbf{k} \cdot \mathbf{v} = k_{\|} v_{\|} + k_r v_r + k_{\perp} v_{\perp}$ [71]. The parallel component is usually small, the radial velocity can become important during relaxation of the pedestal density, as it happens during ELMs or filaments expulsion. Otherwise the extracted velocity $v_{\perp} = \omega / k_{\perp}$ is assumed to correspond to the perpendicular velocity of the density fluctuations in the laboratory frame, $v = v_{E \times B} + v_{ph}$, where $v_{E \times B}$ is the $\mathbf{E} \times \mathbf{B}$ velocity and v_{ph} is the phase velocity of the fluctuations. It has been shown in several experiments that the phase velocity is small compared to the $\mathbf{E} \times \mathbf{B}$ velocity at the edge of a stationary plasma [82, 83]. Hence the Doppler shift is used as a direct measurement of the $\mathbf{E} \times \mathbf{B}$ flow and thus of the radial electric field. Several Doppler systems installed

on AUG have in total five channels, 4 operating in V-band [84] frequency range and 2 in W-band [85]. The radial position of the cut-off and the wavenumber for the probing wave are found from the 3D beam tracing code TORBEAM [86] simulating the propagation of a Gaussian beam in a stationary plasma. To extract the Doppler shift on a fast time scale the multiple signal classification (MUSIC) algorithm is used [87], with a typical window length of about 1.5 to 3 μs, together with the spectrogram analysis (fast Fourier transform on short sliding windows of about 10 μs). The evaluation of the velocity is done only for times when the signal amplitude exceeds a threshold set at about three times the noise level. This limits E_r measurements to plasmas where turbulence is not suppressed too strongly.

5 Ultra-fast swept reflectometry

Plasma microwave reflectometry, being a radar-like technique, is based on the dependence of the plasma refractive index on the electron density. A probing wave propagates in an inhomogeneous plasma until it reaches the so-called cutoff layer where it gets reflected, i.e. the refractive index is zero. As the position of the cutoff depends on the wave frequency as it was shown in (2.18) and (2.19), the plasma density can be measured at different magnetic surfaces. Thus, an electron density radial profile can be reconstructed. However the magnetic field intensity is needed for X-mode and the electron temperature profile is required to take into account the relativistic corrections mentioned in Chapter 2.2. The Doppler effect seen on the reflected signal is usually exploited to measure the velocity of fluctuations, which scatter back the probing wave. Reflectometry was first used for the radiowaves reflected from the ionosphere [88] and now is widely applied for laboratory plasmas [89]. For this the probing frequency range should be adapted to the plasma frequency for O-mode and electron cyclotron frequency for X-mode. Different reflectometers for electron density profile and density fluctuations measurements have been overviewed by [90] and [91]. The history of the ultra-fast swept reflectometer systems will be given in section 5.1 together with the description of its design and installation at AUG. Section 5.2 summarizes the methods of reflectometry applied in this work. The UFSR has been the main diagnostic used in the experiments on L-H transitions and edge coherent modes, as it will be described in Chapter 6 and 7.

5.1 Ultra-fast swept reflectometer history and design

5.1.1 UFSR history

The first concept of a reflectometer for density profile measurements in a tokamak appeared in the late 70s and developped in the 80s [92]. By using several frequencies of

the probing wave, the electron density profile can be reconstructed. The first frequency-modulated continuous-wave (FM-CW) reflectometry measurements were performed at CEA on the tokamaks TFR [93] and Petula-B [94]. If the wave frequency is modulated, the wave propagation introduces a time dependant phase shift containing the beat frequency:

$$\Delta\Phi = \Phi - \Phi_0 = 2\pi F_{\text{beat}} t \tag{5.1}$$

The beat frequency is proportional to the time of flight of the probing wave:

$$F_{\text{beat}} = \tau_{\text{flight}} \frac{dF_{\text{wave}}}{dt} \tag{5.2}$$

This type of diagnostic was installed shortly after at many other fusion devices (ASDEX [95], TFTR [96], JET [97], JT60 [98], URAGAN-3M [99]). The next step in the reflectometry development was to improve the signal quality. The FM-CW systems needed a minimum frequency modulation speed (linearly sweeping or hopping with several steps) speed to be high enough to measure one profile faster than at least the typical MHD oscillations (order of 1 ms). In the best case the frequency scan must be faster than typical turbulence time scale (less than 10 μs). Therefore, two approaches started to develop. The first one, of the sweeping reflectometry, used a single frequency wave, linearly swept through a continuous broadband frequency range. As the duration of the sweep was of the order of milliseconds, this method struggled from the phase perturbation due to density turbulent fluctuations. Coping with this problem, the sweep time evolved from milliseconds to 1 μs nowadays. One of the advantages of the broadband sweeping systems is the high spatial resolution. The second approach, of the pulse reflectometer, was used in military and civil radar applications. This method exploits the relation between the pulse width and its bandwidth: $\Delta F \Delta t = 1$. A short pulse allows to obtain a broad frequency range and thus scan a large plasma region. The measured quantity is the pulse time of flight. The optimum pulse duration is a compromise between the frequency bandwidth (and thus the plasma region width) and the resolving capacity for the time of flight measurements linked to the signal-to-noise ratio [100].

The ultra-fast swept reflectometer (UFSR) comes from the "family" of reflectometers developed for Tore Supra. The first generation of homodyne reflectometers worked with O-mode polarisation in the bands 25–35 GHz, 35–50 GHz and 50–75 GHz. Backward Wave Oscillators (BWO) were used as the source of probing waves and limited the

sweeping rate at 1 ms. In 1994 a reflectometer of a "new generation" in the range 26–36 GHz was built at CEA using the heterodyne detection and a solid state oscillator [101].

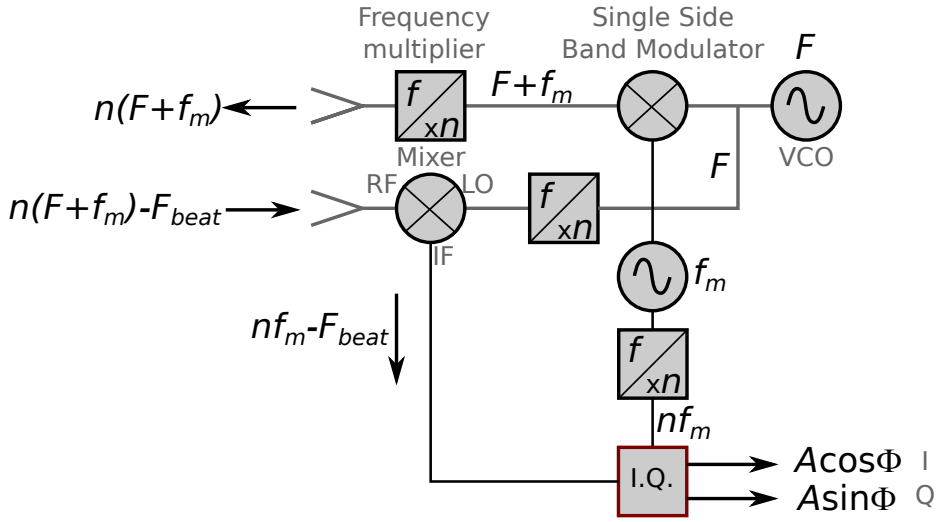

Figure 5.1: Heterodyne reflectometer design

Heterodyne reflectometry method was first applied to fusion plasma by Vershkov in the T–10 tokamak [102]. The principle of the heterodyne detection compared to the homodyne scheme is to mix the signal carrying the beat frequency with a low frequency modulation. The Fig. 5.1 depicts a typical design of a heterodyne reflectometer used for the swept reflectometers developed in CEA. The probing wave with swept frequency (12–20 GHz) is generated by a voltage controlled oscillator (VCO). VCOs are able to provide sweeping as fast as 20 GHz/μs, but also produce a relatively high noise.

The signal is separated in two parts: one launched into the plasma (RF) and the other serving as a reference signal (LO). The single side band modulator (SSBM) adds a modulation frequency f_m to the main frequency F. Before launching the probing wave to the plasma through the emitting antenna, its frequency is multiplied by n, in the case of V- and W-band equal to 4 and 6 respectively.

After the reflection from the cutoff layer, in the case of bistatic system the wave is received by the second antenna. If the launching antenna is also the receiver then we speak about a monostatic system. The reference signal (also multiplied by n) compensates the propagation of the probing wave into the wave guides and mixes to the reflected probing signal. At the mixer output the signal (IF) contains only $F_{\mathrm{beat}} + nf_m$

frequency. The shift of the signal by the carrying frequency nf_m ensures the good signal quality [103]. This is based on the fact that the noise decreases as $1/F$, so as the signal is far from $F = 0$, we improve the signal-to-noise ratio. At the end the modulation frequency is removed and an I/Q detector is used to separate the two parts of the signal shifted by $\pi/2$. This separation allows to measure independently $A\cos\Phi$ and $A\sin\Phi$, where A is the signal amplitude. Extraordinary polarisation (X-mode) was applied first in the range 50–75 GHz (1999) and in the range 75–110 GHz (2001) and covered a broad region of the plasma in the edge for various operating conditions. To rebuild the density profile the electron cyclotron frequency should be included in this frequency range, which requires the magnetic field intensity lower than 4 T but also greater than 2.4 T to include the reflection from the plasma edge. The acquisition system also significantly changed from 40 acquisitions to 10,000 in 2002 and 200,000 in 2015. The turbulence measurements extracted from the phase fluctuation became possible after improving the signal-to-noise ratio to about 30 dB. This was first described in the thesis [104] and in a more systematic way in [105]. At this stage the sweep time was of 20 μs, still too long to access the correllation time of the turbulent structures.

5.1.2 UFSR installation at ASDEX Upgrade

The V- (50–75 GHz) and W-band (75–110 GHz) ultra-fast swept reflectometers on AUG are a result of the upgrade of the acquisition system and of the increased modulation frequency [106]. The sweep time decreased to 1 μs. That ensures to have more or less a frozen density profile including the density fluctuations over the probing time. In such conditions only the spatial density variations are able to scatter the probing wave. This provides the access to the wavenumber spectrum reconstruction from the phase variations.

The reflectometers were transferred frome Tore Supra to ASDEX Upgrade in 2013-2014. The receiving and emitting bistatic antennas were manufactured at IPP and installed on the tokamak equatorial plane at the low-field side of the sector 5 (Fig. 4.1) with a horizontal line of sight (Fig. 5.2a). At the same time some hardware changes were made to improve the signal amplitude by reducing the losses in the waveguide.

The bistatic antennas are shown in Fig. 5.3a. They have an optimised pyramidal shape and are fed by oversized square waveguides of 10×10 mm (Fig. 5.2b). The square waveguides have a smooth horn transition to the circular waviguides (Fig. 5.2b)

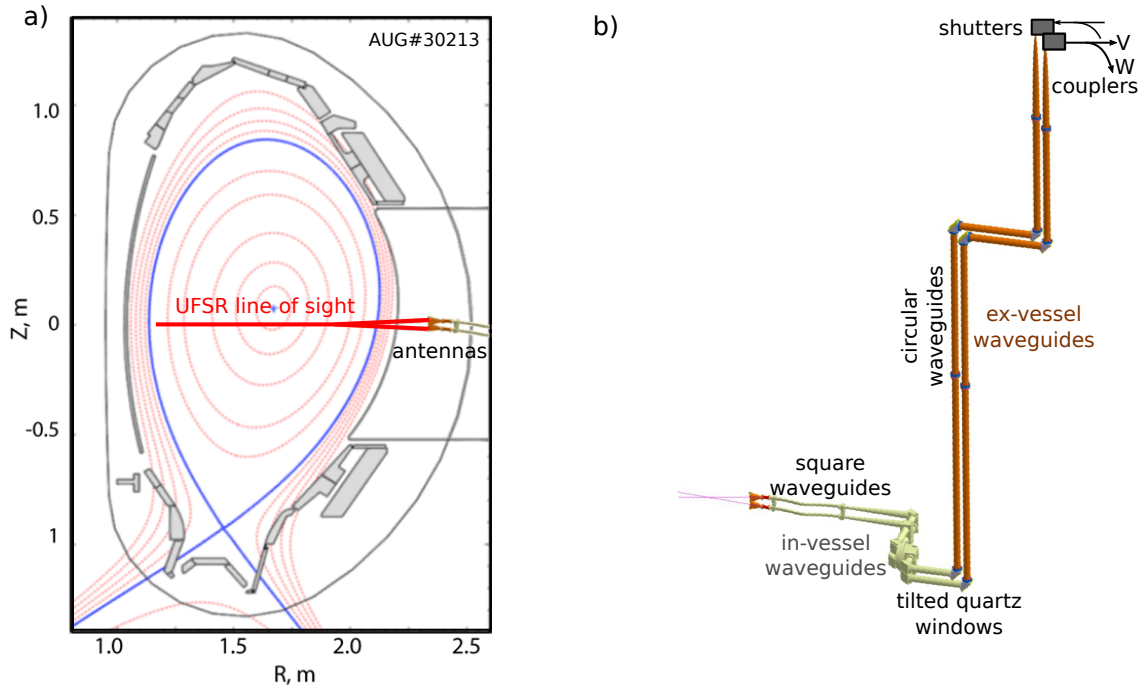

Figure 5.2: a) The position of the UFSR line of sight on the poloidal cross-section of AUG and b) the transmission line including the in-vessel and ex-vessel parts

with diameter of 38 mm and about 5 m length. The vacuum break separating the in-vessel waveguides from the ex-vessel ones is made with the tilted quartz fundamental rectangular windows.

The ex-vessel waveguides are connected to the V-band directional couplers and to the microwave hardware (Fig. 5.3b) schematically shown in Fig. 5.1 through the low-pass filters at 102 GHz (Fig. 5.3b) which were installed for the additional protection. The shielding copper box (Fig. 5.3b) is electrically isolated from the antennas and the waveguides in order to reduce parasitic signals. To avoid the damage of the system during the plasma discharges with possible ECRH stray radiation, two pneumatic switches, used as shutters (Fig. 5.2b), were installed for the emitting and receiving lines. The switches can be open and closed from the AUG control room. Tests of stray radiation were made during 2014 with a detector in sector 5 and a relatively safe power level of the order of milliwatts was measured.

Figure 5.4 depicts the scheme of control of the UFSR. To sweep the probing wave

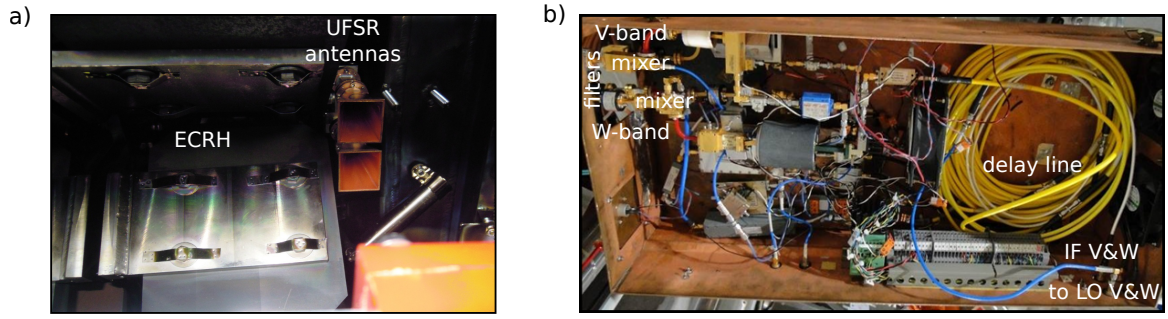

Figure 5.3: a) The UFSR antennas in AUG vessel, b) microwave hardware, the recieving part for V- and W-band is visible on the upper level, the cupplers are connected to the left of the copper shielding box to the low-pass filters, the cables to the right are connected to the VCOs and SSBM (LO and IF) which are outside of the box in a separate cabinet with the acquisition system and the frequency sweep generators

linearly, two arbitrary waveform generators (Tabor) send periodic signals, calibrated with a frequencymeter in the range of 0–2 V, programmed through a GPIB (General Purpose Interface Bus) and amplified (×10), to the VCOs (Fig. 5.4). Thus the oscillators change the frequency in the range of 12–20 GHz. The sweep time during 2013–2015 was of 2 μs before reaching the world record of 1 μs in 2015. As the oscillators need a "dead" time to reset the frequency from 20 to 12 GHz, at the end of each sweep a smooth decrease of the voltage is programmed during 0.25–1 μs. Special attention was paid to the voltage that should have only positive values. The rest of the scheme shown in Fig. 5.4 has been installed in 2013–2014 during the performance tests of the UFSR in the AUG environment.

5.1.3 UFSR perfomance tests

The VCOs send high-frequency sweeps to the reflectometers where the signal frequencies are multiplied by 4 and by 6 for the V- and W-band, respectively, and the heterodyne intermediate frequency f_m is added (Fig. 5.1). The reflected signals mixed with the references are separated with the I/Q detector in $A\cos\Phi$ and $A\sin\Phi$ for both bands and therefore the acquisition card uses 4 channels with the acquisition rate of 1 or 2 Gsample/s (10 bit digitisation). The signal is discretised in 1000 or 2000 points, which provides a sub-millimetre spatial resolution of the plasma density. The time delay between the reference signal and the signal coming from the plasma was suppressed by

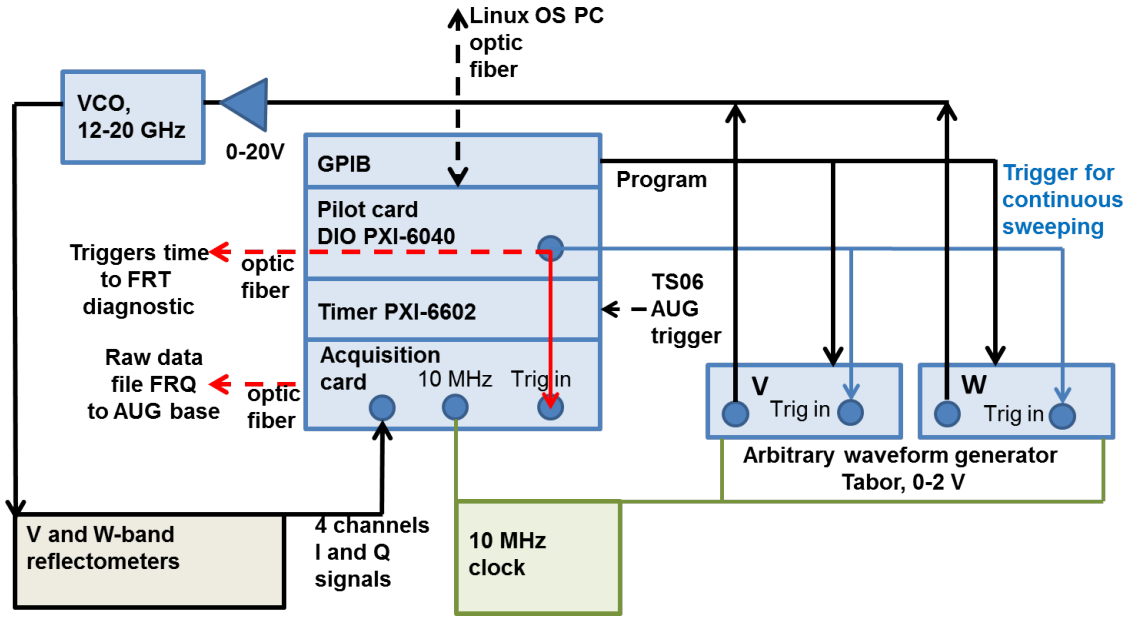

Figure 5.4: Control and triggering scheme of UFSR

adding corresponding 14 m compensating lines (Fig. 5.3b) of cable in the LO part 5.1). The delay between a trigger at the VCO and the signal at the mixer was measured. Figure 5.5 shows the difference of 110 ns between the trigger at the generator and its output voltage and the reflectometer signal start. Thus the acquisition should be delayed by the same amount.

By February 2014 a remote control system was installed. Each plasma discharge at AUG starts with the preparation trigger TS06 (about 3 min prior to the discharge start). With this trigger the piloting card DIO PXI-6040 (Fig.5.4) triggers both Tabor generators and they begin sweeping in a continuous way. Another trigger is provided for the acquisition card, which is able to write data in 2 modes: burst and standard. In the standard mode the card acquires n sweeps with a given time window in between (from 20 μs to 1 ms). In the burst mode the card records one or several "bursts" of data including the sweep and the dead time. The number of the acquired sweeps depends on the mode: until an upgrade of the card memory capacity 16,000 sweeps could be recorded in standard mode and 20,000 in burst mode. In 2015 the upgrade of the acquisition memory multiplied these numbers by 10.

The acquisition card and the generators are provided with an external clock and both generators are synchronised while sweeping. The triggers for the acquisition are set in

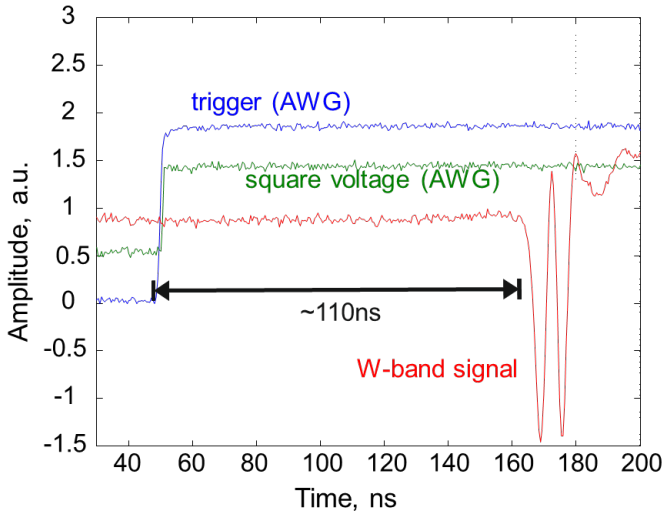

Figure 5.5: The time delay between the trigger of the voltage of the arbitrary waveform generator and the reflectometer signal from the plasma is of 110 ns

the software from a PC in the control room, connected by a pair of optical fibers to the piloting card. The triggers in the AUG time reference are then recorded with a precision of 0.1 μs (10 MHz).

During the first year the software stability was checked. The overheating of the piloting card and the generators caused many problems before the installation of 5 additional fans. The perturbation by the magnetic field during the discharges forced the removal of the ferrite isolators in the emitting and receiving lines.

The linearity and stability of the frequency ramp plays an important role in the data interpretation, that is why the voltage for the VCOs input was tested with high temporal resolution. The VCOs calibration showed that the beginning of the voltage ramp should be linear (Fig. 5.6a, green), but after the amplifiers a non linearity was observed during first 20 ns of the sweep (Fig. 5.6a, blue). As the frequency 50–75 GHz are swept in 1 μs, 20 ns correspond to $(75-50)$ GHz $\cdot$ 20 ns/1 μs $= 0.5$ GHz. This slow start of the sweep introduces an unwanted modulation of the beat frequency measured on a mirror and meant to be constant (Fig. 5.6b). The speed of the amplifiers limits the improving of the sweep time and the observed delay is corrected in the data analysis procedure by a shift of 0.5 GHz. This procedure reduces the trigger delay nonlinearity to a few nanoseconds which corresponds to a frequency uncertainty of a few tens of MHz and does not introduce significant errors in the density profile position [107].

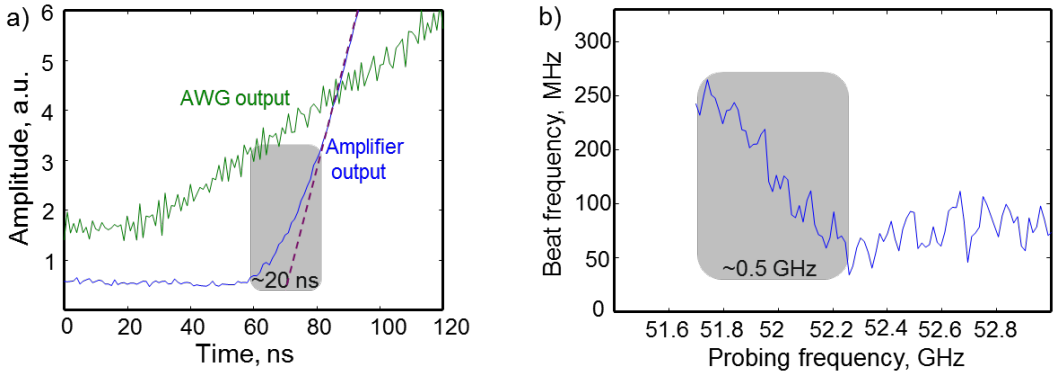

Figure 5.6: The non-linearity is introduced in the VCO input voltage by the amplifiers (a, blue) after the wave gennerator (a, green), this non-linearity causes a modulation of the beat frequency measured at the mirror of 20 ns (b)

The tests of the reflectometers performance followed the installation. First the signals from a reflection on a mirror installed in front of the antennas (30 cm distance) were analysed. Figure 5.7 demonstrates the beat frequency for V-(a) and W-band (b) calculated by a sliding FFT applied to 100 points of the signal phase Φ with a step of 40 points. The maximum (red in the colour code) corresponds to the beat frequency of 1–2 MHz which is proportional to the time of flight (5.2). The beat frequency in this example is not constant due to the erroneous switch of the generators calibration file (V to W).

Figure 5.8 depicts the amplitude of the signal filtered 4 MHz width around the beat frequency (in red) and the noise level (in black). The waveguide transmission line including the directional couplers as well as the vacuum window can introduce some spurious reflections. This results in the signal amplitude losses at certain frequencies both for the signal and the noise. The low-pass filter effect is visible at 104 GHz in the W-band (Fig 5.8, b). Nevertheless the signal-to-noise ratio is about 30 dB for the most part of the range 52–104 GHz. In addition the V- and W-bands have an overlap about 75–77 GHz frequencies allowing a smooth transition from one band to another during the profile reconstruction.

In order to measure the absolute position of the cutoff, one needs to choose a reference with at a position. In the case of the UFSR the reference is taken as the tungsten tile covering the inner vaccuum wall (at the HFS) of the tokamak. The beat frequency of the wave reflected from the backwall in vacuum is shown on Fig. 5.9. The second

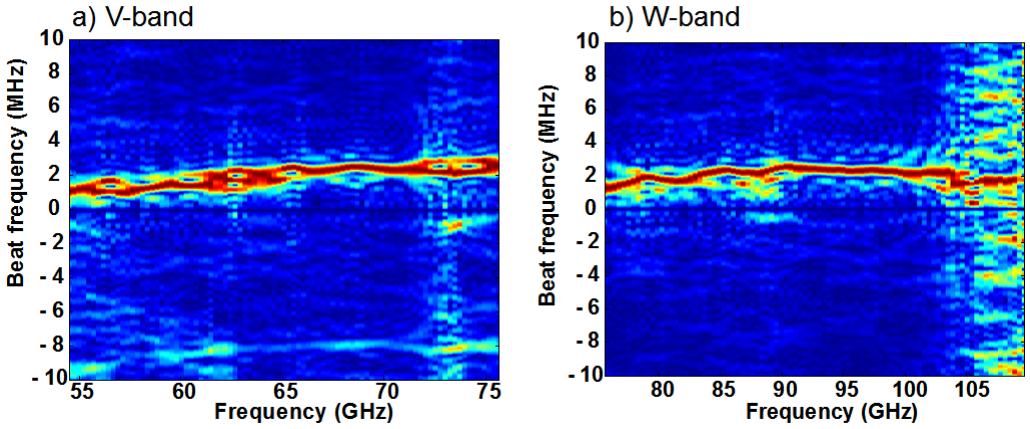

Figure 5.7: Beat frequency for the signal reflected from a mirror for (a) V- and (b) W- band

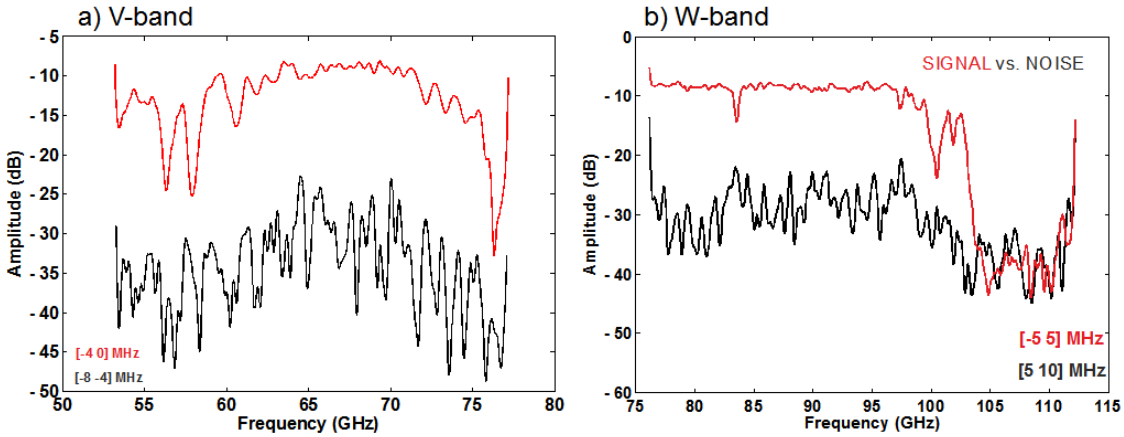

Figure 5.8: Amplitude of the signal reflected from a mirror for (a) V- and (b) W- band showing the losses at certain frequencies

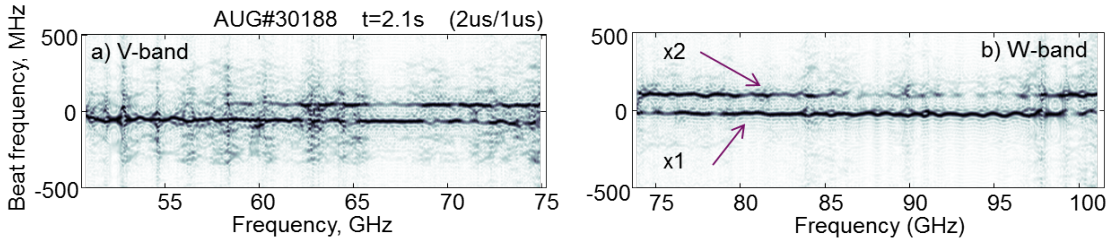

Figure 5.9: Beat frequency for the first and the second reflections from the HFS of the tokamak in vacuum for (a) V- and (b) W- band

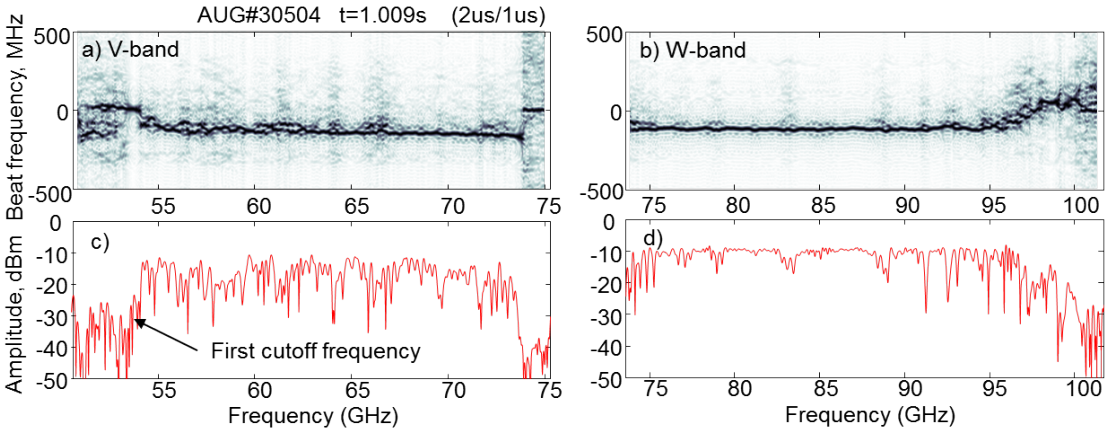

Figure 5.10: Beat frequency for a plasma discharge calculated by sliding FFT for (a) V-band, (b) W-band and the amplitude of the reflectometer signal for (c) V- and (d) W-band

reflection is observed at 100 MHz distance in the beat frequency, which corresponds to a distance about 2.4 m (double size of the tokamak vessel at the mid plane). The backwall reflection is observed in every plasma discharge in the first milliseconds or at the end of the discharge.

The beat frequency for a plasma discharge is presented on the Fig. 5.10a,b. The jump of the beat frequency at 53.5 GHz indicates the first measured cutoff position at the edge of the plasma. The jump happens when the frequency passes from the lower cutoff branch to the upper cutoff branch of X-mode polarisation and thus the probing wave is reflected in the edge, giving a stronger signal, rather after crossing the full plasma. Then the beat frequency increases while the time of flight is growing and the probing wave is reflected deeper inside the plasma. As the amplitude of the signal also has a rapid increase at the first cutoff, this can be used for the automatic profile initialisation.

After the end of the AUG 2014 campaign two main upgrades to the UFSR were made. First, a new acquisition card with extended memory capacity (up to 170,000 profiles per discharge in standard mode and 200,000 in burst mode) was installed in parallel with the original one allowing the use of standard and burst modes in the same plasma shot. Thus for every shot the discharge has been recorded in standard mode with a 0.5 ms time rate and in burst mode for the time windows needed from the physics studies prospective. Secondly, the sweep time was reduced to 1 μs in 2015. These new diagnostics capabilities have been exploited during the AUG 2014–2016

campaigns for many research topics. The precise density profile reconstruction was used for the study of boundary displacement due to ideal kink modes [108] as well as for gas puffing experiments. The frequency spectra were actively used in the investigations of LOC-SOC transitions [109] and turbulent trapped electron modes [110]. In parallel with a strong solicitation of UFSR data from the AUG team, the special experiments for the turbulence dynamics investigation during L-H transitions and ELMs were designed.

5.2 Data analysis methodes

The UFSR sweep time of 1 μs and dead time of 0.25 μs allow to reconstruct the frequency spectra up to 400 kHz and to study fast plasma turbulent events of the order of few microseconds with high time resolution using the density and the turbulence level profiles. The X-mode polarisation provides a large radial access from the very edge to the centre of plasma for central densities up to $5 \cdot 10^{19}$ m^{-3}. The standard acquisition mode gives the opportunity to follow slow events such as MHD modes in the kHz range of frequencies, while the burst mode allows to study the fast density profile dynamics. First studies of the electron density profile dynamics, fluctuations, radial wavenumber and frequency spectra of fluctuations were started in October 2014. In this section the main methods of reflectometry data analysis are discussed. In general, the different reflectometry techniques can be divided according to the measured quantities into four groups: density profile frequency-modulated continuous-wave (FM-CW), density fluctuation fixed frequency, Doppler and correlation reflectometers. The UFSR is able to work like FM-CW profile reflectometer and at the same time to provide turbulence and correlation measurements.

5.2.1 Density profile reconstruction

Launching a probing wave at a fixed frequency one can compare the reflected signal phase Φ with the emitted one. The difference of the phases is proportional to the integral of the refractive index on the wave line of sight from the reference position (plasma edge with electron density close to 0) until the cutoff layer in WKB approximation:

$$\Delta\Phi = \frac{2\omega_{wave}}{c} \int_{R_{ref}}^{R_{co}} N[n_e(R), B(R), \omega] \mathrm{d}R - \frac{\pi}{2} \tag{5.3}$$

Making a frequency sweep, a reflectometer can reconstruct a density profile. The position R_{co} can be found by Abel inversion [111] for O-mode, as the refractive index depends only on the density and the probing wave frequency (2.18). For X-mode the dependence on the magnetic field does not allow an analytical expression for the position of the cutoff (2.20). Therefore numerical methods are used to find the positions of cutoff layers step by step, starting from the edge of the plasma. For O-mode to scan the whole plasma a wide frequency range is needed, in addition the SOL plasma density being too low is not measured with GHz frequencies. The X-mode offers the advantage that fewer frequency bands than in the O-mode are needed, but it has the disadvantage that the toroidal magnetic field must be known with high accuracy to evaluate the density profile. The X-mode allows a better localisation of the cutoff layer due to the shorter wavelength of the probing signal (2.23).

In this work the Bottollier-Curtet algorithm is used as the integral (5.3) inversion method. The full description of the algorithm is given in [94]. $\Delta\Phi$ in (5.3) is measured directly, the frequency of the probing wave is known and $B(r)$ can be obtained from the magnetic equilibrium reconstruction EQH with a time resolution of 1 ms. The unknown quantities are the cutoff layer position R_{co} and the electron density $n_e(R)$. From 1000 points of the raw signal usually 100 are used for a faster reconstruction. Using (5.3), the difference of the phases measured for two close probing frequencies F_{i+1} and F_i is approximately the area below the $N(F_{i+1}, R^i_{co})$ function:

$$\frac{\Phi_{i+1}}{k_0(F_{i+1})} - \frac{\Phi_i}{k_0(F_i)} = \frac{4}{3}(R^{i+1}_{co} - R^i_{co})N(F_{i+1}, R^i_{co}). \tag{5.4}$$

Note that the factor 4/3 comes from the fact that the refractive index behaves as a square root function of the distance in plasma core, which is no longer true at the edge, so in the edge the best factor is 1 as it is described in new developing methods of profile reconstruction [112].

When the density profile is calculated until R^i_{co}, the term $N(F_{i+1}, R^i_{co})$ also can be found. Then the next cutoff position R^{i+1}_{co} can be extracted from (5.4). The density is found from the expression for the X-mode cutoff frequency (2.20):

$$F_p^2(R^{i+1}_{co}) = \left(\frac{\omega_{pe}}{2\pi}\right)^2 = \frac{n_e e^2}{\pi m_e} = F^2_{i+1} - F_{i+1}\frac{\Omega_{ce}(R^{i+1}_{co})}{2\pi} \tag{5.5}$$

The Bottolier-Curtet method is applied to the signal phase, filtered around the beat frequency, $\langle\Phi\rangle$. The initial amplitude jump is used for the definition of the first cutoff

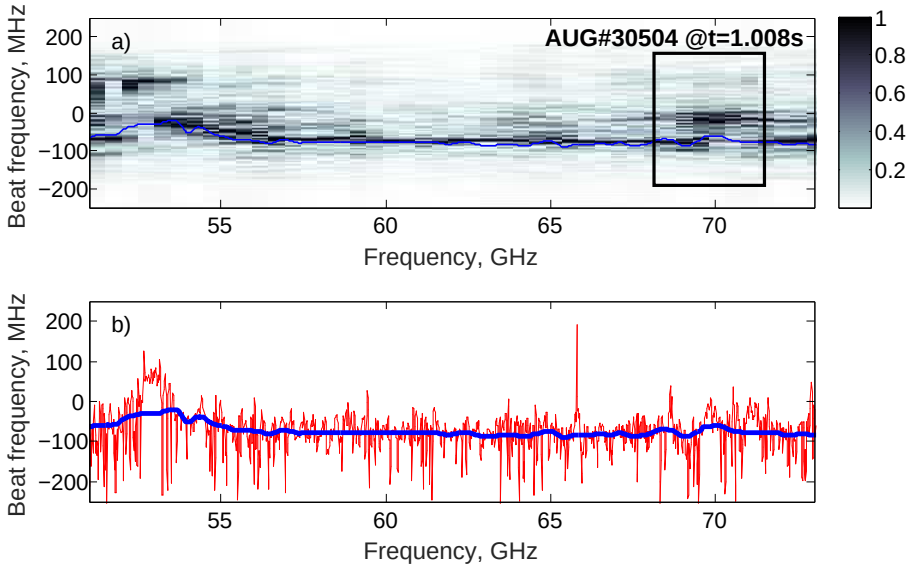

Figure 5.11: Beat frequency for a plasma discharge, calculated by a sliding FFT (a, gray scale) and by deriving the signal phase (b, red), the region with multi-reflections is indicated with a rectangle, the filtered beat frequency (b, blue) is used for the profile reconstruction.

frequency F_1. The electron density associated to F_1 is assumed to be equal to zero, then from $F_1 = \frac{\Omega_{ce}(R^1_{co})}{2\pi}$ the first cutoff position R^1_{co} is deduced.

One of the most important steps in profile reconstruction is the phase filtering. The Bottollier-Curtet method applied to the raw data of the strongly fluctuating phase can be unstable. Only a smooth and monotonic phase should be used. In order to extract a mean phase $\langle\Phi\rangle$ several procedures are undertaken. First, the backwall reference phase is removed from the measured complex signal. Then multiple reflections must be filtered out. The distance between the antennas and the plasma edge is about 20 cm in AUG. This means that if the plasma has a strong density gradient in the edge, the probing wave can be reflected twice as it happens for the backwall (Fig. 5.9), unfortunately in this case the beat frequency separation would be around 15 MHz and a narrow filtering is required. To find the beat frequency on one hand, one can derive the phase at each measurement point (1000 points), which is a fast and efficient method. On the other hand, by applying a sliding FFT and finding of the spectral maximum for each time window, the noise in the beat frequency detection can be reduced. Figure 5.11 illustrates the signal processing: the beat frequency F_b^{FFT} found with the sliding FFT (100 signal

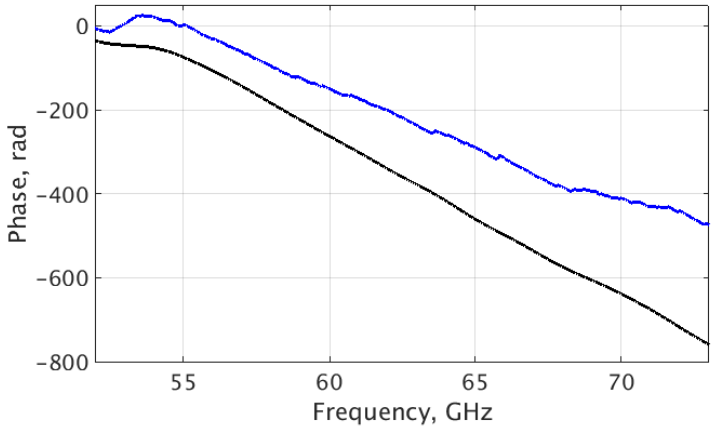

Figure 5.12: The raw signal phase (blue) containing several jumps from the unwraping ambiguity compared with the filtered phase (black) for #30504, $t = 1.008$ s

points for each FFT, 40 points step) is colour-coded (Fig. 5.11a) while the derivative of the phase F_b^{dt} is shown in Fig. 5.11b in red. For the filtering, F_b^{dt} is smoothed over 50 points and integrated in order to obtain the corresponding phase. This phase is removed from the complex signal and the obtained signal S_1 is twice filtered around zero frequency with filters [-100, 100] MHz and [-10, 20] MHz. The first filtering is needed to find the beat frequency without parasitic reflections around which one can then apply a narrower filter. The resulting beat frequency is shown in Fig. 5.11 with the blue line. The multi-reflections around 70 GHz are significantly reduced. Every multi-reflection or a strong fluctuation produces a jump of the phase that can be seen on the raw signal phase. As a result of this the phase increases faster than in a non-perturbed case and can introduce a profile deformation. Figure 5.12 depicts the difference between the raw phase and the filtered phase, that corresponds better to the real plasma density profile. From this beat frequency the phase is reconstructed. In addition using 2–10 consecutive sweeps, the average beat frequency can be taken to avoid strong fluctuations of density.

An example of a density profile is shown in Fig. 5.13. The multi-reflection creates a deformation of the profile around 2.10–2.13 m in the steep gradient region. An additional filtering is needed for this region, the result of the local filtering in the range [-10, 1] MHz around the beat frequency is shown in red and illustrates the improvement of the profile quality with an appropriate signal treatment. In [104] the filtering effect

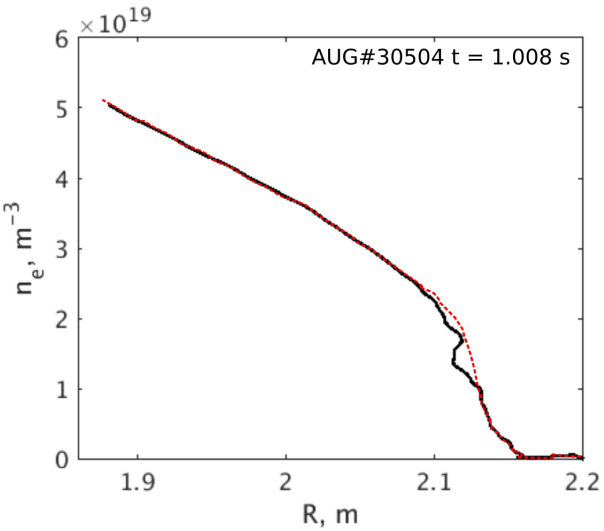

Figure 5.13: Electron density profile with a broad filtering (black solid) compared to the profile with a narrowly filtered phase (red)

on the density fluctuation measurements is described and the conclusion is that for a filtering width above 4 MHz (for a 20 μs sweep) the turbulence level estimation is not affected, which is important for the spectra reconstruction methods (Section 5.2.3).

5.2.2 Step to the ASDEX database

As the profile reconstruction procedure has been automatised, the resulting data are now written in the AUG database which has a standard structure of the shot file. The time of the sweep is transferred as the timebase, the absolute radial position **R** and **rhop** form two area-bases which are connected by the chosen equillibrium reconstruction. The "signals" chosen to be stored are: electron density **ne**, cutoff frequencies **Freq** and group delay **tau**. The signals and the area-bases have 100 points for each sweep. Some important parameters like the magnetic field value on the magnetic axes or the type of equilibrium are also included in the shotfile. More than 1000 shots have been analysed and written in the database. Thus the UFSR profiles can be easily compared to other diagnostics.

5.2.3 Wavenumber power spectra and turbulence level

The phase fluctuations $\delta\Phi$, being induced by density fluctuations, give information about the turbulence level, frequency and wavenumber turbulence spectra:

$$\Phi = \langle\Phi\rangle + \delta\Phi, \quad \delta\Phi = f(\delta n). \tag{5.6}$$

In the case of low-amplitude turbulence and O-mode polarization, the phase fluctuation wavenumber spectrum is directly proportional to the density fluctuation spectrum [32]. We have extended the concept to the X-mode and introduced a k_r-dependent transfer function, which needs to be found for each radial position and time using a 1D full-wave propagation simulation [113]. Experimental density, magnetic field profiles and predicted fluctuation wavenumber spectra are used as input and the simulation produces the signal phase fluctuation spectra as output. The ratio of input and output spectra gives the transfer function $T(k, R, t)$:

$$T(k_r, R, t) = \frac{S_{\delta n}(k_r, R, t)}{S_{\delta\Phi}(k_r, R, t)}. \tag{5.7}$$

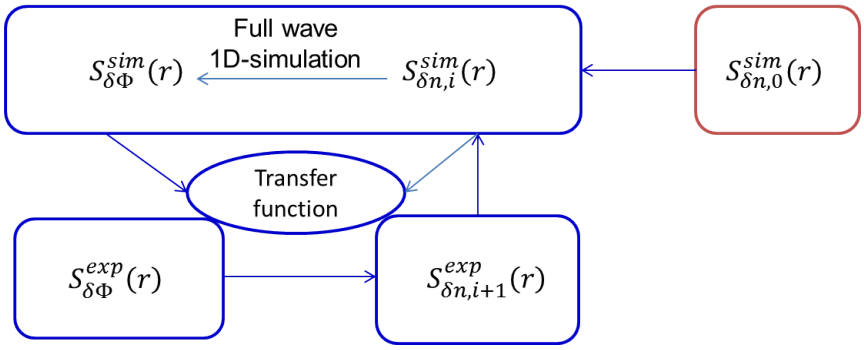

Figure 5.14: The principle of the closed-loop minimising method for the wavenumber spectra $S_{\delta n}$ reconstruction from the phase spectra $S_{\delta\Phi}$

A closed-loop minimizing method [114] is applied to reduce the difference between the output and measured phase spectra. If they are close enough, the input at this iteration is taken as the real density fluctuations spectra, otherwise the current transfer function is applied to the experimental phase spectra and the result is used as input for the next iteration (Fig. 5.14). The difference between the output and the measurements is taken as an error bar estimation and the looping terminates when the error becomes

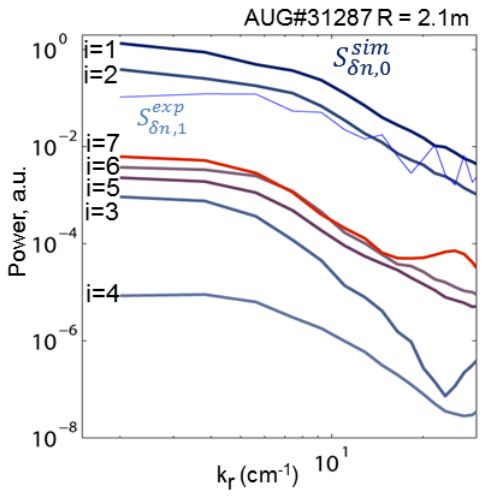

Figure 5.15: First iterations of the closed-loop method for the shot #31287, t = 2.13 s: the iterations 5 and 6 have the closest shape and amplitude and are used as the real plasma spectrum estimation

sufficiently small. In Fig. 5.15 the first 7 iterations are presented for a low density plasma discharge in the L-mode. The phase wavenumber spectra are calculated at the edge where the level of density fluctuation is about 10 %. In light blue the output of the first iteration is shown. For the second step it is smoothed and reshaped to the dark blue spectrum $i = 2$. The aim of the iterations is then to find the two closest consecutive spectra. Note that in this particular case already the first two iterations are close enough, that means that the initial spectrum shape is chosen reasonably. In this shot the iterations 5 and 6 have the closest shape and amplitude, therefore the input $S^{sim}_{\delta n,5}$ is the best candidate for the real plasma spectrum and the error bar can be estimated as the difference $S^{sim}_{\delta n,6} - S^{sim}_{\delta n,5}$.

Due to the Bragg condition (2.22) it is possible to get information about density fluctuations with wavenumbers k_f twice that of the probing wave ($k_f = 2k_r$), here the probing wavenumber varies in the cutoff region from 10 to 0 cm^{-1}. The lower k_r limit depends on the sample window size used in the reconstruction, so finally this gives a 2 cm^{-1} $< k_r <$ 20 cm^{-1} range for the detected density fluctuations. This corresponds to the turbulent scales of $\rho_s < L_r < 10\rho_s$ for typical AUG conditions. By integrating the wavenumber spectra over k_r, a radial profile of the density fluctuations level $\delta n/n$

can be reconstructed:

$$\left(\frac{\delta n}{n}\right)^2 = \frac{1}{n_e^2(k_{max} - k_{min})} \int_{k_{min}}^{k_{max}} S_{\delta n}(k_r) dk_r. \tag{5.8}$$

It appears that the weak convergency of the closed-loop method can produce big error bars. To reduce the uncertainties, the method should be further improved by including some constraining hypotheses on the transfer function (5.7). During the iterations the k_r spectrum sometimes tends to form a maximum around 10–15 cm^{-1} and create a positive slope, in order to prevent the appearance of this artifact, input spectra are modified by smoothing and correcting the slope to negative values. If the absolute spectral power starts to diverge to infinity and the corresponding turbulence level exceeds 100 %, the input spectra are divided by a constant. Other restricting hypotheses could be made via 2D full-wave simulations and the corresponding work is ongoing. The optimal solution would be to find an analytical expression for the transfer function depending only on plasma parameters. Up to now the limiting conditions on the spectral power and on the slope of k_r spectrum are applied and, in order to reduce the calculation time, the same initial slopes are applied for each burst of measurements.

5.2.4 Frequency power spectra

The spectral analysis of the reflectometer signals is a powerful tool for the investigation of MHD and turbulent oscillations in plasma. For this, the complex Fourier transform is used, which in the case of a single infinite and perfectly sinusoidal signal is non-zero only at the frequency of the sine function. For a perfectly periodic but not sinusoidal signal the Fourier transform is a set of discrete values at the fundamental signal frequency f and at multiples of it (harmonics). A discrete Fourier transform is performed because of the data discretisation and it is often used with the Fast Fourier transform (FFT) algorithm. The discrete character of the signal causes a limit to the detectable frequencies, called Nyquist frequency, $f_N = 0.5 f_s$, where f_s is the sampling frequency. When the signal contains a frequency $f > f_N$, a mirrored frequency $|f - nf_N|$ will appear in the frequency spectrum with n satisfying condition $|f - nf_N| < f_N$. In our case there is no possibility to filter out these higher frequencies. Therefore it is important to sweep faster in order to reach $0.5 f_s$ higher than the width of the turbulence spectrum, generally a few hundred kHz.

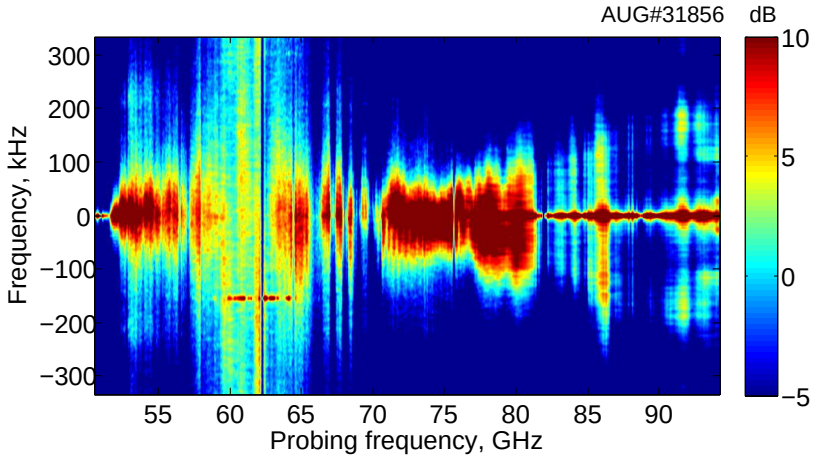

Figure 5.16: Frequency power spectra for all probing frequencies 50–100 GHz, #31856, $t = 0.500$–0.510 s

The frequency spectra are obtained by taking the FFT of the complex signal $S = A(t)e^{i\Phi(t)}$ for each probing frequency. For a fixed radial position, this permits frequency spectra reconstruction up to a half of the sampling frequency $\frac{1}{2}f_s = \frac{1}{2}(t_{sweep} + t_{dead})^{-1}$ equal to 166 kHz for the 2014 campaign and 400 kHz since 2016. Usually at least $N = 256$ time points are needed to reconstruct a spectrum, which excludes the frequencies below $f_{min} = 1/N \cdot (t_{sweep} + t_{dead})^{-1}$ or 3.125 kHz. The time window length has to be adjusted according to the phenomena time scale. There is always a competition between the time resolution and the reduction of noise in the spectra which can be reduced by ensemble averaging of several spectra.

Figure 5.16 depicts an example of spectra for 10 ms of discharge #31856 for the probing frequencies of both V- and W-band. The power spectrum is averaged over 40 power spectra from time windows of 200 sweeps each. This procedure allows to obtain a smoothed spectrum. A parasitic oscillation frequency at −160 kHz is observed for probing frequencies of 60–65 GHz, showing the typical asymmetric behaviour (absent in the positive frequencies). This behaviour might be due to the sawtooth-like shape of the parasitic signal.

Applying FFT to successive time windows, the temporal development of the power spectrum can be obtained and represented as a spectrogram. Spectrograms provide a good overview of the modes dynamics in frequency and amplitude. If the density profile

is reconstructed, the probing frequency can be expressed as a monotonic function of the radial position $F(R)$. Hence the complex signal can be interpolated to the radial points of the averaged density profile.

5.2.5 Correlation length

The radial correlation length L_r is an effective way to describe the spatial scale of the turbulence. Calculated for the reflectometer signal, it carries the information about the characteristic radial wavenumber $\langle k_r \rangle = 2\pi / L_r$. The main question for the correlation analysis is which quantities should be correlated. As the reconstruction of the density profiles requires a narrow filtering and smoothing, the details of the fluctuations can be lost, therefore the raw data are preferred. It is still unknown which part of the signal: the amplitude, the phase or the entire complex signal, one should take to extract the correlation length, that corresponds to the mean structure size.

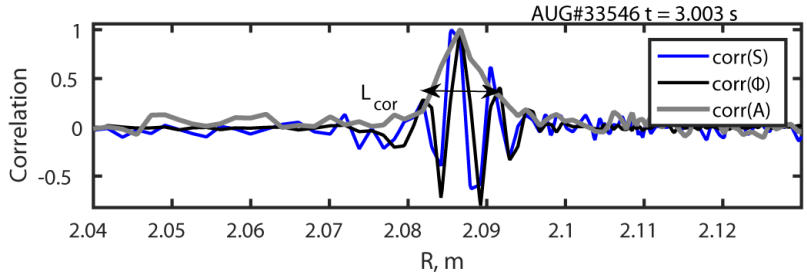

Figure 5.17: Radial autocorrelation function for the complex signal S (blue), the signal phase (black) and the signal amplitude (grey)

The correlation function of two signals $S_1(x)$ and $S_2(x)$ is defined as:

$$\mathrm{Corr}_{S_1,S_2}(\Delta x) = = \frac{\sum_{i=1}^{n} \tilde{S}_1(x_0, y_i)\tilde{S}_2(x_0 + \Delta x, y_i)}{\sqrt{\sum_{i=1}^{n} \tilde{S}_1(x_0, y_i)^2 \sum_{i=1}^{n} \tilde{S}_2(x_0 + \Delta x, y_i)^2}}, \tag{5.9}$$

where $\tilde{S}_1(x_0, y_i) = S_1(x_0, y_i) - \langle S_1(x_0, y_i) \rangle$ and Δx covers a range $[x_1, x_n]$. The reflectometer signal is a function of the probing frequency, so the correlation functions are calculated for the steps ΔF within $[F_{min}, F_{max}]$ and then interpolated to the absolute radial position. If $S_1 = S_2$, the function (5.9) is called the autocorrelation function and should have a peak of 1 at $\Delta x = 0$. An example of the autocorrelation function is

shown on the Fig. 5.17, where x_0 is the frequency $F_0 = 83$ GHz corresponding to the absolute position $R = 2.087$ m. It is calculated for the complex signal S, its phase Φ and amplitude A. The first two autocorrelation functions $\mathrm{Corr}_{S,S}$ and $\mathrm{Corr}_{\Phi,\Phi}$ have a modulation with the period of 1 ns, as the W-band is swept with $dF/dt = 30$ GHz$/1\mu$s, this modulation corresponds to the beat frequency (5.2) of 30 MHz, which is included in the phase, but not in the amplitude. For this reason the autocorrelation function for the amplitude $\mathrm{Corr}_{A,A}$ does not have any modulation and coincides with the envelope of $\mathrm{Corr}_{S,S}$ and $\mathrm{Corr}_{\Phi,\Phi}$. The correlation length is defined as the width at 1/e amplitude, in this case $L_r = 6.5$ mm. In the following the correlation functions will be always calculated for the signal amplitude.

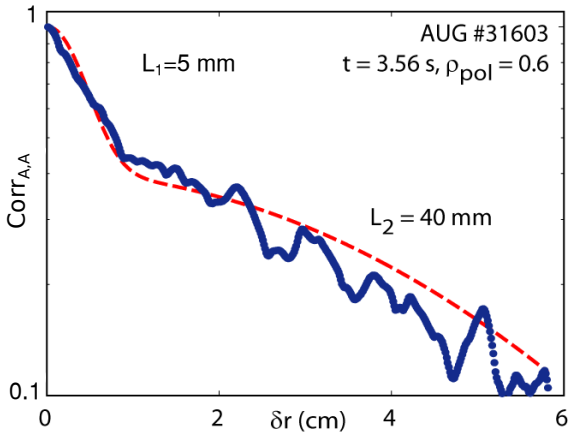

Figure 5.18: Autocorrelation function of the reflectometer signal amplitude with two slopes

The shape of the correlation function is an important issue. All the autocorrelation functions obtained from UFSR raw data have two slopes and can be approximated with two Gaussian functions. Despite this shape, the correlation length for simplicity is defined as the logarithmic decay width. Another example of the autocorrelation function is shown on the Fig. 5.18. Two slopes correspond to structures of 5 mm and 40 mm. In principle the large scale may be explained by so called avalanches or streamers, i.e. poloidally localised turbulent structures which propagate radially with an extremely high velocity [115]. But it is also possible to explain the presence of two slopes by 2D scattering effects on the reflected waves, as discussed in [116]. This topic deserves further investigation.

6 Experimental results on the L-H transition

The plasma confinement is limited by the radial energy and particle transport, in which turbulence plays an important role, as described in Chapter 3. Hence for fusion plasmas regions of reduced turbulence, such as transport barriers, are of special importance. The most pronounced transport barrier develops at the plasma edge at the transition from the low (L-) to the high confinement (H-) mode [8]. As shown in Chapter 3 the plasma edge turbulence is stabilized by increased radial electric field gradient: the $\mathbf{E_r} \times \mathbf{B}$ flow shear reduces turbulence and decreases the radial size of turbulent structures [13] during the transition to H-mode. A transport barrier forms in the edge where the density and the temperature together with their gradients increase. In the following sections first the characteristics of L- and H-mode are described and then the focus shifts to the limit-cycle oscillations and the intermediate phase between a clear L-mode and an established H-mode.

6.1 Dynamics and mechanisms of the L–H transition

The results presented here have been obtained by analysing a series of AUG discharges with both L- and H-mode phases. The D or He plasma was heated using electron cyclotron resonance heating (ECRH) at 140 GHz, which corresponds to core heating at a magnetic field of 2.40–2.56 T used in these discharges. The power step amplitude has been chosen for each density to be slightly above the threshold for an L-H transition (Fig. 6.1a), using the power threshold scaling from [67].

Different values of the central plasma densities from 3 to $7 \cdot 10^{19}$ m^{-3} have been chosen in order to check the universality of observed phenomena. Figure 6.1 shows the

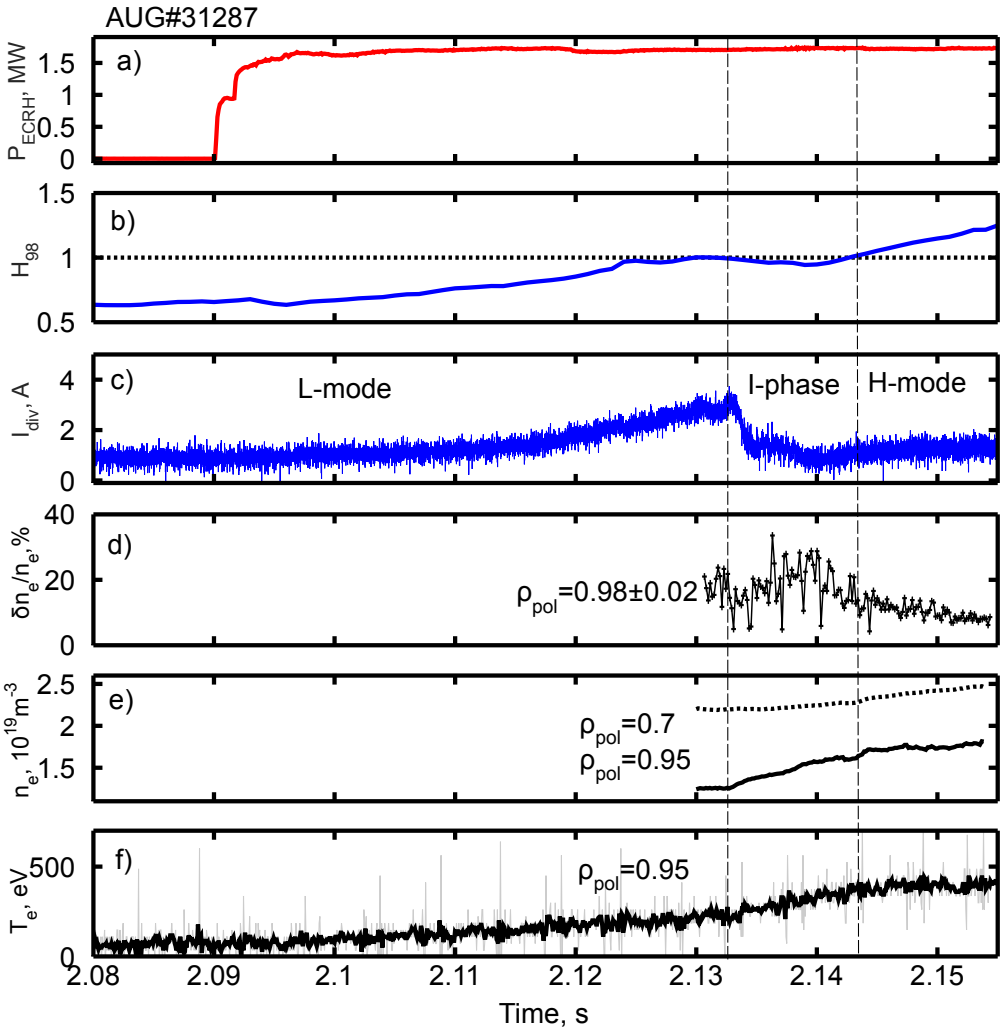

Figure 6.1: Low-density L-H transition: (a) electron-cyclotron heating power, (b) H-factor, (c) divertor current, (d) density fluctuation level around $\rho_{pol} = 0.98$ calculated every 160 μs over 10 sweeps, (e) pedestal top (solid) and core (points) density from 10 000 UFSR sweeps of 2 μs (1 μs dead time)

time trace for the H-factor $H_{98} = \tau_E / \tau_{\mathrm{IPB98(y,2)}}$ (b), where τ_E is the energy confinement time and $\tau_{IPB98(y,2)}$ is the scaling based on the set of ELMy H-mode data from different tokamaks [117], indicating the confinement improvement in H-mode for the shot #31287. The L-H transition can be conveniently detected in the divertor current indicating the particles confinement change (Fig. 6.1c) and in the pedestal top density (at a normalised radius of $\rho_{pol} = 0.95$) that has a rapid grow (Fig. 6.1e, solid line) while the gas puff is kept constant. The core density builds up slower (Fig. 6.1e, dashed line), so the edge density gradient is significantly increased as well as the edge temperature gradient. The evolution of the electron density profile can be seen in Fig. 6.2: the profile builds up inside $\rho_{pol} = 0.99$ from shallow in the L-mode (2.126–2.132 s) to steep in the H-mode (after 2.142 s). The profiles presented in Fig. 6.2 are averaged over 1 ms, which leads to a somewhat shallower shape in the pedestal region.

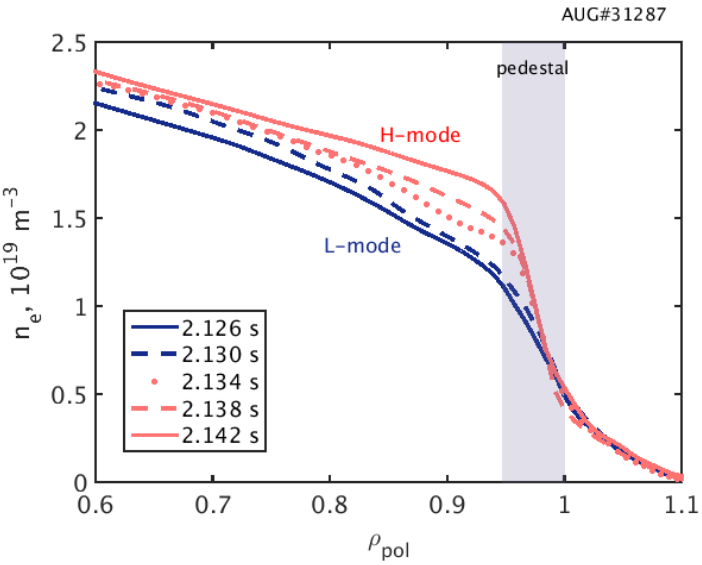

Figure 6.2: Density profile evolution during an L-H transition, L-mode at 2.126–2.130 s, I-phase at 2.134–2.138 s, H-mode after 2.142 s, from the UFSR

Every L-H transition on AUG passes through an I-phase, which can be maintained during the whole discharge if the power threshold of the transition is not reached. Although the plasma density and temperature oscillations happen during the whole I-phase, the strong density gradient appears after the first milliseconds of it. At the same time the turbulence level strongly oscillates (Fig. 6.1d) from 20–30 % to small

values of about 10 % that indicate the building of the transport barrier in the very edge of the plasma, characteristic for the H-mode. The turbulence level is calculated for the radial windows of $\Delta\rho_{pol} = 0.04$ around $\rho_{pol} = 0.98$ every 160 μs. This time resolution (chosen for the sake of minimisation of the analysis time) does not allow to distinguish the I-phase oscillation, typically a few kHz, however, the fluctuation oscillation is visible directly in the raw UFSR signal. The phase fluctuation modulation with the I-phase frequency is observed in the pedestal region $0.95 < \rho_{pol} < 1$, where the strong fluctuation bursts (in red) follow the turbulence suppression (green-blue) (see Fig. 6.3).

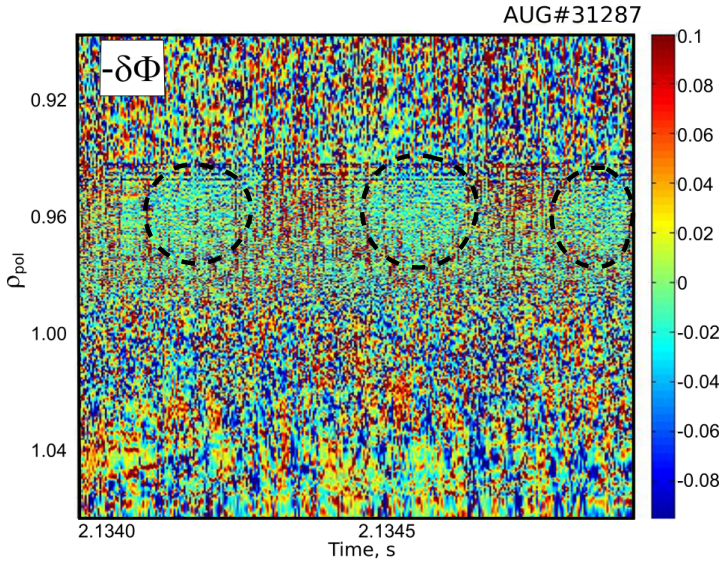

Figure 6.3: Fluctuation of the reflectometer signal phase during the I-phase, the reduction of the phase fluctuation is surrounded by black dashed lines

The L-H transition occurs 20–60 ms after the additional heating start as it is seen around 2.133 s in the drop of the outer divertor current (Fig. 6.1c). The average turbulence level in the edge decreases from 20 % in L-mode to 10 % in H-mode (Fig. 6.1d). As the UFSR has limited acquisition memory, in the high sweeping rate mode the system could acquire only 30 ms during the AUG campaign 2014 and 250 ms in 2015. For this reason the trigger for measurements has been set a few milliseconds prior to the expected L-H transition, so the density fluctuation level (Fig. 6.1d) and the precise density evolution (Fig. 6.1e) are typically available only for a part of the

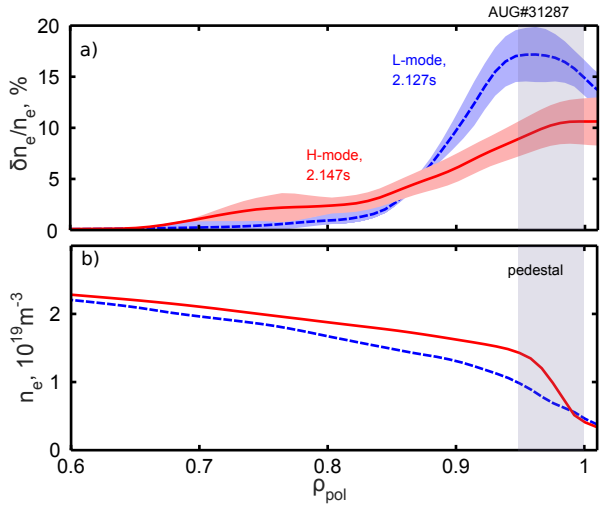

Figure 6.4: (a) Density fluctuation radial profile and (b) density profile in L-mode (blue dashed) and in early H-mode (red solid)

discharge. Immediately after the reduction of particle transport to the outer divertor, high-frequency modes appear in the frequency spectra of density fluctuations. The modes are characterised by narrow frequency bands and high coherence within a broad radial extent in the plasma edge. The description of the edge coherent modes is given in Chapter 7.

It is clear that for the analysis of the L-H transition dynamics, the stable L-mode (until 2.132 s) and the established H-mode (after 2.145 s) should be separated from the short I-phase of 15 ms. If there is a trigger for the transition, it should be searched between the start of the heating pulse and the drop of the divertor current. The comparison of L- and H-mode density fluctuation is discussed in the next section, whereas a zoom on the I-phase is presented in section 6.3.

6.2 Comparison of L- and H-mode turbulence characteristics

In this section an early H-mode (16 ms after the divertor current drop) following the I-phase is compared to an L-mode plasma. To describe the turbulent transport, the radial profiles of the turbulence level have been extracted from the UFSR data. Applying

the closed-loop method and 1D-wave propagation simulation, the radial wavenumber spectra for each radial position have been found. Then, by an integration over small radial wavenumbers 1 $\text{cm}^{-1} < k_f < 10\ \text{cm}^{-1}$ the absolute turbulence level profiles have been reconstructed (Fig. 6.4). The spectral power drops from the plasma edge to the core (Fig. 6.5) and is strongly reduced in the edge after the transition to the H-mode. Two spectral slopes are visible in L-mode and H-mode spectra at $\rho_{pol} = 0.95$. The change in the spectral slopes can be distinguished within the error bars. The wavenumber spectra were calculated for radial windows of 3 cm each, which leads to the smoothing of the turbulence level radial profile. The flattening of the spectrum in the L-mode might happen because of the change of turbulence regime as well as because of the saturation effect for the reflectometer phase response in the case of high amplitude density fluctuation [116]. Note also that the values of the spectral slopes might not be accurate due to non-linear effects in the wave turbulence interraction and due to the saturation in X-mode for high level turbulence [118–120]. The nonlinearity parameter [118] is estimated as γ =100–500, although the standard deviation of the phase fluctuation is less than 1. This indicates that the turbulence measurements were obtained in a non-linear regime. Nevertheless, the absolute turbulence level obtained after integration is not affected by the saturation of the wavenumber spectra [104]. The decrease in turbulence level during the L-H transition is consistent with the predicted suppression of large scale turbulent structures ($0.1 < k_r \rho_s < 1$) in the pedestal region, from the separatrix, $\rho_{pol} = 1$, to the top of the density pedestal.

6.3 I-phase and limit-cycle oscillations

Between the L- and the H-mode an intermediate phase, called I-phase [11], occurs, where the turbulence level, background and turbulent flows oscillate in the kilohertz range and the E_r well deepens towards H-mode values. The I-phase has been observed in different devices [11, 19, 20, 121–124]. Experimentally the I-phase can be characterised by the oscillations of the $\mathbf{E} \times \mathbf{B}$ flow and the turbulence level. Moreover similar oscillations have been observed in the plasma density, temperature, their gradients and magnetic fluctuations from Mirnov coils. In ASDEX Upgrade (AUG) the number of periods preceding an established H-mode varies with the heating power and density, but at least a few oscillations are always present in favorable magnetic configuration (ion ∇B drift in X-point direction) [80].

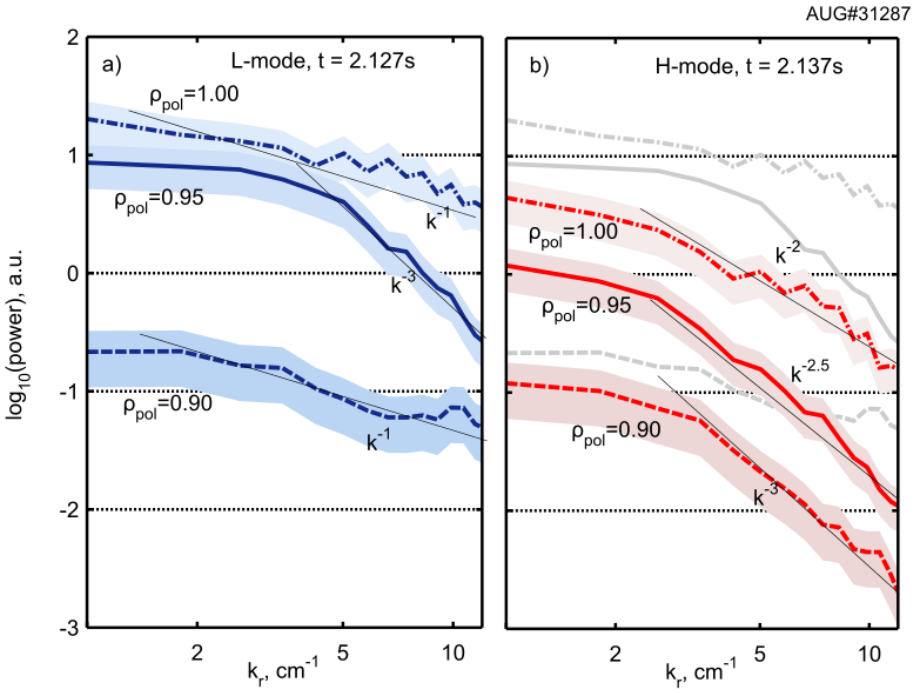

Figure 6.5: Density fluctuation k_r spectra evolution in L-(a) and H-mode (b) at $\rho_{pol} = 1.00$ (dash dot), $\rho_{pol} = 0.95$ (solid), $\rho_{pol} = 0.90$ and 3 cm window

6.3.1 Radial electric field as main player during I-phase

The origin of the strong radial electric field appearing in the I-phase and in the H-mode is still discussed. In principle it can have contributions from the background E_r, as described by neoclassical theory, or from the turbulence driven zonal flows. Neglecting various forces which might have influence on E_r (such as ion orbit loss [125]), it is often supposed that the radial electric field can be written as a sum of two contributions:

$$E_r = E_r^{neo} + E_r^{ZF} = v_{E\times B}B, \tag{6.1}$$

where

$$E_r^{neo} = \frac{\nabla p_i}{Zen_i} - \alpha\frac{\nabla T_i}{e} + \frac{B}{B_\phi}B_\theta\langle V_{i\|}\rangle \tag{6.2}$$

is the neoclassical or the mean background electric field, E_r^{ZF} is the radial electric field created by the zonal flows and GAMs through the Reynolds stress, T_i, n_i and p_i are the ion temperature, density and pressure, B is the magnetic field strength and

α is a coefficient depending on collisionality [14]. The I-phase has been described as an interplay between the turbulence and turbulent zonal flows that creates limit-cycle oscillations (LCO) [58] or, alternatively, as a relaxation of the mean radial electric field after a bifurcation of the poloidal flow to H-mode value [126]. Some theoretical models include both the zonal flow and the mean shear flow [127] and maintain the primordial role of the zonal flow in the L-H transition. From the theoretical point of view, LCOs with different causality are possible, creating on the phase plane $\delta n_e/n_e$-E_r cycles in clockwise or in counter-clockwise directions. Historically first it has been observed on AUG that there is a phase shift during I-phases in low-density plasmas [11]. In this case no modulation in the electron pressure gradient has been detected, as a consequence it has been supposed that the feeding mechanism of the I-phase is the predator-prey interplay between the turbulence and the zonal flows. On the contrary from EAST tokamak experiments it has been reported that there is no phase shift [124].

In general it is challenging to measure E_r, density, temperature and turbulence dynamics on a fast time scale. Therefore the mechanisms of the I-phase are difficult to determine from experiments. The experimental evidence of the presence of a zonal flow generally consists in the difference between the neoclassical and the total $\mathbf{E} \times \mathbf{B}$ flow. This evidence has been reported at several devices [11, 127]. However, by means of CXRS measurements of the perpendicular velocity and of the ion pressure in AUG, it was found recently that in some I-phases the background E_r^{neo} dominates and oscillates in phase with the $\mathbf{E} \times \mathbf{B}$ velocity and the turbulence level [128] within the diagnostic time resolution of 100 μs. From this it has been postulated that zonal flows do not play a significant role in the L-H transition. At the same time on AUG it was shown that the signatures of the LCO during the I-phase resembles to a type III ELM relaxation [129]. In [123] it is also shown that in the JFT-2M tokamak the LCO can occur without zonal flows.

Thus far, I-phases with and without zonal flow contribution have been reported and LCO phase space trajectories in both clockwise and counter-clockwise directions have been observed at different devices. The aim of the present study is to provide a better understanding of the turbulence and $\mathbf{E} \times \mathbf{B}$ velocity shear dynamics during the L-H transition. The UFSR is able to measure the electron density radial profile together with the turbulence level with a time resolution of the order of microseconds. The simultaneous measurement allows to localise and correlate density and density gradient perturbations at different radial positions. The neoclassical radial electric field (6.2)

can be approximated by the normalised ion pressure gradient if the toroidal velocity is small [130]. In first approximation the normalised ion pressure can be set equal to the normalised electron pressure

$$E_{r0} = \nabla p_e / Zen_e \tag{6.3}$$

for high collisionality, when $T_i = T_e$ can be assumed. However, this assumption is maybe a little too strong for the edge region where the equipartition time may be as large as a few milliseconds. Nevertheless, the measurements of the electron dynamics have the advantage of a better time resolution than one could achieve using the correct ion temperature and density. Combining the UFSR density measurements with 1 μs temporal resolution with the ECE electron temperature data averaged over 100 μs, it is possible to follow the dynamics of the contribution of the density gradient to the electron pressure gradient. In addition, Doppler backscattering system with several fixed frequency channels provides fast measurements of the $\mathbf{E_r} \times \mathbf{B}$ velocity. The difference or the agreement between the normalised pressure gradient E_{r0} and E_r independently measured by Doppler reflectometer can give some clues to the physics of the I-phase.

6.3.2 Density and electric field dynamics during I-phase

During this study, I-phases for various plasma conditions were documented and the contribution of the background flow to the total $\mathbf{E} \times \mathbf{B}$ flow has been analysed. During the first milliseconds after the divertor current drop, the I-phase has been observed for each discharge from the experimental series. Figure 6.6 shows an example of the I-phase starting at 3.117 s in a He discharge. The upper plot demonstrates the evolution of the normalised electron pressure gradient E_{r0} ((6.3) with $Z = 2$), used as an estimate of the neoclassical radial electric field, at different radial positions. The pressure has been calculated from UFSR density data with 1 μs resolution averaged over 10 μs and from the ECE temperature measurements averaged over 100 μs. A correction of the shine-through effect has been included in the ECE temperature profiles reconstruction. The average edge electron density starts to grow continiously from the beginning of the I-phase until the first type-I ELM at 3.245 s in the H-mode (Fig. 6.6b). Strong oscillations of the density and of E_{r0} are visible on both plots. The modulation of E_{r0} is localised in the pedestal region, $0.94 < \rho_{pol} < 1$. During the I-phase the average neoclassical electric field continiously deepens around $\rho_{pol} = 0.98$ until the typical H-mode transition value on AUG below -15 kV/m [67] is reached. On top of this

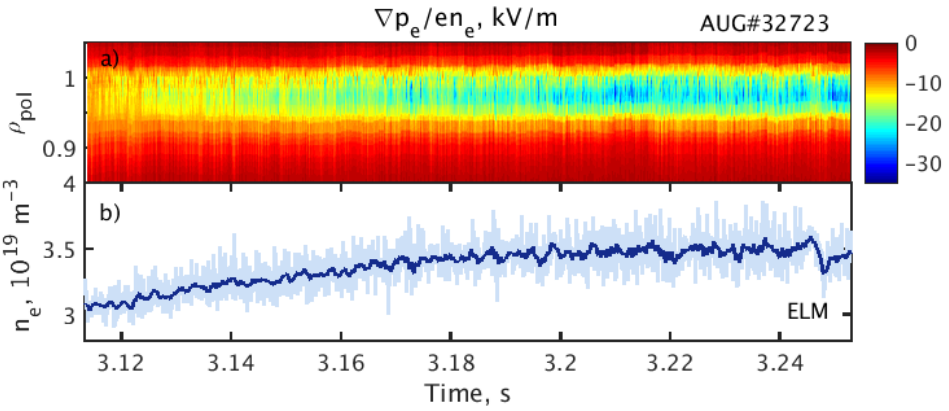

Figure 6.6: (a) Normalised electron pressure gradient, (b) edge electron density during the I-phase (3.117–3.245 s)

evolution, E_{r0} undergoes higly localised kHz oscillations.

After a heating pulse significantly exceeding the power threshold for an L-H transition, the I-phase is typically short. The discharges #31287, #32723 and #32944 have been chosen as representative cases of various plasma conditions. The discharge #31287 represents a low-density case, with the core density of about $4 \cdot 10^{19}$ m^{-3} and a fast L-H transition with a short I-phase duration of 10 ms (Fig. 6.1). The discharge #32723 shows a longer I-phase of 130 ms in a He plasma with a high central density of $7 \cdot 10^{19}$ m^{-3} (Fig. 6.6). The discharge #32944 is a medium-density case ($4.5 \cdot 10^{19}$ m^{-3}) with an I-phase lasting 20 ms. The behaviour of density gradient and density fluctuations are similar for the three indicated cases. The frequency of I-phase oscillations is lower for high density discharges [80], so the analysis of this case provides better statistics with a given time resolution and thus the focus will be on the discharge #32723 where the UFSR data contain 200,000 sweeps of 1 μs.

In AUG the I-phase can typically be identified in a poloidal Mirnov coil signal $\partial B_\theta / \partial t$ as low kHz range oscillations as it is shown in the zoom on the first I-phase oscillations (Fig. 6.7e) for the Mirnov coil C09-23 situated close to the X-point. The periodic suppression of the turbulence level is visible in the amplitude of the Doppler reflectometer signal after $t = 3.1171$ s (Fig. 6.7d) and synchronously in the density fluctuation level measured by the UFSR at about $\rho_{pol} = 0.96$–1 (Fig. 6.7a,b). Similar bursts have been found with a high temporal resolution in the normalised electron

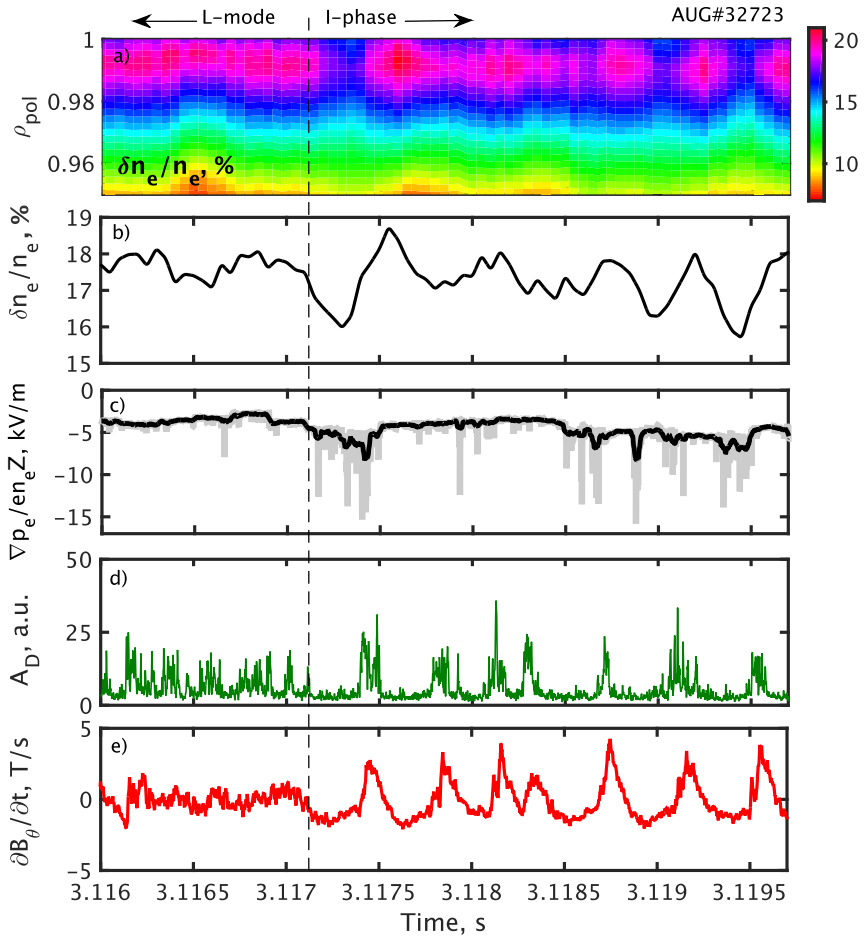

Figure 6.7: (a) Density fluctuation level in the plasma edge, (b) at $\rho_{pol} = 0.99$, (c) normalised ectron pressure at $\rho_{pol} = 0.99$, (d) Doppler reflectometer signal amplitude for $F = 80$ GHz, (e) Mirnov coil signal during the first oscillations of the I-phase

pressure gradient (E_{r0}) evolution in the pedestal region. Figure 6.7c depicts E_{r0} in grey with the time resolution of 10 μs and in black with the average of 100 μs for density. The close-up on the oscillations shows that during one period of the I-phase E_{r0} changes by about 30 % , the crash to the lower absolute level (as at t = 3.1174 or 3.1195 s) being synchronised with the magnetic signal $S_{mag} = \partial B_\theta / \partial t$ bursts and an increase of the density fluctuation level $\delta n_e / n_e$. Although the first oscillations of the I-phase (t =3.1175–3.119 s) have irregular character, during the most part of the I-phase the deep negative values of E_{r0} appear between the turbulence bursts and the crash of E_{r0} happens together with the turbulence increase. Before the very first I-phase burst at t = 3.1174 s the turbulence level drops and the E_{r0} minimum reaches the typical threshold for L-H transition, this stage will need further investigation to understand the triggering mechanisms of the transition.

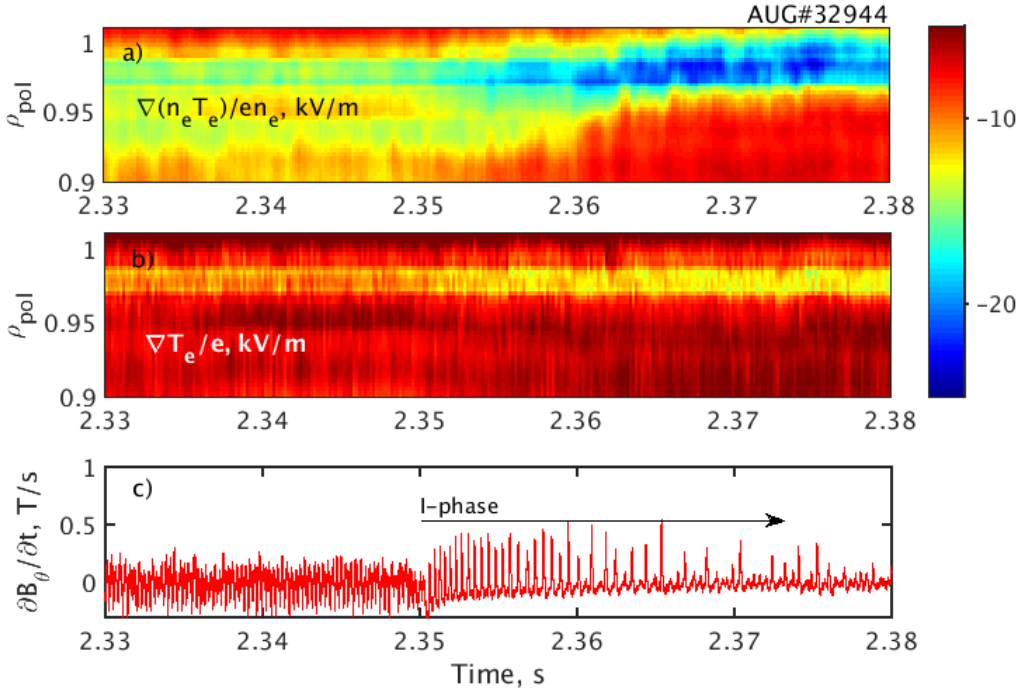

Figure 6.8: (a) Nomalised electron pressure, (b) $\nabla T_e/e$ contribution and (c) magnetic signal $\partial B_\theta / \partial t$ during the I-phase t =2.35–2.37 s

The medium density I-phase is shown in Fig. 6.8. The signal from the Mirnov coil defines the beginning of the I-phase at 2.35 s. The contribution of the temperature

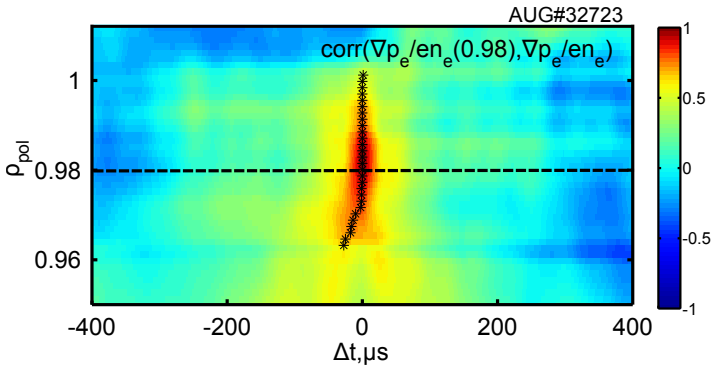

Figure 6.9: Correlations of the neoclassical estimation E_{r0} at different radial positions and the propagation of its modulation inside the separatrix

gradient term to the pressure gradient is about 50 %. The temperature spatial resolution does not allow to follow the radial movement of the E_{r0} minimum, while the density gradient shifts the normalised pressure gradient minimum from $\rho_{pol} = 0.96$ to 0.98 during the I-phase (Fig. 6.8a). Hence the precise measurement of the density and its gradient ensures a better understanding of the I-phase dynamics.

In order to follow the displacement of E_{r0}, the radial correlation of $E_{r0}(\rho_{pol})$ with respect to E_{r0} at $\rho_{pol} = 0.98$ has been constructed (Fig. 6.9) for the time window $t =$ 3.191–3.194 s. The maximum of the correlation function for each radial position is marked with a black cross. The correlation function is periodic in the time delay Δt with the I-phase oscillation period of 1.3 kHz. The E_{r0} modulation propagates from the top of the pedestal to $\rho_{pol} = 0.98$. The crash of E_{r0} happens simultaneously within the given time resolution at all radial positions from $\rho_{pol} = 0.98$ to the separatrix. At the separatrix the E_{r0} modulation changes the phase by π, i.e. is anti-correlated with the modulation within the last closed magnetic surface. The time delay between inner radial positions is of the order of 30 μs and should be considered in the analysis of the relative phase. The correlation rapidly decreases to the noise level for $\rho_{pol} < 0.96$ which means that the I-phase E_r modulation is localised in the pedestal region. The anticorrelation inside and outside the separatrix has the usual characteristics of a crash of the edge density gradient.

The evolution of the pressure is accompanied by a significant change of the density profile. During one burst of the I-phase the density crashes inside the separatrix

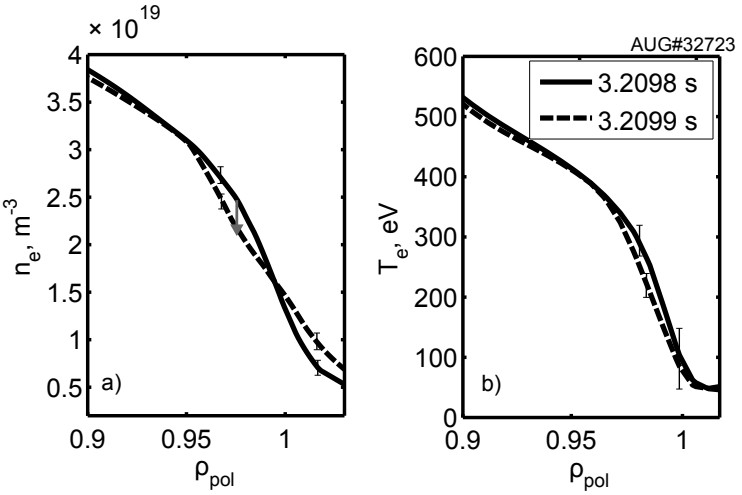

Figure 6.10: Example of density (a) and temperature (b) profile dynamics during a late I-phase burst

and grows outside (Fig. 6.10), which is similar to the behaviour during ELMs with a periodic outward particle expulsion. The pedestal top density changes by about 15–20 %, crashes in 100–200 μs and rebuilds until the next crash during 300–1000 μs. The density evolution is taken into account for the Doppler reflectometer measurement position. The pedestal top temperature oscillates as well with 5–10 % amplitude within the same time intervals but tends to not be distinguishable within the error bars.

6.3.3 Established I-phase as ELM-like phenomenon

A long I-phase with many periods of oscillations (> 10 ms) can be devided in two parts: the early I-phase where the oscillation frequency changes significantly during several periods and the established I-phase where it can be cosidered constant during at least ten periods. The period of the I-phase changes from 400 μs in the early I-phase to 1 ms before the first ELM. The late or established I-phase in the medium to high density discharges can be characterised by the regularity of its bursts and by the zero phase shift between the turbulence and the neoclassical electric field. Indeed, the cross-correlation function reconstructed between the density fluctuation level $\delta n_e/n_e$ and E_{r0} at $\rho_{pol} = 0.98$ for a time window of 10 ms in the established I-phase demonstrates the absence of the phase shift (Fig. 6.11, black solid) within a time resolution of 10 μs. This can be interpreted as the absence of predator-prey interaction between the neoclassical

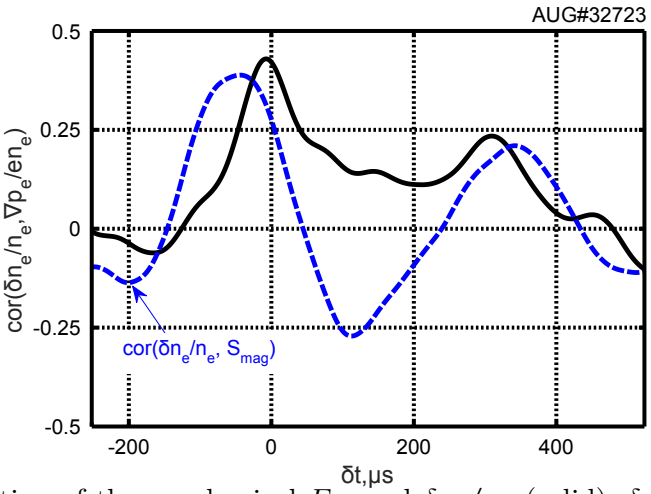

Figure 6.11: Correlation of the neoclassical E_{r0} and $\delta n_e/n_e$ (solid), $\delta n_e/n_e$ and $\partial B_\theta/\partial t$ (dashed) at $\rho_{pol} = 0.98$ for time window t = 3.19–3.20 s, AUG#32723

E_{r0} and the turbulence with radial wavenumbers of 1–10 cm^{-1}. A small negative phase shift indicates that the fluctuation level increases during the strong E_{r0} phase since the steep pressure gradient drives the edge instabilities. Note that the oscillations in the early I-phase are not regular and their frequency evolves too fast to allow a reconstruction of the correlation function over a time window with 10–20 oscillations.

Both E_{r0} and the turbulence level oscillations are slightly shifted with respect to the magnetic signal (Fig. 6.11, blue dashed) in the established I-phase. The shift of the correlation function of $\Delta t = 50$ μs visible also in Fig. 6.7b,e is probably due to the location of the Mirnov coil close to the X-point compared to the mid-plane position of the UFSR. This shift indicates that the I-phase oscillations propagate from the X-point to the top of the tokamak from the low-field side. This behaviour is consistant with the magnetic structure and the poloidal propagation of the I-phase oscillations discussed in [80].

The DR data from three fixed frequency channels (80, 85 GHz X-mode and 55 GHz O-mode) have been used for the comparison between the total E_r and the neoclassical estimate E_{r0}. Only the points with the signal amplitude A_D (Fig. 6.12a, black line) higher than three times the noise level (Fig. 6.12a, magenta) were taken into account. The density profile evolution changes the position of DR measurement and makes all the channels scan the region of $0.96 < \rho_{pol} < 1$. The wavenumber calculated from the beam tracing changes by about 5–15 %. Therefore, in order to obtain the measurement from the position nearest to the E_r well minimum, for each time window of 10 μs the

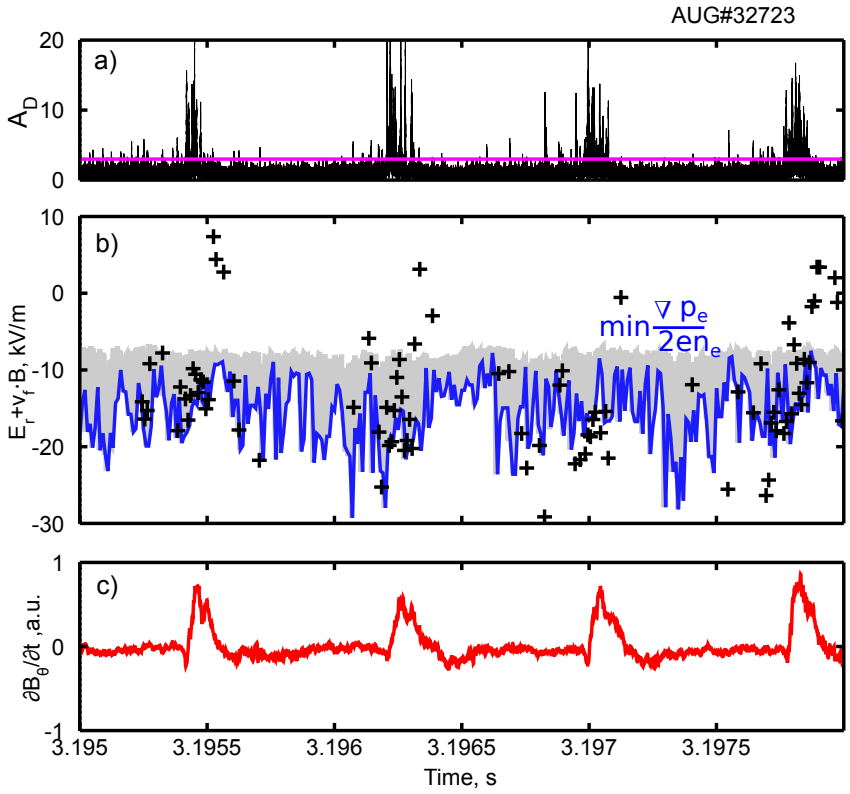

Figure 6.12: Doppler reflectometer signal amplitude at F = 80 GHz, X-mode a), estimation of E_r minimum value from 3 channels of Doppler reflectometers (crosses) and neoclassical electric field minimum estimation E_{r0} (grey) and its minimum values inside windows of 10 μs (blue) b), the Mirnov coil signal $\partial B_\theta/\partial t$ c) indicates the I-phase bursts

minimum value from the 3 channels has been selected.

The result of this selective procedure is shown in Fig. 6.12b with crosses and is taken as an estimation of the E_r minimum value. Note the Doppler reflectometer measurement corresponds to the sum of three terms $E_r + \frac{u_r k_r}{k_\perp} B + v_f B$, where the first term is dominant if the radial movement of plasma is excluded and the phase velocity v_f is considered small. In order to compare similar quantities, the E_{r0} minimum (grey line) was calculated for time windows of 10 μs and the minimum value for each window is shown as the blue line. The fast oscillation of the normalised pressure is probably due to the small radial movement of plasma.

In between the bursts the estimated E_r minimum values agree with the neoclassical E_{r0} at ρ_{pol} =0.97–0.99. At this stage the absence of a strong phase velocity and of E_r^{ZF} can be supposed. In this case the I-phase could be explained by edge pressure driven instabilities that lead to a crash of the pedestal pressure with particles expulsion. The edge coherent modes observed around 100 kHz might be precursors and support the relation of the crashes with type-III ELMs [80].

The E_r minimum value at the end of the fluctuation bursts shows positive values (Fig. 6.12b). This fact could be related to the expulsion of filaments accross the separatrix which then are advected in the opposite direction in the SOL. Also the radial velocity of such filaments could lead to positive Doppler shifts if the $k_r v_r$ contribution to the Doppler reflectometer frequency shift becomes important (see Chapter 4.10). In addition ELMs simulations have shown an inversion of the filaments rotation direction during the crash even inside the separatrix [131], which is also observed in some experiments [132]. Such effects should be studied by full-wave codes in the future.

6.3.4 Controversial early I-phase

The beginning of the I-phase needs to be analysed more carefully as it contains irregular oscillations with different phase shift. Figure 6.13 shows the comparison of the turbulence level, total E_r minimum and E_{r0} in the He plasma discharge #32723. To analyse the relative phase shift, $E_{r0} = \nabla p_e / 2en_e$ (Fig. 6.13b, black solid line) and the density fluctuation level (Fig. 6.13a) have been taken at the minimum E_{r0} position around ρ_{pol}=0.98 and the DR data (Fig. 6.13b, blue crosses) have been treated as mentioned above with windows of 20 μs. It has been found that for the very first I-phase periods in high (#32723, Fig. 6.13) and medium (#32944) density discharges the turbulence

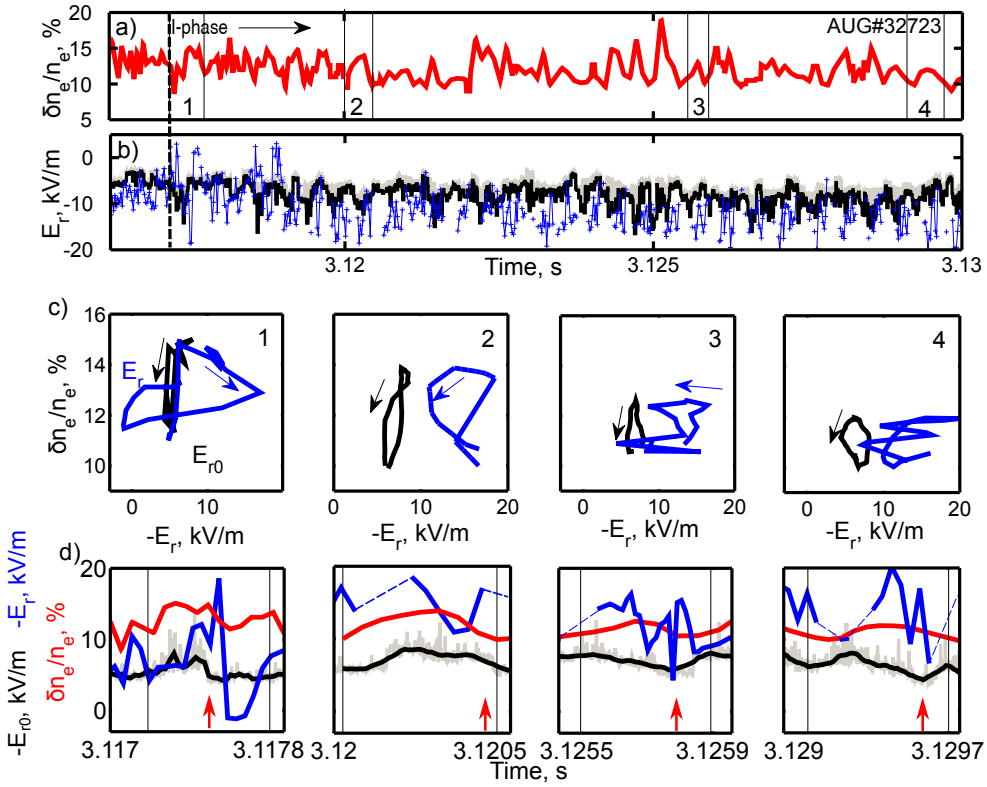

Figure 6.13: The beginning of the I-phase in #32723 from the UFSR: (a) turbulence level at $\rho_{pol} = 0.98$, (b) the minimum of E_{r0} (black solid line) and of E_r (blue crosses) from Doppler reflectometer, (c) the evolution of turbulence level and E_{r0} (black) or E_r (blue dash) amplitudes on the phase plane for individual periods of I-phase and the corresponding time traces (d)

level and E_r amplitudes create open loops in the clockwise direction on the phase space plane (Fig. 6.13c, 1), which are typical for the predator-prey interplay between the flow and the turbulence. In the following periods of the I-phase both E_r and E_{r0} create loops in the counter-clockwise direction showing both the same behavior albeit with wider loops (Fig. 6.13c, 2-3) for E_r. After several periods, E_{r0} and E_r synchronise their phases with the turbulence level (Fig. 6.13c, 4) and the cycles collapse into lines within the given resolution. The time traces (Fig. 6.13d) show that the bursts of the fluctuation level provoke the relaxation of the E_{r0} well and the following increase of the pressure and its gradient first supresses the turbulence and later drives edge instabilities

causing the next burst. Note that the E_{r0} oscillations have a stronger amplitude prior to the bursts and a smaller variation immediatly after the pressure gradient relaxation. The Doppler measurements are only ploted when the signal amplitude allows to extract E_r values, they are connected by a dashed line (Fig. 6.13d).

6.4 Summary

First studies of the electron density profile dynamics, turbulence level, k_r- and frequency spectra during L-H transitions in ASDEX Upgrade have been performed with a time resolution of 1 μs. The reconstruction of the turbulence level with a closed-loop procedure needs to be constrained in the spectral indices. Although the X-mode reflectometry for these discharges might operate in the non-linear regime, the UFSR measurements indicate that the low k_r density fluctuation level decreases in the pedestal region after an L-H transition.

In the observed I-phases an important contribution of the density gradient to the neoclassical E_r has been confirmed. The I-phase bursts at medium to high density might be explained by growing pressure driven edge instabilities which cause a pressure crash consistent with previous studies on AUG [80]. The edge coherent modes observed in the frequency spectra support this description and can be considered as a precursor, similar to those of type-III ELMs.

The fluctuation level extracted from the UFSR data contains not only the turbulence itself but also the radial density profile movement and the density in expulsed plasma filaments. During the I-phase, the density profile modification due to the burst starts from the pedestal region leading to a simultaneous destruction of the pressure gradient within $0.97 < \rho_{pol} < 1$ consistent with DIII-D results [122]. The crash of the neoclassical electric field estimate E_{r0} is in phase with turbulence level, pick-up coil bursts and Doppler reflectometer measured E_r, which indicates the absence of predator-prey oscillations in the established I-phase.

However, some evidences are found that the first few periods of the I-phase could have a different phase behaviour. In the first cycle the neoclassical estimate E_{r0} deepens together with the drop of the turbulence level, while the Doppler reflectometer measured E_r has a positive phase shift with respect to the turbulence level as it was observed previously for the low density I-phase [11]. First the turbulence starts to grow with the increasing presure gradient, then the strong flow velocity appears and the turbulence

level decreases. This could be a consequence of an interplay between zonal flow, the background flow and the turbulence, which might have an impact on the transition from L-mode to the I-phase. Note that the phase shift, if there is any, is shorter than 150–200 μs, therefore it can be measured only with the diagnostics of a higher temporal resolution. At this point it is important to stress, that this observation is based on Doppler reflectometer signals which only for short time intervals are strong enough to extract a flow velocity. Further studies are needed to identify the physics of these interesting events and to relate these observations unambiguously to the mean background flow. Nevertheless, the established I-phase in the medium to high densities presents clear features of the ELM-like behaviour.

7 Edge coherent modes

The modes which can be observed in a confined magnetized plasma are related to instabilities caused by different drives, like pressure gradient or fast particles. The goal is to identify the basic properties of such instabilities, which can be measured in the experiment: the growth rate, the poloidal and toroidal mode numbers m, n, the mode frequency ω, the modes' radial structure. In practice the growth rate can be found if the temporal evolution of the mode amplitude is obtained. The mode numbers and frequency can be calculated from the analysis of the magnetic pick-up coil signals giving the temporal derivative of the magnetic field components B_r and B_θ. The main disadvantage of the pick-up coils is their non-local measurement outside the plasma, related to their position. Therefore only modes with high amplitude can be detected and they need an electromagnetic component to be detectible outside the plasma. In addition the magnetic component can be screened by the plasma. If a mode is associated to density perturbations, it can be observed in reflectometry signals by the reconstruction of the frequency spectrum. In contrast to the Mirnov coils this measurement has a local character. Using several probing wave frequencies, the mode can be localised radially. In addition the temporal dynamics can be studied on a time scale of the window used in a fast Fourier transform (FFT). However, these characteristics do not determine the modes driving forces which should be found from a detailed analysis of plasma conditions and mode characteristics.

Previous experiments on different devices reported the onset of high frequency modes with $f > 40$ kHz in the plasma edge region in high confinement regimes [12, 133]. The underlying instabilities could be the reason for the limitation of the pedestal gradients after the transition to the improved confinement. In the standard H-mode quasi-coherent modes are thought to play a role in the inter-ELM dynamics by clamping the pressure gradient. These modes have nature of either kinetic ballooning modes (KBM) or microtearing modes (MTM) [134, 135]. The "edge harmonic oscillation" (EHO) has been observed on magnetic probes, in the temperature and density measurements in the

pedestal region during the quiescent H-mode in DIII-D [12]. Several branches with mode numbers n =1–10 were observed in the spectra, although they simply corresponded to the Fourier harmonics needed to describe a non-sinusoidal periodic oscillation. The EHO was described as a MHD oscillation in ASDEX Upgrade and JET, with the fundamental harmonic at a toroidal mode number $n = 1$ [133]. The disappearance of the EHO after each ELM and its onset with the recovering pressure suggested that the pressure or edge pressure gradient in the pedestal region might drive the mode. Later the EHO was modeled as a saturated kink/peeling mode destabilized by plasma current gradient and rotation and limiting the edge pressure gradient[136]. Accompanying the EHO, high frequency fluctuations were observed in the plasma edge with the frequencies in the range of 200 to 500 kHz during the quiescent H-mode [133] and in between ELMs [137].

Another type of magnetic fluctuations has been classified under the name of washboard modes [138] which appear between type-II ELMs in JET and have a strong dependence of the frequency evolution on the edge electron temperature measured close to the pedestal top. Resistive ballooning or microtearing modes have been regarded as a possible candidate to explain the washboard modes.

In several devices coherent modes around 100 kHz were observed in the edge with characteristics different from EHO modes. Quasi-coherent modes were observed as a drive for the coherent modes in the steep edge gradient region with typical frequencies of about 100 kHz in Alcator C-Mod [139]. In EAST the edge coherent modes were identified as trapped electron modes (TEM) [140].

In a toroidal plasma also various forms of Alfvén eigenmodes can be excited by energetic particles, for example the Toroidal Alfvén eigenmode (TAE) [141]. The modes with multiple branches in the range around 100 kHz can also be Alfvén modes seen in neutral beam heated as well as in Ohmic plasmas in TFTR tokamak [142] for instance. Thus several types of oscillations with similar properties can manifest after the transition to the H-mode and the experimental evidence allows for various interpretations.

This chapter summarises the results obtained in the study of the coherent modes in ASDEX Upgrade which have common characteristics, such as their frequency range of 50–200 kHz and edge radial position, and thus will be grouped under the name of edge coherent modes (ECM). They appear in different plasma confinement regimes, such as the I-phase, ELM-free or ELMy H-mode. Section 7.1 describes the general observations, sections 7.2, 7.3, 7.4 present the analysis of the modes' behaviour during respectively

the ELM-free phase of the H-mode, the ELMs and the I-phase.

7.1 Observation of modes with the UFSR

Different edge coherent modes (ECMs) have been detected in the reflectometer signals during the experiments dedicated to the L-H transition studies on AUG. First appearing as sequences of pulsations in the raw reflectometer phase signal the modes could later be visible in the frequency spectra. Almost in all cases the modes start to be visible in the pick-up coil signals a few milliseconds later and therefore have an electromagnetic nature. The modes have been observed in the UFSR signal continuously during the I-phase, after the transition to the ELM-free phase of the H-mode and in between ELMs. The mode frequency is in the range of 40–200 kHz and often several branches are observed simultaneously. This observation is similar to the washboard, high frequency modes or Alfvén eigenmodes [143]. However, the latter are usually observed when NBI creates a population of fast particles, while the modes studied here were also found in discharges without NBI. This feature necessitates to question more accurately their nature. ECMs were previously investigated in AUG in between ELMs, although they were not decisively identified [137, 144].

The ECMs develop as it is shown in Fig. 7.1. In the pedestal region during the I-phase the density fluctuation amplitude decreases and the spectra become narrower compared to typical L-mode spectra which are more broadband. The modes start to grow directly at the transition from the L-mode to the I-phase in the edge region $0.90 < \rho_{pol} < 0.98$ and their amplitude saturates during the ELM-free phase of the H-mode. The oscillations occur within the range of 60–80 GHz of UFSR probing frequencies, corresponding to the edge region inside the separatrix. In between ELMs the modes become saturated again. An important feature of these modes is their coherency, meaning that in the frequency spectrum they have a distinctive narrow peak above the noise level with a width $\Delta f \ll f$. At the same time, the rest of the usual broad L-mode spectrum is suppressed when the modes increase in amplitude. Summarising the aforementioned characteristics, the modes were named edge coherent modes.

Note that the radial position for each spectrum is defined from a bijective relation $\langle F_{prob,i}(t)\rangle \leftrightarrow \langle \rho_{pol,i}(t)\rangle$ where the probing frequency F_{prob} and corresponding radial positions ρ_{pol} are averaged over the FFT time window of typically a few milliseconds.

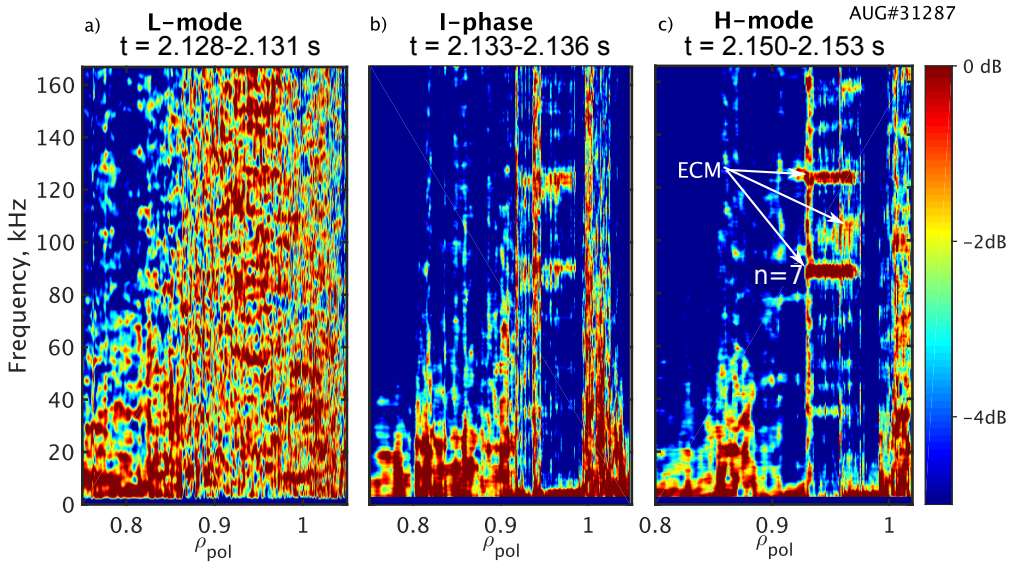

Figure 7.1: Density fluctuation frequency power spectra in (a) L-mode, (c) H-mode and (b) during I-phase

In the example of Fig. 7.1 this window was 3 ms. Figure 7.2a depicts the dependence of the radial position from the probing frequency for 1000 consecutive sweeps. During this time each reflectometer frequency $F_{prob,i}$ probes a different radial position from one sweep to another around an average position $\langle \rho_{pol,i} \rangle$ due to the density profile dynamics, hence the actual shift of the profile can introduce an additional extension of the estimated mode position. Usually the shift of the profile is within 2.5 cm in the edge, which is about 0.05 in terms of ρ_{pol}. Figure 7.2b shows an example of the frequency spectra for all probing frequencies. The ECMs are visible around 90 and 125 kHz for the probing frequencies of 70–75 GHz. These probing frequencies clearly correspond to the top of the pedestal as it is shown in Fig. 7.2a with the red rectangle, the absolute position is around 2.1 m with the precision of 2–3 cm.

Figure 7.1 illustrates the development of ECMs after the L-mode (a) during the I-phase (b) and in H-mode (c) in a low density discharge #31287 with 1.6 MW of ECRH. In the case of Figs. 7.1b,c the strongest modes have frequencies of 90 and 125 kHz. When examining the pick-up coil spectrogram (Fig. 7.3a), the modes are not yet visible during the first 18 ms after the L-I-phase transition. They appear in

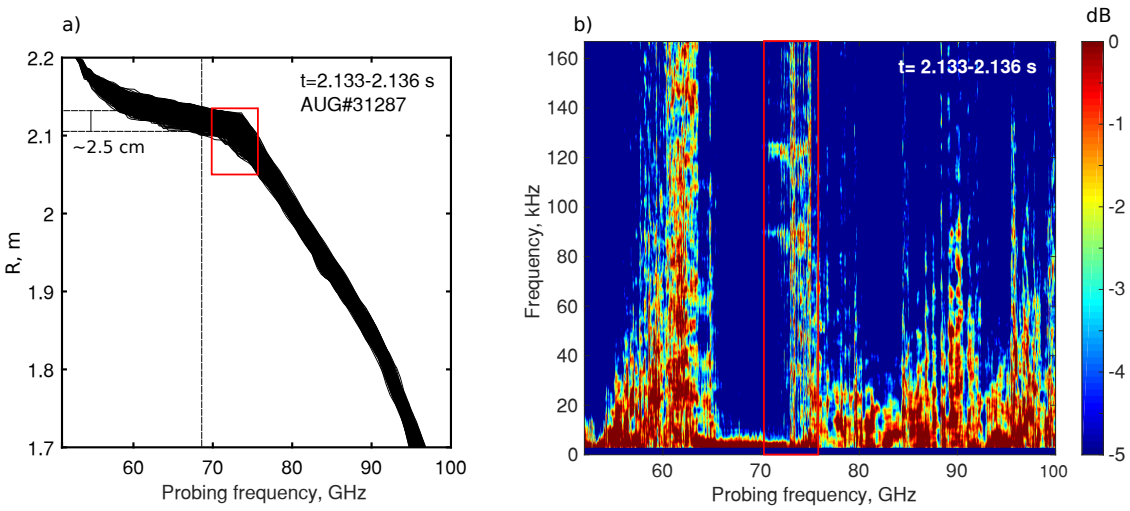

Figure 7.2: (a) Absolute position of USFR measurement during the I-phase AUG#31287 for different probing frequencies within the time window $t = 2.133 - 2.136$ s of typical FFT, one probing frequency in the edge region may correspond to the radial positions within 2.5 cm; (b) frequency spectra for all probing frequencies, the ECMs are measured with probing frequencies of 70–75 GHz, corresponding to the top of the pedestal, shown with the red rectangle in the left figure.

the spectrogram only after $t = 2.15$ s with branches around 70–100 kHz (Fig. 7.3a). The mode at 125 kHz is not visible in the magnetic pick-up coils while being clearly observed with the UFSR.

The magnetic pick-up coils (B31-01, B31-02) were used to deduce the toroidal mode numbers as described in Chapter 4.8. They vary between $n = -2, \ldots, -7$ (Fig. 7.3a) for the lowest to the uppermost branch (the negative sign corresponds to the electron diamagnetic direction in the laboratory frame). Usually the distance between the coils does not allow to detect mode numbers higher than 16 [144], but the main limitation for the mode detection is the plasma screening. The most pronounced branches in the magnetic pick-up coil spectrum correspond to $n = -5$ and $n = -6$ and frequencies of 70–80 kHz, while in the UFSR signal the modes with frequency of 115–125 kHz have the strongest amplitude. The UFSR frequency spectra (Fig. 7.3b) are constructed for the window 2.153–2.156 s which is indicated in Fig. 7.3a by the shaded area. The mode's location slightly varies for different n: $n = -5$ and $n = -7$ are more visible at the top of the pedestal $0.95 < \rho_{pol} < 0.97$ while $n = -6$ is shifted to the core

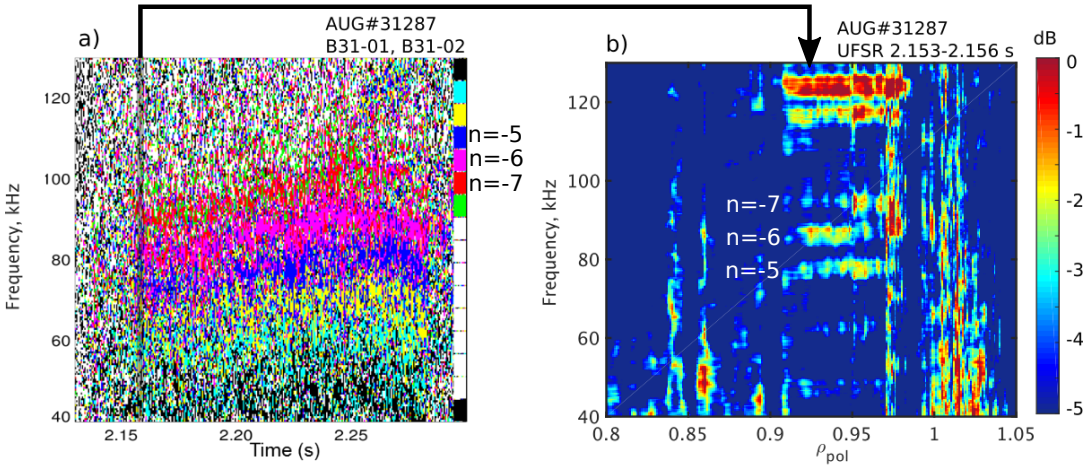

Figure 7.3: (a) Frequency evolution of toroidal mode numbers n found from the Mirnov coils signals and (b) the frequency spectra from UFSR at 2.153–2.156 s of the discharge #31287 (the time window is indicated in plot (a) by the shaded area)

$0.92 < \rho_{pol} < 0.95$. Assuming the same propagation velocity for the modes visible in the spectra with frequencies around 115 and 125 kHz and the modes with $n = -5$ to -7, the corresponding mode numbers would be $n = -10$ and $n = -11$, not detected in the pick-up coil analysis. Similar modes with toroidal mode numbers from $n = -3$ to -12 and poloidal mode numbers around $m = 30$ for the lower n numbers were described in [145] as MHD activity between ELM bursts in AUG. Their position was estimated by matching their frequency and mode number to the background $\mathbf{E} \times \mathbf{B}$ velocity and was found to be between the E_r minimum and the separatrix. The UFSR system identifies these modes at the pedestal top.

For a typical H-mode in AUG, the profile of the radial electric field (Fig. 7.4) has its minimum around $\rho_{pol} = 0.99$. E_r changes its sign from negative in the pedestal region to positive in the plasma core, therefore the $\mathbf{E} \times \mathbf{B}$ velocity of the plasma changes its direction from the electron diamagnetic to the ion diamagnetic velocity direction. As the ECMs propagate in the electron diamagnetic direction in the laboratory frame and are located on the top of the pedestal where the $\mathbf{E} \times \mathbf{B}$ velocity is low, it is likely that the modes also propagate in the electron diamagnetic direction in the plasma frame. However, this observation should be checked in dedicated experiments. Nevertheless, the direction of the propagation might indicate that the modes have the nature of microtearing modes (MTM) [147]. This would be consistent with the gyrokinetic

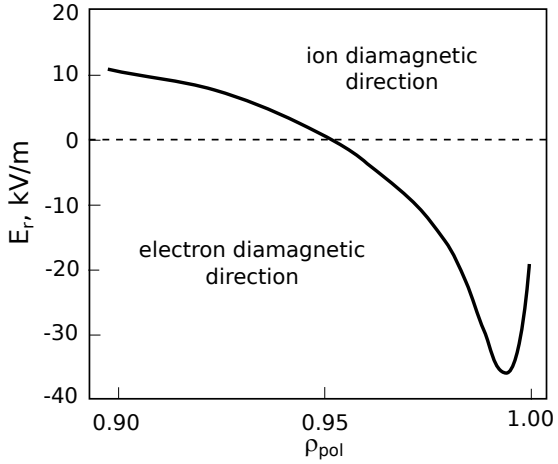

Figure 7.4: Typical radial electric field in H-mode in AUG defines the $\mathbf{E} \times \mathbf{B}$ velocity which corresponds to the electron diamagnetic direction in the pedestal region and changes the direction for ρ_{pol} <0.90–0.95 (adapted from [146])

simulations which have shown that MTM can be a dominant instability responsible of the transport at the pedestal top [148]. The formation of the pedestal has been described as an interplay between the MTMs regulating the temperature gradient and transport inside the pedestal and the KBMs limiting the density gradient in the pedestal foot [46]. It is possible that first the MTMs are destabilised at the top of the pedestal during the I-phase and the ELM-free H-mode and that they are not visible in the pick-up coil signal because the level of magnetic fluctuations is low [147]. Then the KBMs are driven at the same frequency at the pedestal foot and thus are detectable with Mirnov coils.

The mode's frequency also lays in the range of the typically observed toroidal Alfvén eigenmodes (TAE) in AUG [143]. The Alfvén frequency is given by

$$f_A = v_A/2\pi qR \sim q^{-1}{n_i}^{-0.5}, \tag{7.1}$$

where the Alfvén speed is given by $v_A = B/\sqrt{\mu_0 n_i m_i}$, q is the safety factor (3.1), m_i is the ion mass, n_i is the ion density, R is the major radius, μ_0 is vacuum permeability.

It is important to note that ECM have been observed in plasmas with both ECR and NBI heating, with only NBI and only ECRH. Hence, the presence of ECMs does not rely on energetic ions which usually excite TAEs. For a fixed value of the parallel wavenumber, the TAE frequency constitutes a continuous spectrum with a gap which defines the modes' localisation [141]. The gap is produced because two branches of

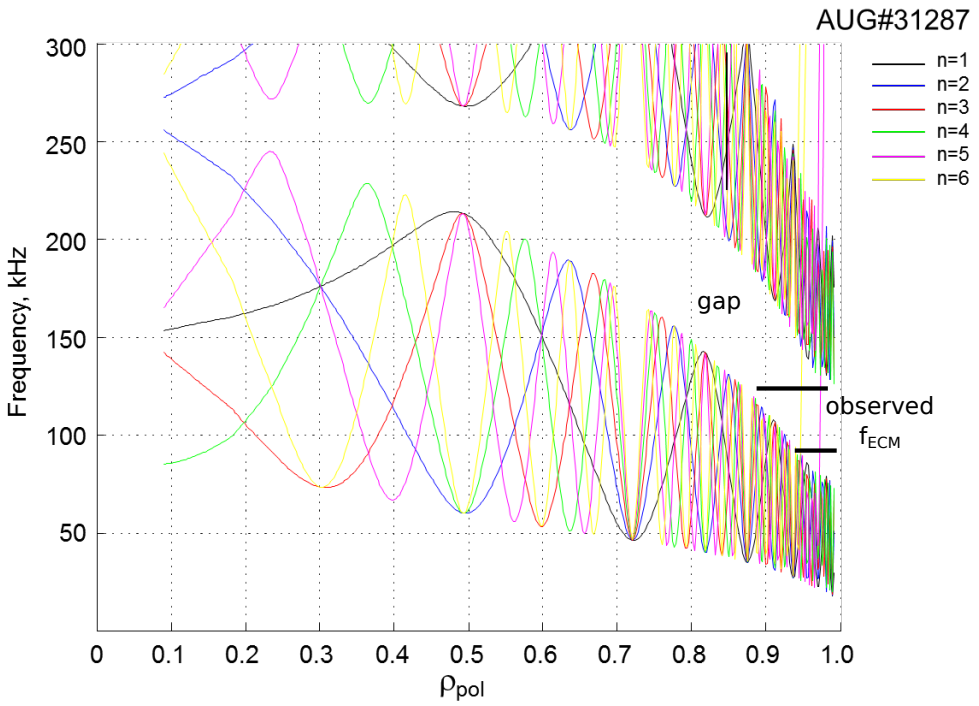

Figure 7.5: In the gap TAE can be excited, solid black lines indicate observed frequency of the ECMs measured with the UFSR, $t = 2.14$ s [kindly provided by A. Biancalani, IPP]

Alfvén waves with poloidal mode numbers m and $m+1$, satisfying the dispersion relation $\omega_A = v_A(R)|k_\parallel| = v_A(R)|m - nq|/qR$, have a crossing point at the resonant surface with $q = (2m+1)/2n$ [149]. At this point the modes have degenerated energy states [150]. The frequency of the gap centre can be approximated as $f_{TAE} = f_A/2$. For the discharge #31287 the TAE continuous spectrum has been calculated (Fig. 7.5) for cylinder geometry [151] at $t = 2.14$ s during the I-phase, where the ECMs are observed at frequencies 90–125 kHz. The gaps are superposed for different toroidal mode numbers n =1–6. The frequencies of ECMs (Fig. 7.5, black lines) fall in the gap in the edge region $0.9 < \rho_{pol} < 1$ where TAE can exist.

From the same discharge the temporal evolution of the mode frequency (Fig. 7.6a) has been compared to the density and temperature dynamics. Figure 7.6 depicts the evolution of the electron density (b) and temperature (c) at the top of the pedestal from Thomson scattering during 170 ms of the discharge after an L-H transition. The frequency of the ECM with toroidal mode number $n = -7$ measured with pick-up coils

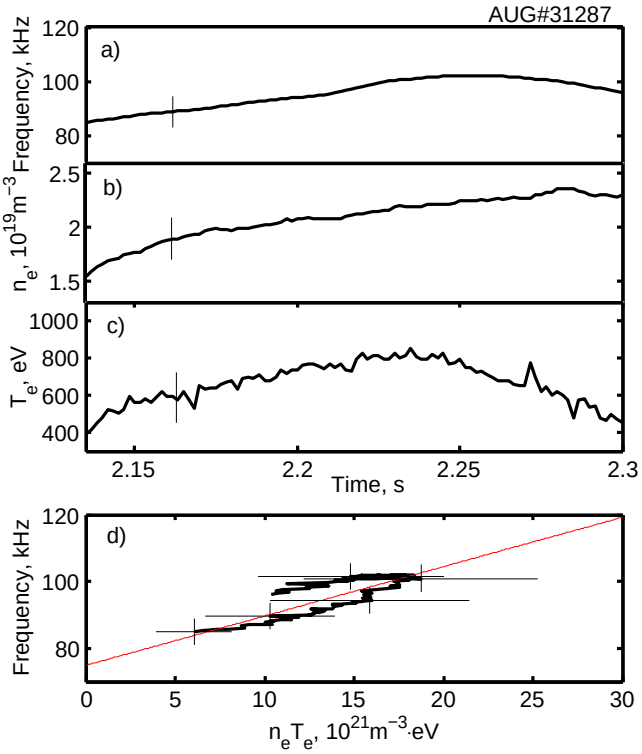

Figure 7.6: (a) ECM frequency evolution for the $n = -7$ mode compared to (b) the edge electron density, (c) temperature and (d) electron pressure dependence of frequency at $\rho_{pol} = 0.97$ in the discharge #31287

follows the temperature and density dynamics, although the temperature is changing faster than the ECM frequency, while the density starts to decrease later. The frequency of the mode does not follow the ${n_i}^{-0.5}$ dependence of the Alfvén frequency (7.1), therefore the ECMs are not TAEs, which is also consistent with the fact that they are observed in ECRH only discharges. The best fit for the density and temperature dependence is $f \propto n_e T_e$ on the top of the pedestal (Fig. 7.6d), which can be a rough estimate for the pressure gradient, assuming the pedestal width is not changing much. Note that the MTM frequency scales with the electron diamagnetic velocity also proportional to the electron pressure gradient.

The analysis of the density fluctuations though becomes complicated as the coherent modes dominate the turbulent spectrum. In order to distinguish density fluctuations due to these modes and broadband turbulence, a low-pass filter $f < 50$ kHz, filtering out the ECM, has been applied to the UFSR signal phase. The density fluctuation profile

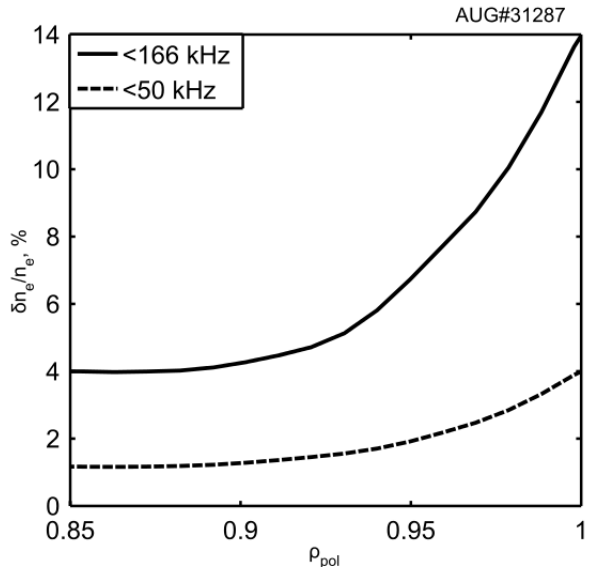

Figure 7.7: Density fluctuation level for frequencies $f < 166$ kHz (solid) and $f < 50$ kHz (dashed) in the ELM-free phase of the H-mode with ECMs, $t = 2.141$ s

shape is unchanged after filtering (Fig. 7.7), the absolute level of density fluctuation decreases proportionally to the filter width, hence the ECMs do not contribute to the selected k_r range from 2 to 20 cm^{-1}. In contrast to the previous analysis where the time traces at one radial position are used, the calculation of the density fluctuation level here uses the closed-loop method where the wavenumber spectra are reconstructed and then integrated over a selected range of k_r. That indicates that the edge coherent modes have a small $k_r < 2$ cm^{-1}, corresponding to a size of about 1.5 cm which is consistent with the mode's width in Fig.7.1. Hence the closed-loop method (Section 5.2.3) is not suitable to follow the dynamics of the edge coherent modes.

Summarising the observations, ECMs are localised in the edge region $0.87 < \rho_{pol} < 1.00$, with indications from the UFSR that they are mostly located on the pedestal top. They saturate after the transition to the I-phase or the H-mode and disappear only during and shortly after ELM crashes. The toroidal mode numbers change from -2 to -11, they propagate in the electron diamagnetic direction. The ECMs have a small radial wavenumber $k_r < 2$ cm^{-1}. In ECR heated discharges without NBI the ECM frequency increase with electron pressure at the top of the pedestal. The ECMs have features of MTMs, TAEs have been excluded as possible explanation.

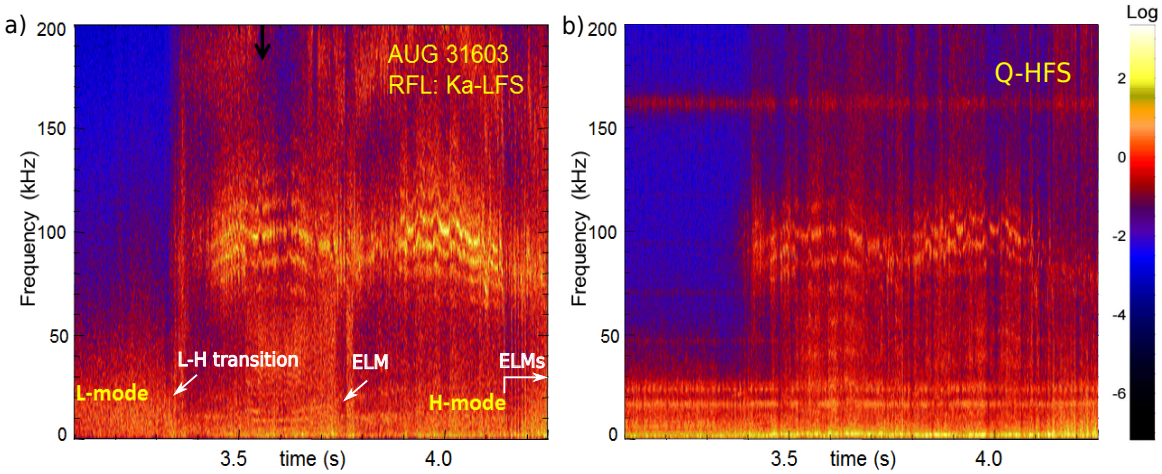

Figure 7.8: Spectrogram of phase fluctuations in the pedestal region during ELM-free phase of the H-mode reconstructed from the fixed frequency reflectometer signal with $F_{prob} = 36$ GHz (a) from the LFS and (b) with $F_{prob} = 39$ GHz from the HFS [kindly provided by V. Nikolaeva, IST]

7.2 Edge coherent modes in the ELM free phase of the H-mode

In an ELM-free phase of an H-mode the observation of ECMs is more convenient as the plasma is perturbed neither by I-phase bursts nor by ELMs. Usually the ECMs are simultaneously visible on the spectrogram of the fixed frequency reflectometer phase and magnetic pick-up coil signals where the different frequencies branches are well distinguishable.

In the fixed frequency reflectometer (see Section 4.9) spectrograms the modes are visible in the edge region $0.95 < \rho_{pol} < 1$ at several O-mode frequencies 22, 36, 39 and 50 GHz both from the low and high field sides of the torus (see Fig. 7.8a for $F_{prob} = 36$ GHz from the LFS and Fig. 7.8b for $F_{prob} = 39$ GHz from the HFS). The displacement of the cutoff layer causes the disappearance of modes from the spectra. The amplitudes are slightly stronger at the low field side, but this may also be linked to the difference in the channel sensitivities and therefore the ECMs do not have a strong ballooning character, which excludes KBM as well as TEM or ETG modes. The modes appear distinctly 80 ms after the transition from the L-mode (at $t = 3.32$ s), saturate until the first solitary ELM arrives at $t = 3.75$ s and disappear afterwards. After the

ELM the mode amplitude starts to grow again until the start of regular type-I ELMs in the H-mode ($t = 4.2$ s).

From the UFSR data the modes are observed in a narrow radial region $0.96 < \rho_{pol} < 0.995$ with the strongest branch around 95 kHz. The spectrogram in Fig. 7.9a is a result of averaging of 3 spectra within the time window $t = 3.557$–3.561 s calculated for 500 sweeps each. The average spectrum of the complex signal is asymmetric between positive and negative frequencies, which indicates that the shape of the oscillations is rather sawtooth-like or helicoidal (tilted) than sinusoidal.

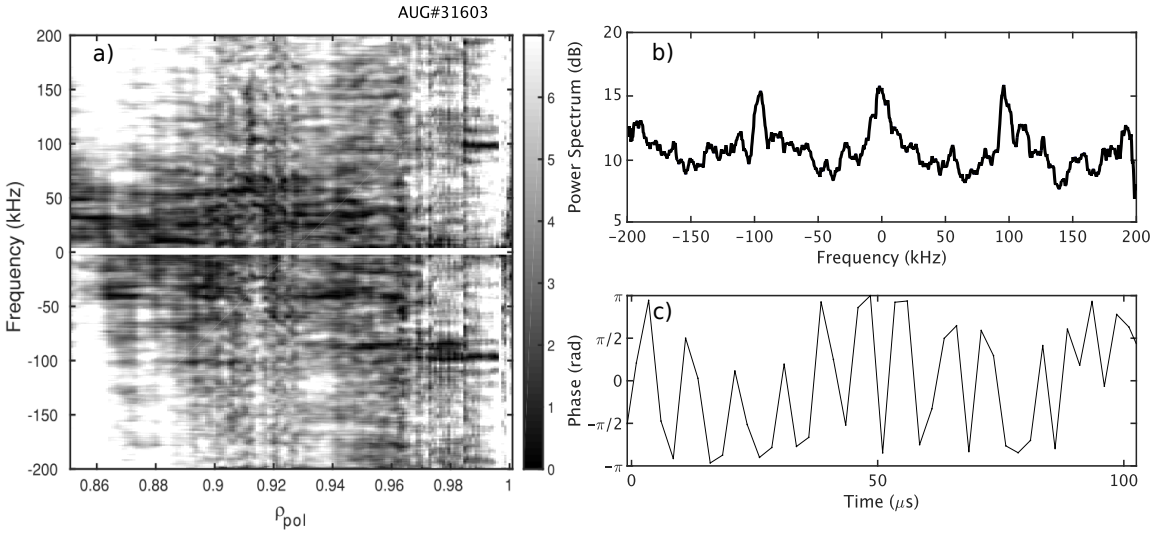

Figure 7.9: (a) Density fluctuation frequency power spectra during the ELM-free phase of the H-mode t =3.557–3.561 s, (b) a frequency power spectrum at $F_{prob} = 69.8$ GHz, $\rho_{pol} = 0.98$ and (c) the reflectometer signal phase showing a 95 kHz oscillation

Looking at the spectrum at one probing frequency $F_{prob} = 69.8$ GHz, the main branch at 95 kHz and of the width of about 5 kHz is visible with the side branches of 80 and 110 kHz (Fig. 7.9b). The reflectometer phase shows sequences of oscillations (Fig. 7.9c) with a period about 7–11 μs, with 5–20 periods each. In the frequency spectrum this bursty behaviour manifests as a broadening of the ECM peaks for longer FFT time windows. This behaviour is observed both in I-phase and H-mode discharges.

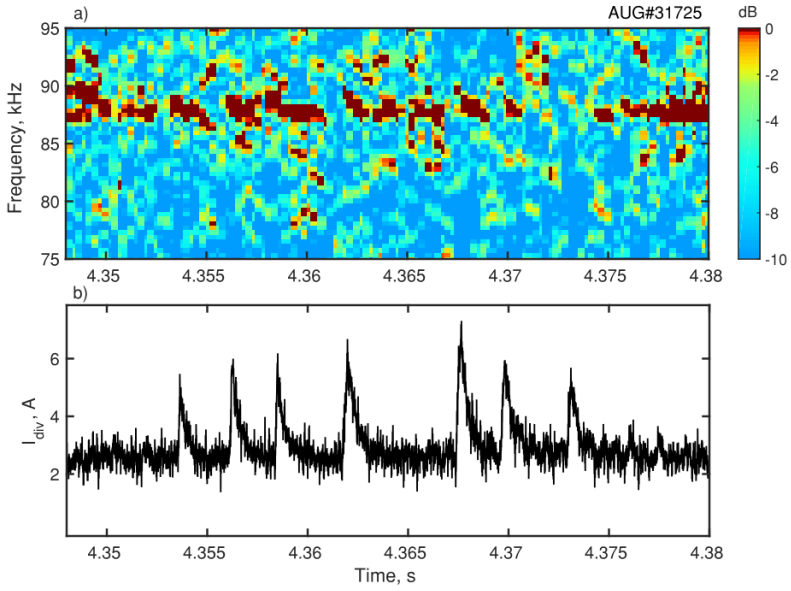

Figure 7.10: (a) Density fluctuation frequency power spectra in between ELMs at $\rho_{pol} = 0.97$ and (b) outer divertor current indicating type-I ELMs. Most of the time the ECM dissapears during ELM crashes but not always.

7.3 Edge coherent modes in between ELMs

In between ELM crashes the ECMs recover and the UFSR sweep rate allows to follow their time evolution. The time between two consecutive ELMs of 1–10 milliseconds allows to calculate a few FFT in different phases of the ELM cycle. Figure 7.10a depicts the ECM evolution during ELMs for the radial position $\rho_{pol} = 0.97$. The sliding FFT (SFFT) is calculated with windows of 500 reflectometer sweeps of 1.25 μs each with a 50 % overlap. For each FFT window the probing frequency closest to $\rho_{pol} = 0.97$ was selected and the resulting spectrum was normalised to its maximum. The ECM has a frequency of about 88 kHz and its amplitude varies from saturation to disappearance during the ELM relaxation of the pedestal, or after a sequence of frequent ELMs. A similar kind of modes is investigated in details in [144] as MHD activity with several branches with $n < 12$ and fixed f/n values. These mode were located in the pedestal region close to the separatrix from a comparison to the edge plasma rotation. However, the exact position of the modes was not found due to large uncertainties in the estimate of the plasma rotation velocity and equilibrium close to the separatrix [144]. Using the

ELM synchronization in the same work, it was shown that dominant toroidal mode numbers change from high to low n prior to the ELM crash in agreement with the results from non-linear MHD code JOREK [144]. Nevertheless, from the UFSR observations the modes with $n = 3$–7 and frequencies of up to 150 kHz seem not to trigger ELMs: sometimes they are not observed during the ELM crash (see Fig. 7.10 at t =4.362 s for example) and there are cases where they maintain their amplitude (Fig. 7.10 at t =4.358 s). However, the modes might play a role in the clamping of the pedestal gradients. The frequency of the ECMs does not change by more than 5 kHz in between ELMs, a drop of the frequency can be noticed prior to some ELMs.

7.4 Edge coherent modes during I-phase

During the I-phase the ECMs are less pronounced than in between ELMs, but can still be visible in the UFSR spectrogram if the FFT time windows are short enough. No chirping of the ECM frequency can be detected within a few kHz error bars. Figure 7.11 shows the spectrogram averaged over 4 consecutive time windows of 625 μs each.

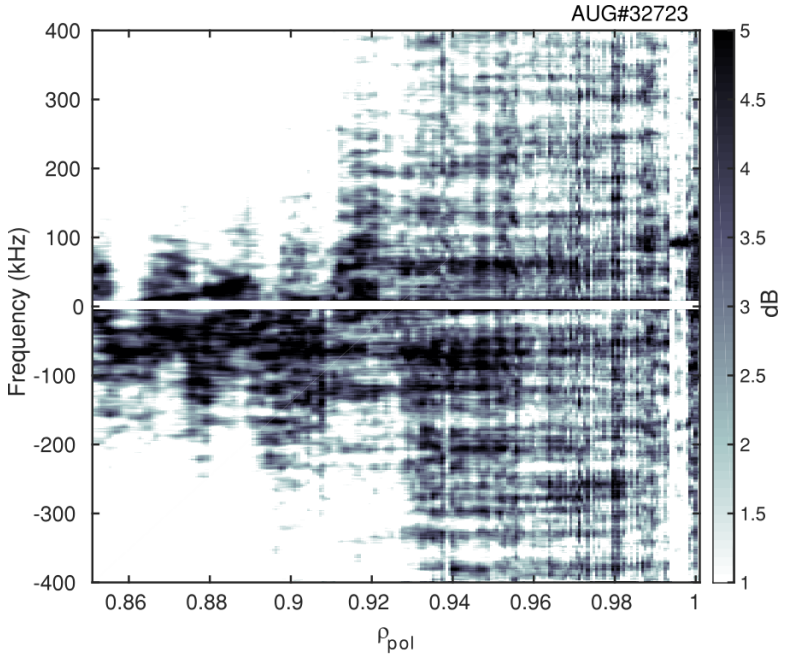

Figure 7.11: Density fluctuation frequency power spectra during the I-phase at t = 3.3230–3.3255 s in the plasma edge with the ECM around 60 kHz

The strongest ECM has a poorly distinguishable frequency around 60 kHz, which was confirmed by magnetic pick-up coil data. Figure 7.12a illustrates the growth of the ECMs after the L-I confinement transition indicated by the drop of the inner divertor current (Fig. 7.12b) at $t = 2.351$ s for the discharge #32944. The spectrogram is constructed with a SFFT (time windows of 250 μs and 50 % overlap) applied to the UFSR signal around $\rho_{pol} = 0.97$. With the given time resolution a study of the evolution of the spectra during one period of the I-phase does not seem possible.

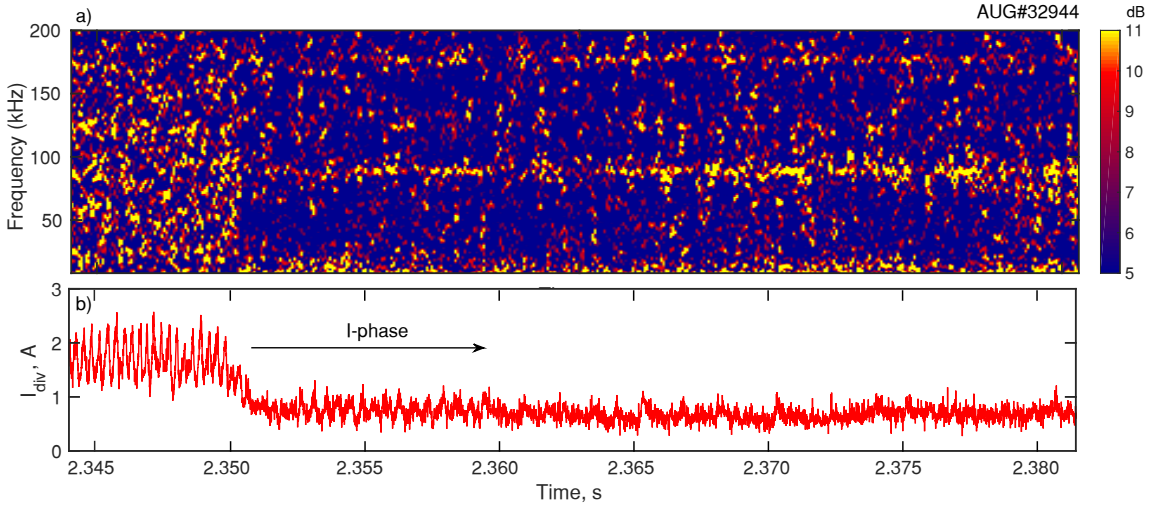

Figure 7.12: (a) Density fluctuation frequency power spectra during I-phase around the same radial position $\rho_{pol} = 0.97$ and (b) outer divertor current

However, by constructing the radial correlation length for the UFSR signal amplitude taking $\rho_{pol} = 0.98$ as the reference position it has been observed that during the I-phase in between the bursts the correlation length grows (Fig. 7.13). This could indicate the corresponding onset of the ECM in the pedestal region where the pressure gradient steepens. The correlation length was taken as the width of a Gaussian fit to the autocorrelation function calculated for time windows of 125 μs.

In Fig. 7.13 the first ELM is visible in the magnetic signal at $t = 3.245$ s as a large perturbation. The radial correlation length reaches 2 cm prior to the ELM crash. The behaviour is similar before each cycle of the I-phase, where the radial correlation length increases from 1.2 to 1.7 cm. Although the appearance of the modes might be connected with the L-H transition and their amplitude might play a role in the pedestal stability

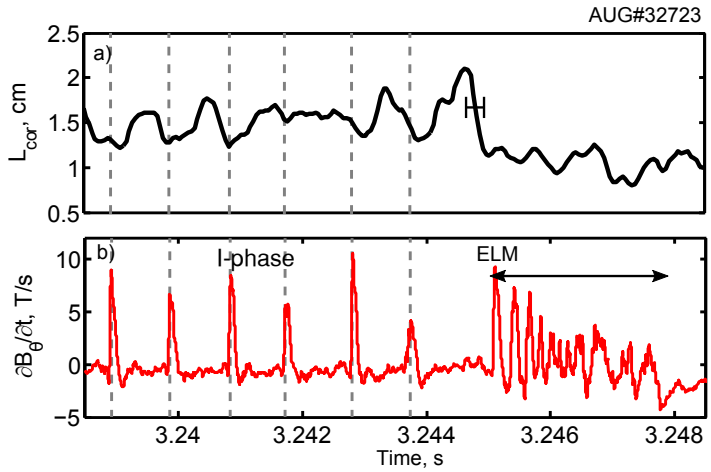

Figure 7.13: (a) Radial correlation length in the pedestal region during the I-phase bursts and an ELM crash at $t = 3.245$ s and (b) $\partial B_\theta/\partial t$

during the I-phase, it is unknown whether they contribute to the mechanisms of the transition. Note that the reduction of the radial correlation length could be related to the confinement improvement.

7.5 Summary

The edge coherent modes observed in ASDEX Upgrade in the range of 50–200 kHz in reflectometer and magnetic pick-up coil spectra have several well reproducible properties. The UFSR data allow to locate the modes in the plasma edge $0.87 < \rho_{pol} < 1.00$ and, from the comparison between the probing frequencies and density profiles, at the pedestal top. The radial range in which the modes are detected might be broader than the actual size of the mode due to the radial motion of the entire plasma profile. Through a detailed analysis it is shown that the ECM frequency increases with plasma edge electron pressure. ECMs have low toroidal numbers between $n = -2$ and -11 and propagate in the electron diamagnetic direction in the laboratory frame. From the analysis of the wavenumber spectra it follows that the ECMs have a small radial wavenumber $k_r < 2$ cm^{-1}. The fixed frequency reflectometer channels detect the ECM both on the LFS and the HFS excluding a strong ballooning character. The absence of the ballooning character, the propagation in the electron diamagnetic direction and the localisation at the pedestal top indicate that the ECMs might be microtearing modes.

The modes often have an intermittent character with sequences of 5–20 oscillations observed first in the reflectometry phase signal and only when the ECMs are saturated, in the magnetic pick-up coil signal. The observation of ECMs in ECRH only discharges indicates that their existence does not depend on energetic particles. This fact, together with the linear frequency dependence on the electron density, could exclude the hypothesis of a TAE nature of the ECM. Although the ECMs exist in between ELMs and I-phase bursts and disappear from the spectra during a burst, there are few cases where the modes either disappear without a burst or persist in spite of a pedestal relaxation. This suggests that the ECM is not an ELM precursor, although it might play a role in the clamping of the pedestal pressure gradient. The impact of ECMs on plasma confinement is still an issue that needs to be investigated in the future.

8 Conclusions

> There is no such thing as individual knowledge, a particular knowledge belonging to one special person or group. Knowledge is the sea of humanity, the field of humanity, the general condition of human existence.
> –Yukio Mishima, The Temple of the Golden Pavilion

Plasma turbulence and the associated transport belong to one of the most important factors which limit the plasma confinement in a tokamak. In the H-mode (high confinement mode) the energy confinement time is about a factor of two higher compared to that in L-mode (low-confinement mode). The improved confinement is reached after an intermediate phase (I-phase), when an edge transport barrier develops due to turbulence reduction. In the H-mode the turbulence is suppressed due to sheared $\mathbf{E} \times \mathbf{B}$ flows as the radial electric field forms a deep well. The edge turbulence level during the I-phase undergoes periodic limit-cycle oscillations (LCO). It is known that the turbulence is reduced by sheared plasma flows driven by a radial electric field. The I-phase oscillations have been described as a predator-prey-like interplay between turbulence and the zonal flow or as a periodic relaxation of the background radial electric field due to MHD instability. Hence, two alternative models exist for the generation of the sheared flow: the background neoclassical E_r or a turbulence driven zonal flow. The goal of this thesis was to examine the L-H transition from the beginning of the I-phase to the established H-mode. To this end, the temporal evolution of the density profile, its gradient and the density fluctuation level were studied using an ultra-fast swept reflectometer (UFSR) and fixed frequency Doppler reflectometer systems.

Diagnostic tools have been developed to get a better understanding of the turbulence properties. The density fluctuations, being an order of magnitude larger than other types of fluctuations, are among the most important parameters to measure. The V- and W-band ultra-fast swept reflectometer used in this work was transferred from the Tore Supra tokamak to ASDEX Upgrade in 2013–2014. During this thesis work it

was adapted, the acquisition system was upgraded and the modulation frequency was increased to enable fully resolved radial measurements within 1 μs. The sweep time of 1 μs over a frequency range from 50 to 105 GHz allowed to reconstruct density fluctuation wavenumber spectra from the phase variations measured in the reflected microwave beam. Hardware changes were made to improve the signal amplitude and a system of pneumatic switches was installed for the protection of the reflectometer from possible ECRH stray radiation. By February 2014 a system of remote control was installed allowing the measurements with two acquisition cards which register 20,000 and 200,000 sweeps per plasma discharge, respectively. These new diagnostics capabilities have been exploited during the 2014-2016 campaigns for many research topics which are not presented in this work. The precise density profile reconstruction, confirmed through the cross-comparison with other AUG diagnostics, was used for the study of boundary displacements due to ideal kink modes [108]. The frequency spectra reconstruction for different radial positions allowed to investigate the LOC-SOC confinement transition in Ohmic plasma[109] and turbulent trapped electron modes [152]. The work presented here was focused on the turbulence dynamics investigation during L-H transitions and edge localised modes (ELM).

First studies of the electron density profile dynamics, the density turbulence level, radial wavenumber and frequency spectra during L-H transitions in ASDEX Upgrade have been performed with a time resolution of 1 μs. The reconstruction of the turbulence level is achieved with a closed-loop procedure for the phase of the UFSR signal. The UFSR measurements show that the density large scale fluctuations ($1\ \mathrm{cm}^{-1} < k_r < 10\ \mathrm{cm}^{-1}$) decrease in the pedestal region after an L-H transition, which confirms the theoretical predictions of the turbulence reduction by sheared flows and supports previous experimental evidences.

The intermediate (I-) phase, which preceeds the transition to the H-mode, is characterised by limit-cycle oscillations of the fluctuations amplitude and the background flow. In the observed I-phases in medium and high density discharges, an important contribution of the density gradient to the neoclassical radial electric field E_r has been confirmed. During the I-phase, the density profile modification due to the bursts starts from the pedestal region leading to a simultaneous destruction of the pressure gradient within the region of the normalised radius $0.97 < \rho_{pol} < 1$, i.e. right at the plasma edge. The crash of the neoclassical electric field estimate is in phase with the burst in the turbulence level, pick-up coil bursts and Doppler measured E_r, which indicates the absence

of a predator-prey-like turbulence-flow interaction in the established I-phase. Hence, the I-phase bursts might be explained by growing pressure driven edge instabilities which cause a pressure crash consistent with previous studies on AUG [80]. Therefore the established I-phase in the medium to high densities presents more features of an ELM-like behaviour.

However, the comparison between the neoclassical electric field estimate and the Doppler reflectometer measurement of the poloidal flow velocity gives indications that the first few periods of the I-phase can have a different behaviour compared to the established I-phase. In the first cycle the neoclassical estimate deepens together with the drop of the turbulence level, while the Doppler measured E_r has a positive phase shift with respect to the turbulence level. First the turbulence starts to grow with the increasing pressure gradient, then the strong flow velocity appears and the turbulence level decreases. This could be a consequence of an interplay between zonal flow, the background flow and the turbulence, which might have an impact on the transition from L-mode to the I-phase. Note that the phase shift, if there is any, is shorter than 150–200 μs, therefore it can be measured only with the diagnostics of a higher temporal resolution.

The edge coherent modes (ECMs) observed in the I-phase and during ELM-free or ELMy H-mode phases have common characteristics, such as their frequency of about 100 kHz, edge radial position and scaling of the frequency with the pressure gradient. The observation of ECMs during L-H transitions led to a more detailed documentation of the edge modes in ASDEX Upgrade in the range of 50–200 kHz. The ECMs are visible in the reflectometer and magnetic pick-up coil spectra and have several well reproducible properties. First, the modes are localised with the UFSR in the plasma edge region $0.87 < \rho_{pol} < 1.00$ and, from the comparison between the probing frequencies and density profiles, at the pedestal top. Second, the magnetic pick-up coils show that the ECMs have toroidal numbers between $n = -2$ and -11 and propagate in the electron diamagnetic direction in the laboratory frame. The fixed frequency reflectometers channels detect the ECM both on the low-field side and the high-field side of the plasma, which excludes a strong ballooning character. Therefore it is unlikely that the ECMs are kinetic ballooning modes. The observation of ECM in discharges heated by microwaves (ECRH) only indicates that their existence does not depend on energetic particles. This fact, together with the linear frequency dependence on the electron density, excludes the hypothesis of a toroidal Alfvén eigenmode. The absence

of the ballooning character, the propagation in the electron diamagnetic direction and the localisation at the pedestal top might indicate microtearing modes as source of the observed coherent fluctuations. Although the ECM exist in between ELMs and I-phase bursts and disappear from the spectra during a burst in the divertor current, there are few cases where the modes either disappear without a burst or persist in spite of the pedestal relaxation. This suggests that the ECMs are not an ELM precursor, although they might play a role in the clamping of the pedestal gradients. The presence of ECM increases the radial correlation length. The impact of ECMs on plasma confinement is an issue that needs to be investigated in the future.

The potential of the UFSR as turbulence diagnostic exceeds the results presented in this work. Its fast temporal resolution allows to measure density dynamics and density fluctuation characteritics, such as frequency and wavenumber spectra, correlation lengths and time during fast transitions in a plasma discharge. By improving the analysis of the reflectometer signal phase fluctuation, the radial localisation of the turbulence properties can be reduced down to the millimetre scale. For the determination of the density fluctuations from the reflected signal, a closed-loop method with 1D full wave code has been used. However, it was shown that 2D effects should be introduced in the transfer function which links the phase fluctuation and the density fluctuation. As the radial size of the edge transport barrier is less than 1 cm, it is also fundamental to improve the diagnostic radial resolution.

Bibliography

[1] H.-S. Bosch et al. “Improved formulas for fusion cross-sections and thermal reactivities.” *Nucl. Fusion* 32.4 (1992), p. 611.

[2] L. Spitzer. *A proposed stellarator*. Tech. rep. Princeton Univ., NJ Forrestal Research Center, 1951.

[3] E. I. Moses. “Ignition on the National Ignition Facility: a path towards inertial fusion energy.” *Nucl. Fusion* 49.10 (2009), p. 104022.

[4] J. D. Lawson. “Some Criteria for a Power producing thermonuclear reactor.” *Atomic Energy Research Establishment* 1807 (1955).

[5] M. Kikuchi et al. *Fusion Physics*. International Atomic Energy Agency, 2012.

[6] L. Artsimovich. “Research on controlled thermonuclear reactions in the USSR.” *Physics-Uspekhi* 1.2 (1958), pp. 191–207.

[7] N. Bretz. “Diagnostic instrumentation for microturbulence in tokamaks.” *Rev. Sci. Instrum.* 68.8 (1997), pp. 2927–2964.

[8] F. Wagner et al. “Regime of Improved Confinement and High Beta in Neutral-Beam-Heated Divertor Discharges of the ASDEX Tokamak.” *Phys. Rev. Lett.* 49 (1982), pp. 1408–1412.

[9] Y. R. Martin et al. “Power requirement for accessing the H-mode in ITER.” *Journal of Physics: Conference Series* 123 (2008), p. 012033.

[10] H. Zohm. “Dynamic behavior of the L-H transition.” *Phys. Rev. Lett.* 72 (1994), pp. 222–225.

[11] G. D. Conway et al. “Mean and Oscillating Plasma Flows and Turbulence Interactions across the L-H Confinement Transition.” *Phys. Rev. Lett.* 106.6 (2011), p. 065001.

[12] K. H. Burrell et al. "Quiescent H-mode plasmas in the DIII-D tokamak." *Plas. Phys. and Cont. Fusion* 44.5A (2002), A253.

[13] H. Biglari et al. "Influence of sheared poloidal rotation on edge turbulence." *Physics of Fluids B: Plasma Physics* 2.1 (1990), p. 1.

[14] F. L. Hinton et al. "Theory of plasma transport in toroidal confinement systems." *Rev. Mod. Phys.* 48 (1976), pp. 239–308.

[15] K. Miki et al. "Spatio-temporal evolution of the L–I–H transition." *Phys. Plasmas* 19.9 (2012), pp. –.

[16] P. H. Diamond et al. "Self-Regulating Shear Flow Turbulence: A Paradigm for the *L* to *H* Transition." *Phys. Rev. Lett.* 72 (1994), pp. 2565–2568.

[17] H. Zohm et al. "Investigation of the bifurcation character of the H-mode in ASDEX Upgrade." *Plas. Phys. and Cont. Fusion* 37.4 (1995), pp. 437–446.

[18] R. Colchin et al. "Slow L-H Transitions in DIII-D Plasmas." *Phys. Rev. Lett.* 88.25 (2002), p. 255002.

[19] S. J. Zweben et al. "Quiet periods in edge turbulence preceding the L-H transition in the National Spherical Torus Experiment." *Phys. Plasmas* 17.10 (2010).

[20] T. Estrada et al. "L-H Transition Experiments in TJ-II." *Contributions to Plasma Physics* 50.6-7 (2010), pp. 501–506.

[21] S. Braginsky et al. "Voprosy teorii plazmy." *Problems of plasma theory* 1 (1963).

[22] J. Dolbeault. "An introduction to kinetic equations: the Vlasov-Poisson system and the Boltzmann equation." *Discrete and Continuous Dynamical Systems* 8.2 (2002), pp. 361–380.

[23] P. Helander et al. *Collisional Transport in Magnetized Plasmas*. Cambridge Monographs on Plasma Physics. Cambridge University Press, 2005.

[24] M. Cavedon. "The role of the radial electric field in the development of the edge transport barrier in the ASDEX Upgrade tokamak." Ph.D. thesis. Universität München, 2016.

[25] P. Manz. *Lectures on turbulent transport in fusion*. Technische Universität München, 2015.

[26] J. Wesson. *Tokamaks*. International Series of Monographs on Physics. OUP Oxford, 2011.

[27] F. Wagner et al. "Transport in toroidal devices-the experimentalist's view." *Plas. Phys. and Cont. Fusion* 35.10 (1993), p. 1321.

[28] V. Ginzburg. *Rasprostranenie electromagnitnyh voln v plasme*. Nauka, 1967, pp. 264–280.

[29] E. Mazzucato. "Relativistic effects on microwave reflectometry." *Physics of Fluids B: Plasma Physics* 4.10 (1992), pp. 3460–3461.

[30] X. L. Zou et al. "Scattering of an electromagnetic wave in a plasma close to a cut-off layer. Application to fluctuation measurements." *Plas. Phys. and Cont. Fusion* 33.8 (1991), p. 903.

[31] B. B. Afeyan et al. "The scattering phase shift due to Bragg resonance in one-dimensional fluctuation reflectometry." *Plas. Phys. and Cont. Fusion* 37.3 (1995), p. 315.

[32] C. Fanack et al. "Ordinary-mode reflectometry: modification of the scattering and cut-off responses due to the shape of localized density fluctuations." *Plas. Phys. and Cont. Fusion* 38.11 (1996), p. 1915.

[33] S. Baang et al. "Spatial resolution of microwave/millimeter-wave reflectometry." *Rev. Sci. Instrum.* 61.10 (1990), pp. 3013–3015.

[34] T. L. Rhodes et al. "Fundamental investigation of reflectometry as a density fluctuation diagnostic." *Rev. Sci. Instrum.* 63.10 (1992), pp. 4599–4604.

[35] V. Igochine et al. "Stochastic sawtooth reconnection in ASDEX Upgrade." *Nucl. Fusion* 47.1 (2006), p. 23.

[36] J. Freidberg et al. "Kink instabilities in a high-β tokamak." *The Physics of Fluids* 16.11 (1973), pp. 1909–1916.

[37] H. Zohm. "Edge localized modes (ELMs)." *Plas. Phys. and Cont. Fusion* 38.2 (1996), p. 105.

[38] F. Troyon et al. "A semi-empirical scaling law for the β-limit in tokamaks." *Physics Letters A* 110.1 (1985), pp. 29–34.

[39] E. Hameiri et al. "Stability of ballooning modes in a rotating plasma." *Physical Review A* 41.2 (1990), p. 1186.

[40] E. Doyle et al. “Modifications in turbulence and edge electric fields at the L–H transition in the DIII-D tokamak.” *Physics of Fluids B: Plasma Physics* 3.8 (1991), pp. 2300–2307.

[41] C. P. von Thun et al. “Identifying the MHD signature and power deposition characteristics associated with type-II ELMs in ASDEX Upgrade.” *Plas. Phys. and Cont. Fusion* 50.6 (2008), p. 065018.

[42] R. Maingi et al. “H-mode pedestal, ELM and power threshold studies in NSTX.” *Nucl. Fusion* 45.9 (2005), p. 1066.

[43] M. Dunne. “Inter-ELM evolution of the edge current density profile on the ASDEX Upgrade tokamak.” Ph.D. thesis. National University of Ireland, Cork, 2013.

[44] W. Suttrop. “The physics of large and small edge localized modes.” *Plas. Phys. and Cont. Fusion* 42.5A (2000), A1.

[45] P. B. Snyder et al. “Development and validation of a predictive model for the pedestal height a.” *Phys. Plasmas* 16.5 (2009), p. 056118.

[46] D. Dickinson et al. “Kinetic instabilities that limit β in the edge of a tokamak plasma: a picture of an H-mode pedestal.” *Phys. Rev. Lett.* 108.13 (2012), p. 135002.

[47] R. J. Goldston et al. *Introduction to plasma physics*. CRC Press, 1995.

[48] U. Stroth. *Plasmaphysik*. Vieweg+Teubner Verlag, 2011.

[49] W. Horton et al. “Quasi-two-dimensional dynamics of plasmas and fluids.” *Chaos: An Interdisciplinary Journal of Nonlinear Science* 4.2 (1994), pp. 227–251.

[50] B. Scott. “Three-dimensional computation of drift Alfvén turbulence.” *Plas. Phys. and Cont. Fusion* 39.10 (1997), p. 1635.

[51] B. Fischer et al. “Experimental study of drift wave turbulence and anomalous transport.” *Plas. Phys. and Cont. Fusion* 31.3 (1989), p. 453.

[52] A. Kolmogorov. *Sci.Acad. USSR* 31.6 (1941), pp. 538–541.

[53] H. Grant et al. “Turbulence spectra from a tidal channel.” *Journal of Fluid Mechanics* 12.02 (1962), pp. 241–268.

[54] R. H. Kraichnan. *Inertial ranges in two-dimensional turbulence*. Tech. rep. DTIC Document, 1967.

[55] A. B. Navarro et al. "Applications of large eddy simulation methods to gyrokinetic turbulence." *Phys. Plasmas* 21.3 (2014), p. 032304.

[56] L. Prandtl. "Bericht uber Untersuchungen zur ausgebildeten Turbulenz." *Zeitschrift fur angew. Math. u. Mechanik* 5.2 (1925), pp. 136–139.

[57] X. Garbet. "Turbulence in fusion plasmas: key issues and impact on transport modelling." *Plas. Phys. and Cont. Fusion* 43.12A (2001), A251.

[58] U. Stroth et al. "On the interaction of turbulence and flows in toroidal plasmas." *Plas. Phys. and Cont. Fusion* 53.2 (2011), p. 024006.

[59] P. H. Diamond et al. "Zonal flows in plasma – a review." *Plas. Phys. and Cont. Fusion* 47.5 (2005), R35.

[60] P. Manz et al. "Zonal flow triggers the LH transition in the Experimental Advanced Superconducting Tokamak." *Phys. Plasmas* 19.7 (2012), p. 072311.

[61] A. Fujisawa. "A review of zonal flow experiments." *Nucl. Fusion* 49.1 (2009), p. 013001.

[62] K. Itoh et al. "Physics of zonal flows." *Phys. Plasmas* 13.5 (2006).

[63] G. D. Conway et al. "Amplitude behaviour of geodesic acoustic modes in the ASDEX Upgrade tokamak." *Plas. Phys. and Cont. Fusion* 50.8 (2008), p. 085005.

[64] F. Levinton et al. "Radial electric field measurements in reversed shear plasmas." *Phys. Rev. Lett.* 80.22 (1998), p. 4887.

[65] Y. Hamada et al. "Density fluctuations in JIPP T-IIU tokamak plasmas measured by a heavy ion beam probe." *Nucl. Fusion* 37.7 (1997), p. 999.

[66] P. Manz et al. "Poloidal asymmetric flow and current relaxation of ballooned transport during I-phase in ASDEX Upgrade." *Phys. Plasmas* 23.5 (2016), p. 052302.

[67] F. Ryter et al. "H-mode threshold and confinement in helium and deuterium in ASDEX Upgrade." *Nucl. Fusion* 49.6 (2009), p. 062003.

[68] R. J. Groebner et al. "Critical edge parameters for H-mode transition in DIII-D." *Plas. Phys. and Cont. Fusion* 40.5 (1998), p. 673.

[69] J. Hugill. "Transport in tokamaks – a review of experiment." *Nucl. Fusion* 23.3 (1983), p. 331.

[70] S.-I. Itoh et al. "Model of L to H-Mode Transition in Tokamak." *Phys. Rev. Lett.* 60 (1988), pp. 2276–2279.

[71] G. D. Conway et al. "Plasma rotation profile measurements using Doppler reflectometry." *Plas. Phys. and Cont. Fusion* 46.6 (2004), p. 951.

[72] D. Prisiazhniuk et al. "Application of poloidal correlation reflectometry to study turbulence at ASDEX Upgrade." *Proc. 12th Int. Reflectometry Workshop.* 2015.

[73] P. J. McCarthy et al. *The CLISTE interpretive equilibrium code.* Max-Planck-Institut für Plasmaphysik, 1999.

[74] A. Mlynek et al. "Real-time feedback control of the plasma density profile on ASDEX Upgrade." *Nucl. Fusion* 51.4 (2011).

[75] S. K. Rathgeber et al. "Estimation of edge electron temperature profiles via forward modelling of the electron cyclotron radiation transport at ASDEX Upgrade." *Plas. Phys. and Cont. Fusion* 55.2 (2013), p. 025004.

[76] I. H. Hutchinson. *Principles of plasma diagnostics.* Vol. 1. IH. Cambridge University Press, 1990.

[77] H. Murmann et al. "The Thomson scattering systems of the ASDEX upgrade tokamak." *Rev. Sci. Instrum.* 63.10 (1992), pp. 4941–4943.

[78] B. Kurzan et al. "Edge and core Thomson scattering systems and their calibration on the ASDEX Upgrade tokamak." *Rev. Sci. Instrum.* 82.10 (2011).

[79] M. Willensdorfer et al. "Characterization of the Li-BES at ASDEX Upgrade." *Plas. Phys. and Cont. Fusion* 56.2 (2014), p. 025008.

[80] G. Birkenmeier et al. "Magnetic structure and frequency scaling of limit-cycle oscillations close to L-to H-mode transitions." *Nucl. Fusion* 56.8 (2016), p. 086009.

[81] V. Igochine et al. *Active control of magneto-hydrodynamic instabilities in hot plasmas.* Springer, 2015.

[82] G. Conway et al. "Observations on core turbulence transitions in ASDEX Upgrade using Doppler reflectometry." *Nucl. Fusion* 46.9 (2006), S799.

[83] E. Viezzer et al. "High-accuracy characterization of the edge radial electric field at ASDEX Upgrade." *Nucl. Fusion* 53.5 (2013), p. 053005.

[84] G. D. Conway et al. "Interaction of mean and oscillating plasma flows across confinement mode transitions." *Plasma and Fusion Research* 5 (2010), S2005.

[85] T. Happel et al. "The optimized steerable W-band Doppler reflectometer on ASDEX Upgrade: possibilities and issues." Proc. 11$^{\text{th}}$ International Reflectometry Workshop, 2013.

[86] E. Poli et al. "TORBEAM, a beam tracing code for electron-cyclotron waves in tokamak plasmas." *Computer Physics Communications* 136.1 (2001), pp. 90–104.

[87] L. Vermare et al. "Detection of geodesic acoustic mode oscillations, using multiple signal classification analysis of Doppler backscattering signal on Tore Supra." *Nucl. Fusion* 52.6 (2012), p. 063008.

[88] K. G. Budden. *The propagation of radio waves: the theory of radio waves of low power in the ionosphere and magnetosphere*. Cambridge University Press, 1988.

[89] E. Mazzucato. "Microwave reflectometry for magnetically confined plasmas." *Rev. Sci. Instrum.* 69.6 (1998), pp. 2201–2217.

[90] M. E. Manso. "Reflectometry in fusion devices." *Plas. Phys. and Cont. Fusion* 35.SB (1993), B141.

[91] C. Laviron et al. "Reflectometry techniques for density profile measurements on fusion plasmas." *Plas. Phys. and Cont. Fusion* 38.7 (1996), p. 905.

[92] J. L. Doane et al. "Plasma density measurements using FM–CW millimeter wave radar techniques." *Review of Scientific Instruments* 52.1 (1981), pp. 12–15.

[93] F. Simonet. "Measurement of electron density profile by microwave reflectometry on tokamaks." *Rev. Sci. Instrum.* 56.5 (1985), pp. 664–669.

[94] H. Bottollier-Curtet et al. "Microwave reflectometry with the extraordinary mode on tokamaks: Determination of the electron density profile of Petula-B." *Rev. Sci. Instrum.* 58.4 (1987), pp. 539–546.

[95] A. Silva et al. "Ultrafast broadband frequency modulation of a continuous wave reflectometry system to measure density profiles on ASDEX Upgrade." *Rev. Sci. Instrum.* 67.12 (1996), pp. 4138–4145.

[96] G. R. Hanson et al. "A swept two-frequency microwave reflectometer for edge density profile measurements on TFTR." *Rev. Sci. Instrum.* 63.10 (1992), pp. 4658–4660.

[97] A. E. Costley et al. "Recent developments in microwave reflectometry at JET." *Rev. Sci. Instrum.* 61.10 (1990), pp. 2823–2828.

[98] T. Fukuda et al. "Broadband reflectometry for the density profile and fluctuation measurements in the JT-60 tokamak." *Rev. Sci. Instrum.* 61.11 (1990), pp. 3524–3527.

[99] A. Skibenko et al. "Measurement of plasma density profile and fluctuations in the URAGAN-3M torsatron using bipolarization reflectometry." *Plasma Physics Reports* 20.1 (1994).

[100] S. Hacquin et al. "Use of dispersive effects for density profile reconstruction from pulse radar reflectometry measurements alone." *Plas. Phys. and Cont. Fusion* 42.3 (2000), p. 347.

[101] P. Moreau et al. "Ultrafast frequency sweep heterodyne reflectometer on the Tore Supra tokamak." *Rev. Sci. Instrum.* 71.1 (2000), pp. 74–81.

[102] V. Vershkov et al. "Plasma diagnostics experiments on the T-10 tokamak by means of a reflected microwave signal." *Soviet Physics-Technical Physics (English Translation)* 32.5 (1987), pp. 523–526.

[103] R. Sabot et al. "Single sideband modulator, a key component of Tore-Supra heterodyne reflectometers." *Rev. Sci. Instrum.* 75.8 (2004), pp. 2656–2659.

[104] L. Vermare. "Mesures de l'activite magnetohydrodynamique et de la micro-turbulence par reflectometrie a balayage." Ph.D. thesis. l'Universite de Provence, 2005.

[105] T. Gerbaud. "Etude de la microturbulence par réflectométrie dans un plasma de fusion sur le tokamak Tore-Supra." Ph.D. thesis. Université Henri Poincaré, 2008.

[106] F. Clairet et al. "Fast sweeping reflectometry upgrade on Tore Supra." *Rev. Sci. Instrum.* 81.10 (2010), p. 10D903.

[107] F Clairet et al. "Plasma turbulence measured with fast frequency swept reflectometry in JET H-mode plasmas." *Nucl. Fusion* 56.12 (2016), p. 126019.

[108] M. Willensdorfer et al. "Three dimensional boundary displacement due to stable ideal kink modes excited by external $n = 2$ magnetic perturbations." *arXiv preprint arXiv:1702.03177* (2017).

[109] H. Arnichand et al. "Identification of trapped electron modes in frequency fluctuation spectra." *Plas. Phys. and Cont. Fusion* 58.1 (2015), p. 014037.

[110] A. Lebschy et al. "Measurement of the E× B velocity across the LOC-SOC transition." *43rd EPS Conference on Plasma Physics*. European Physical Society. 2016.

[111] A. E. Costley. *Basic and Advanced Diagnostic Techniques for Fusion Plasmas*. CEC, Brussels, 1986.

[112] R. B. Morales et al. "New density profile reconstruction methods in X-mode reflectometry." *Rev. Sci. Instrum.* 88.4 (2017), p. 043503.

[113] S Heuraux et al. "Radial wave number spectrum of density fluctuations deduced from reflectometry phase signals." *Rev. Sci. Instrum.* 74.3 (2003), pp. 1501–1505.

[114] T. Gerbaud et al. *Density fluctuation measurements with fast-sweep X-mode reflectometry*.

[115] G. Dif-Pradalier et al. "Finding the elusive E× B staircase in magnetized plasmas." *Phys. Rev. Lett.* 114.8 (2015), p. 085004.

[116] E. Z. Gusakov et al. "2D modeling of turbulence wave number spectra reconstruction from radial correlation reflectometry data." *Plas. Phys. and Cont. Fusion* 57.7 (2015), p. 075009.

[117] D. J. Campbell. "Physics and goals of RTO/RC-ITER." *Plas. Phys. and Cont. Fusion* 41.12B (1999), B381.

[118] T. Happel et al. "Comparison of detailed experimental wavenumber spectra with gyrokinetic simulation aided by two-dimensional full-wave simulations." *Plas. Phys. and Cont. Fusion* 59.5 (2017), p. 054009.

[119] E. Z. Gusakov et al. "Two-dimensional non-linear theory of radial correlation reflectometry." *Plas. Phys. and Cont. Fusion* 46.9 (2004), p. 1393.

[120] J. R. Pinzón et al. "Enhanced Doppler reflectometry power response: physical optics and 2D full wave modelling." *Plas. Phys. and Cont. Fusion* 59.3 (2017), p. 035005.

[121] G. S. Xu et al. "First Evidence of the Role of Zonal Flows for the *L-H* Transition at Marginal Input Power in the EAST Tokamak." *Phys. Rev. Lett.* 107 (2011), p. 125001.

[122] L. Schmitz et al. "Role of Zonal Flow Predator-Prey Oscillations in Triggering the Transition to H-Mode Confinement." *Phys. Rev. Lett.* 108.15 (Apr. 2012), p. 155002.

[123] T. Kobayashi et al. "Spatiotemporal Structures of Edge Limit-Cycle Oscillation before L-to-H Transition in the JFT-2M Tokamak." *Phys. Rev. Lett.* 111.3 (July 2013), p. 035002.

[124] J. Cheng et al. "Dynamics of Low-Intermediate-High-Confinement Transitions in Toroidal Plasmas." *Phys. Rev. Lett.* 110.26 (June 2013), p. 265002.

[125] K. C. Shaing et al. "Bifurcation theory of poloidal rotation in tokamaks: A model for *L* - *H* transition." *Phys. Rev. Lett.* 63 (1989), pp. 2369–2372.

[126] S.-I. Itoh et al. "Edge localized mode activity as a limit cycle in Tokamak plasmas." *Physical review letters* 67.18 (1991), p. 2485.

[127] E.-J. Kim et al. "Zonal Flows and Transient Dynamics of the *L-H* Transition." *Phys. Rev. Lett.* 90 (2003), p. 185006.

[128] M. Cavedon et al. "Interplay between turbulence, neoclassical and zonal flows during the transition from low to high confinement mode at ASDEX Upgrade." *Nucl. Fusion* 57.1 (2017), p. 014002.

[129] G. Birkenmeier et al. "Characterisation and frequency scaling of limit-cycle oscillations close to L- to H-transitions." *Plas. Phys. and Cont. Fusion* (2015).

[130] E. Viezzer et al. "Evidence for the neoclassical nature of the radial electric field in the edge transport barrier of ASDEX Upgrade." *Nucl. Fusion* 54.1 (2014), p. 012003.

[131] J. A. Morales et al. "Edge localized mode rotation and the nonlinear dynamics of filaments." *Phys. Plasmas* 23.4 (2016), p. 042513.

[132] G. Yun et al. "Two-dimensional visualization of growth and burst of the edge-localized filaments in KSTAR H-mode plasmas." *Phys. Rev. Lett.* 107.4 (2011), p. 045004.

[133] W. Suttrop et al. "ELM-free stationary H-mode plasmas in the ASDEX Upgrade tokamak." *Plas. Phys. and Cont. Fusion* 45.8 (2003), p. 1399.

[134] A. Diallo et al. "Correlations between quasi-coherent fluctuations and the pedestal evolution during the inter-edge localized modes phase on DIII-D a." *Phys. Plasmas* 22.5 (2015), p. 056111.

[135] A. Diallo et al. "Observation of edge instability limiting the pedestal growth in tokamak plasmas." *Phys. Rev. Lett.* 112.11 (2014), p. 115001.

[136] P. B. Snyder et al. "Stability and dynamics of the edge pedestal in the low collisionality regime: physics mechanisms for steady-state ELM-free operation." *Nucl. Fusion* 47.8 (2007), p. 961.

[137] F. M. Laggner et al. "High frequency magnetic fluctuations correlated with the inter-ELM pedestal evolution in ASDEX Upgrade." *Plas. Phys. and Cont. Fusion* 58.6 (2016), p. 065005.

[138] C. P. Perez et al. "Washboard modes as ELM-related events in JET." *Plas. Phys. and Cont. Fusion* 46.1 (2003), p. 61.

[139] J. A. Snipes et al. "The quasi-coherent signature of enhanced Dα H-mode in Alcator C-Mod." *Plas. Phys. and Cont. Fusion* 43.4 (2001), p. L23.

[140] H. Wang et al. "New edge coherent mode providing continuous transport in long-pulse h-mode plasmas." *Phys. Rev. Lett.* 112.18 (2014), p. 185004.

[141] C. Z. Cheng et al. "Fast particle destabilization of toroidal Alfven eigenmodes." *Nucl. Fusion* 35.12 (1995), p. 1639.

[142] Z. Chang et al. "Alfven frequency modes at the edge of TFTR plasmas." *Nucl. Fusion* 35.12 (1995), p. 1469.

[143] M. García-Muñoz et al. "Convective and diffusive energetic particle losses induced by Shear Alfvén waves in the ASDEX Upgrade tokamak." *Phys. Rev. Lett.* 104.18 (2010), p. 185002.

[144] F. Mink et al. "Toroidal mode number determination of ELM associated phenomena on ASDEX Upgrade." *Plas. Phys. and Cont. Fusion* 58.12 (2016), p. 125013.

[145] F Mink et al. "Characterization of inter-ELM magnetic oscillations on ASDEX Upgrade." *43rd EPS Conference on Plasma Physics*. European Physical Society. 2016.

[146] E. Viezzer et al. "High-resolution charge exchange measurements at ASDEX Upgrade." *Rev. Sci. Instrum.* 83.10 (2012).

[147] P. Manz et al. "Velocimetry analysis of type-I edge localized mode precursors in ASDEX Upgrade." *Plas. Phys. and Cont. Fusion* 56.3 (2014), p. 035010.

[148] D. Hatch et al. "A gyrokinetic perspective on the JET-ILW pedestal." *Nucl. Fusion* 57.3 (2017), p. 036020.

[149] A Biancalani et al. "Linear gyrokinetic particle-in-cell simulations of Alfvén instabilities in tokamaks." *Physics of Plasmas* 23.1 (2016), p. 012108.

[150] M Maraschek et al. "Observation of toroidicity-induced Alfvén eigenmodes in ohmically heated plasmas by drift wave excitation." *Physical review letters* 79.21 (1997), p. 4186.

[151] A. Biancalani et al. "2D continuous spectrum of shear Alfvén waves in the presence of a magnetic island." *Plas. Phys. and Cont. Fusion* 53.2 (2011), p. 025009.

[152] A. Lebschy et al. "Indirect measurement of the poloidal rotation velocity in the core of ASDEX Upgrade plasmas with charge exchange recombination spectroscopy." *42nd EPS Conference on Plasma Physics*. European Physical Society. 2015.

Acknowledgments

These four years have been a period of intense learning for me and I would like to thank people who have supported me during this time. I would first like to express my deep gratitude to my academic supervisors Prof. Ulrich Stroth and Prof. Stéphane Heuraux who enabled this joint Ph. D. work between TUM, University of Lorraine, IPP and CEA. Their interest to my research and excellent expertise on the topic of this thesis were for me a source of motivation.

I would also like to thank my advisor Dr. Frédéric Clairet who has guided me throughout the whole thesis and provided me with the tools that I needed to successfully complete my dissertation. He introduced me to the wonders and frustrations of the reflectometry world and I am grateful for his patient guidance and encouragement. I would like to express my great appreciation to Christine Bottereau who always impresses me with her deep knowledge of microwave technology. These two specialists developed the ultra-fast swept reflectometer in CEA and ensured its successful transfer to IPP. My sincere thanks are also extended to Dr. Garrard D. Conway for his help from the very first day of my Ph. D. work. Without his invaluable advice, insightful questions and support this work would not have been possible.

I wish to acknowledge the help provided by the turbulence group of IPP through regular discussions of the experimental findings at ASDEX Upgrade. I am particularly grateful for the Doppler refletometry data provided by Dr. Pascale Hennequin and Dr. Tim Happel and for the FM-CW reflectometer data from the IST team. Besides, I would like to thank Dr. Peter Manz and Dr. Gregor Birkenmeier for fruitful discussions. I wish to offer my special thanks to Dr. Dmitrii Prisiazhniuk and Valentina Nikolaeva for sharing the whole Ph. D. experience and many aspects of work with reflectometers.

The installation of the ultra-fast swept reflectometer at ASDEX Upgrade would have never be possible without the software design made by Diego Molina and the help of Dr. Karl Behler, Roland Merkel, Sven Martinov and Helmut Blank. I would also like to

thank Johannes Friesen, Daniel Grossman, Christian Aubanel and Dr. Antonio Silva for the help with the hardware design and installation.

I would like to extent my appreciation to Dr. Alessandro Biancalani, Dr. Rainer Fischer, Dr. Valentin Igochine, Dr. Dmytro Meshcheriakov, Dr. François Ryter, Dr. Matthias Willensdorfer, Dr. Elisabeth Wolfrum, Felician Mink for their input to this work. Special thanks should be given to Prof. Sanae-I. Itoh and Prof. Kimitaka Itoh for giving me the possibility to visit Kyushu University and the National Institute for Fusion Science. Their encouragement and our enlightening discussions have been a great source of inspiration for me.

I wish to thank the whole IPP staff, the ASDEX Upgrade team and in particular the my office mates: Dr. Marco Cavedon, Dr. Mike Dunne, Dr. Sina Fietz, Georg Harrer, Dr. Florian Laggner, Alexander Lebschy, Ou Pan, Ivan Paradela Perez, Ulrike Plank and Dr. Dmitrii Prisiazhniuk.

I am most thankful to my family and friends for the support during the thesis time. A warm thank to Alan Averill, Anneke van Giersbergen and Agnete M. Kirkevaag for being a source of motivation. Words cannot express how grateful I am to my parents, in particular for transmitting me the passion for physics and mathematics. At the end I would like to express my great appreciation to Ivan Glasser, who provided unconditional support and unending encouragement together with useful theoretical comments.